

Quantum Billiards on Polyhedral Surfaces

Kimberly Shen

Senior Thesis
Department of Physics
Princeton University

April 29, 2024



Advisor: Professor Biao Lian
Second Reader: Professor Shinsei Ryu

This paper represents my work in accordance with University regulations.

/s/ Kimberly Shen

Abstract

Solutions to Schrödinger’s equation for free particles confined to the surface of a regular polyhedron can be determined by solving the same equation on an unfolding of the polyhedral surface embedded in \mathbb{R}^2 and enforcing appropriate boundary conditions to ensure that the wavefunction is well-defined and smooth. Previous work by Bělín et al has determined the complete set of eigenmodes for particles on a tetrahedron, all of which are solvable. We extend their work to particles confined to the surfaces of the triangle- and square-faced regular polyhedra as well as square and rectangular prisms. In all cases aside from the tetrahedron, we find that the solvable eigenmodes are incomplete, and conjecture that the remaining eigenmodes are unsolvable and quantum chaotic. To support this conjecture, we examine the energy level spacing statistics of numerically-computed energy eigenmodes for a tight-binding model lattice on the polyhedral surface. Lastly, we consider the classical limit of the system—billiards on polyhedral surfaces—and show that the classical system is integrable for the tetrahedron but pseudo-integrable for all other polyhedra under consideration, consistent with the quantum result.

Acknowledgements

First and foremost, I would like to thank Professor Biao Lian for advising me on this thesis over the past academic year and for leading me into the fascinating world of mathematical and condensed matter physics. I am especially grateful for his generosity, clear guidance, and his continual patience with me, even when I was being chaotic and messing up in every way possible. I am also grateful to Professor Shinsei Ryu who kindly agreed to be my second reader. Last but not least, I would like to thank my team of support—my family, friends, and my piano professor, Dr. Francine Kay—for their unconditional love and concern for me.

Contents

1	Introduction	1
1.1	Wavefunctions	1
1.2	Polyhedral surfaces	2
1.3	Setup and boundary conditions	3
2	Solvable wavefunctions	6
2.1	General properties	6
2.2	Tetrahedron	10
2.3	Cube	12
2.4	Octahedron	14
2.5	Icosahedron	16
2.6	Square prism	18
2.6.1	Rational square prism	18
2.6.2	Irrational square prism	19
2.7	Rectangular prism	20
2.7.1	Rational rectangular prism	20
2.7.2	Irrational rectangular prism	21
3	Unsolvable wavefunctions on the cube	22
3.1	Incompleteness of solvable eigenmodes	22
3.1.1	Proof of incompleteness by direct computation	22
3.1.2	Proof of incompleteness via thermodynamics	25
3.1.3	Proof of incompleteness by symmetry	26
3.2	Cube Symmetries	26
3.3	Computational approach	27
3.3.1	Tight-binding Hamiltonian	28
3.3.2	Discretization of the wavefunction	29
3.3.3	Symmetry matrices	30
3.3.4	Diagonalizing the Hamiltonian	31
3.4	Representations of the cube symmetry group	32
3.4.1	Irreps of the solvable cube wavefunctions	33
3.4.2	Counting solvable wavefunctions	34
3.5	Energy level statistics	35
3.5.1	Level spacing ratios	35
3.5.2	Spectral form factor	37
3.6	Quantum scar states	39
4	Unsolvable wavefunctions on rectangle-faced polyhedra	42
4.1	Incompleteness of the solvable wavefunctions	42
4.1.1	Proof via symmetry	42
4.1.2	Proof via direct computation	42
4.1.3	Proof via thermodynamics	42
4.2	Van Hove Singularity	43
4.3	Square prism	44
4.3.1	Square prism symmetries	44
4.3.2	Representations of the symmetry group	44

4.3.3	Counting solvable wavefunctions	47
4.3.4	Energy level statistics	47
4.3.5	Quantum scar states	53
4.4	Rectangular prism	54
4.4.1	Rectangular prism symmetries	54
4.4.2	Representations of the symmetry group	54
4.4.3	Counting solvable wavefunctions	55
4.4.4	Energy level statistics	55
5	Solvable wavefunctions on the tetrahedron	60
5.1	Honeycomb lattice	60
5.1.1	Tight-binding Hamiltonian	60
5.2	Symmetries	62
5.2.1	Van Hove singularity	62
5.3	Completeness of solvable wavefunctions	63
5.3.1	Proof of completeness via thermodynamics	64
5.3.2	Failure of symmetry arguments to prove incompleteness	64
5.4	Irreps of the solvable wavefunctions	66
5.5	Energy level statistics	68
6	Unsolvable wavefunctions on the octahedron	70
6.1	Incompleteness of the solvable wavefunctions	70
6.1.1	Proof via thermodynamics	70
6.1.2	Proof of incompleteness via symmetry	70
6.2	Symmetries of the octahedron	70
6.2.1	Irreps of the solvable wavefunctions	71
6.2.2	Van Hove singularity	73
6.3	Energy level statistics	74
6.4	Quantum scarring	74
7	Unsolvable wavefunctions on the icosahedron	77
7.1	Incompleteness of the solvable wavefunctions	77
7.1.1	Proof via thermodynamics	77
7.1.2	Proof of incompleteness via symmetry	77
7.2	Symmetries of the icosahedron	77
7.2.1	Irreps of the solvable wavefunctions	79
7.2.2	Van Hove singularity	80
7.3	Energy level statistics	80
7.3.1	Quantum scarring	84
8	Billiards: an analogous classical problem	85
8.1	Billiards on 2D polygons	85
8.1.1	Topology of phase space	85
8.1.2	General method to calculate genus	86
8.1.3	Demonstration of chaos	87
8.2	Billiards on 3D polyhedra	87
8.2.1	Topology of the cube phase space	87
8.2.2	Topology of other polyhedral phase spaces	90

1 Introduction

1.1 Wavefunctions

A basic postulate of quantum mechanics is that the physical state of a particle can be represented by a vector (denoted by a ket $|\cdot\rangle$ in Dirac notation) in a Hilbert space over \mathbb{C} . The dimensionality of the Hilbert space is determined by the property of the particle being examined. For example, the Hilbert space of spin states for a spin- $\frac{1}{2}$ particle has a basis $\{|\uparrow\rangle, |\downarrow\rangle\}$ and thus is two dimensional. In contrast, the Hilbert space of position states typically contains infinitely many linearly independent vectors $\{|\vec{x}\rangle \mid \vec{x} \in \mathbb{R}^3\}$ and thus is infinite dimensional.

The dual of the Hilbert space is comprised of vectors denoted by bras $\langle \cdot |$ in Dirac notation. The ket space is dual to the bra space in the sense that left multiplication of a ket by a bra provides the inner product operation of the Hilbert space. In general, we assume that any particle state ket $|\alpha(t)\rangle$ is always normalized to unity, i.e. $\langle \alpha(t)|\alpha(t)\rangle = 1$ for all $t \in \mathbb{R}$. Furthermore, for a particle with normalized state ket $|\alpha(t)\rangle$, the wave function is defined as

$$\langle \vec{x}|\alpha(t)\rangle = \psi_\alpha(\vec{x}, t).$$

The wavefunction $\psi_\alpha(\vec{x}, t)$ can alternatively be viewed as a mapping $\mathbb{R}^3 \times \mathbb{R} \rightarrow \mathbb{C}$. A practical interpretation of a particle's wavefunction is that $|\psi_\alpha(\vec{x}, t)|^2$ is the probability density of the particle's position. In this paper, we will examine the wavefunctions of particles governed by the free particle Hamiltonian. Then Schrödinger's equation gives the partial differential equation satisfied by the wavefunction:

$$i\hbar \frac{\partial}{\partial t} \psi_{\alpha,t}(\vec{x}, t) = \hat{H} \psi_\alpha(\vec{x}, t) = \left(-\frac{\hbar^2}{2m} \nabla^2 + V \right) \psi_\alpha(\vec{x}, t).$$

Conveniently, the Schrödinger equation is separable in the variables \vec{x} and t . Furthermore, due to the finite spatial dimensions of the surfaces considered in this paper, we expect the particle's energy spectrum to be discrete. Then we may write the wavefunction in the form

$$\psi_\alpha(\vec{x}, t) = \sum_n c_n \psi_n(\vec{x}) e^{-iE_n t/\hbar}$$

where $c_n \in \mathbb{C}$ are complex coefficients, E_n are the energies in the energy spectra, and the functions $\psi_n(\vec{x}) : \mathbb{R}^3 \rightarrow \mathbb{C}$ satisfy the time-independent Schrödinger equation:

$$\hat{H} \psi_n(\vec{x}) = \left(-\frac{\hbar^2}{2m} \nabla^2 + V \right) \psi_n(\vec{x}) = E_n \psi_n(\vec{x}).$$

For notational simplicity, we will work in “natural” units by taking $\hbar = 1$ and $m = \frac{1}{2}$. For computational simplicity we will mostly work with the free particle Hamiltonian by setting $V = 0$ so that the time-independent Schrödinger equation simply becomes the Helmholtz equation:

$$\nabla^2 \psi_n(\vec{x}) = -E_n \psi_n(\vec{x}) = -|k_n|^2 \psi_n(\vec{x})$$

where \vec{k}_n is the wave vector of the particle whose wavefunction is given by the energy eigenfunction $\psi_n(\vec{x})$.

A problem of interest to physicists is computing the wavefunctions of particles whose position is confined to some 2-dimensional surface in \mathbb{R}^3 . In general, directly solving Schrödinger's equation for particles on surfaces with non-zero curvature is quite difficult. However, solutions to Schrödinger's

equation for many simple hamiltonians are well studied in the case of surfaces with zero curvature such as flat planes.

In this paper we seek to lessen this difference in understanding by examining the wavefunctions of particles confined to various polyhedral surfaces. Polyhedral surfaces are particularly well suited for study since their surfaces have vanishing curvature (apart from a finite number of singularities), so Schrödinger's equation can be solved relatively easily on them, yet in the limit of high tessellation, a polyhedral surface well approximates a curved surface. The study of wavefunctions on polyhedral surfaces also has relevant applications to polyhedral nanoparticles [1–3].

1.2 Polyhedral surfaces

Throughout this section, we use the term “curvature” as a shorthand to refer to the Gaussian curvature K of a smooth 2D-manifold via the standard mathematical definition. In general, any smooth surface, regardless of its genus or curvature can be flattened via homeomorphism so that its curvature is everywhere zero except for several singular points [4]. For example, the sphere can be flattened into a cube (or any of the regular polyhedra). See Fig. (1).

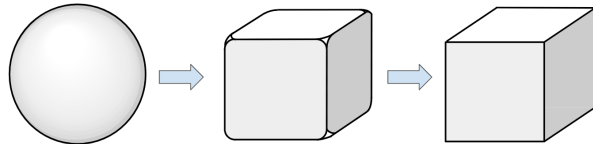


Figure 1: A sphere can be flattened into a cube by concentrating all of the curvature at the vertices of the cube.

The relevant homeomorphism can be described informally as a radial projection of one surface onto the other. For example, the mapping $f : [-1, 1]^3 \rightarrow S^2$ defined as

$$f(x, y, z) = \frac{(x, y, z)}{\sqrt{x^2 + y^2 + z^2}}$$

is a homeomorphism from the sphere S^2 to the cube $[-1, 1]^3 \subset \mathbb{R}^3$. A similar homeomorphism with S^2 can be defined for any convex polyhedron. Thus, the sphere and all convex polyhedra are topologically equivalent and share the same genus $g = 0$. Then by the Gauss-Bonnet Theorem [5],

$$\oint_S K dA = 4\pi(1 - g),$$

the surface integral of the curvature must be 4π for all convex polyhedra. The curvature on polyhedral surfaces is zero on all facial interiors. The curvature also vanishes on the interiors of all edges, since any interior point of any edge has an open neighborhood isometric to an open set in Euclidean space \mathbb{R}^2 (see Fig. 2).

However, the curvature at the vertices is non-vanishing. In particular, to satisfy the Gauss-Bonnet Theorem, the curvatures at the vertices must be delta functions whose coefficients sum to 4π . Thus, for a regular polyhedron with V vertices, symmetry requires that the curvature be $\frac{4\pi}{V}\delta(\vec{v}_i)$ at each vertex \vec{v}_i . Therefore, the flattening process can be understood intuitively as concentrating the total surface curvature of the sphere into V singularities.

Another method to determine the curvature singularities is to notice that the vertices of the polyhedron correspond to conical singularities in the flat metric. That is, a small open neighborhood of the

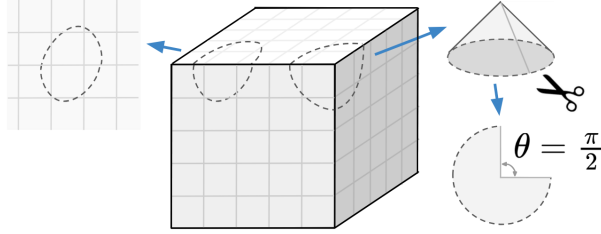


Figure 2: The interiors of the edges of the cube have zero curvature since they have open neighborhoods which can be isometrically unfolded into open subsets of \mathbb{R}^2 . The vertices are isometric to a cone with cone angle $\theta = \frac{\pi}{2}$ in the case of a cube.

vertex is isometric to a cone with cone angle determined by cutting the cone along a straight ray from the vertex and flattening the cone onto Euclidean space \mathbb{R}^2 . Since the vertices of the cube are the meeting point of three corners of a square-shaped faces with angle $\frac{\pi}{2}$ it is clear that the cone angle is $2\pi - 3 \cdot \frac{\pi}{2} = \frac{\pi}{2}$. In the same manner we can compute the conical singularities of all the regular polyhedra. One advantage of this method for calculating conical singularities is that it can also be applied to non-regular polyhedra as well.

Later, we will also find it useful to consider the symmetry groups of each polyhedron. A more detailed discussion of the polyhedral symmetry groups is given in Section 3.2. For reference, we tabulate several useful properties of various polyhedra in Tables 1 and 2.

	Tetrahedron	Cube	Octahedron	Dodecahedron	Icosahedron
Illustration					
Faces	4	6	8	12	20
Vertices	4	8	6	20	12
Conical singularity	π	$\frac{\pi}{2}$	$\frac{2\pi}{3}$	$\frac{\pi}{5}$	$\frac{\pi}{3}$
Symmetry group	T_d	O_h	O_h	I_h	I_h

Table 1: Properties of the regular polyhedra.

	Square prism	Rectangular prism
Illustration		
Faces	6	6
Vertices	8	8
Conical singularity	$\frac{\pi}{2}$	$\frac{\pi}{2}$
Symmetry group	D_{4h}	D_{2h}

Table 2: Properties of some non-regular polyhedra.

1.3 Setup and boundary conditions

The five regular polyhedra are the tetrahedron, cube, octahedron, dodecahedron, and icosahedron. So far, the complete set of eigenfunctions and eigenvalues of a free particle confined to the surface of a tetrahedron has been solved in [6] but to the best of our knowledge there is no existing literature for the other four regular polyhedra or for non-regular polyhedra. Later, we will find the solvable states on the remaining polyhedra by generalizing the approach used on the tetrahedron by [6].

Any polyhedral surface can be smoothly unfolded onto a net in the \mathbb{R}^2 plane by cutting along certain edges of the polyhedron (see Figure 3). Then, solving for the eigenstates of a free particle on a polyhedron is equivalent to solving the Helmholtz equation on \mathbb{R}^2 after applying suitable boundary conditions to ensure continuity and smoothness of the function across all edges and vertices of the polyhedron.

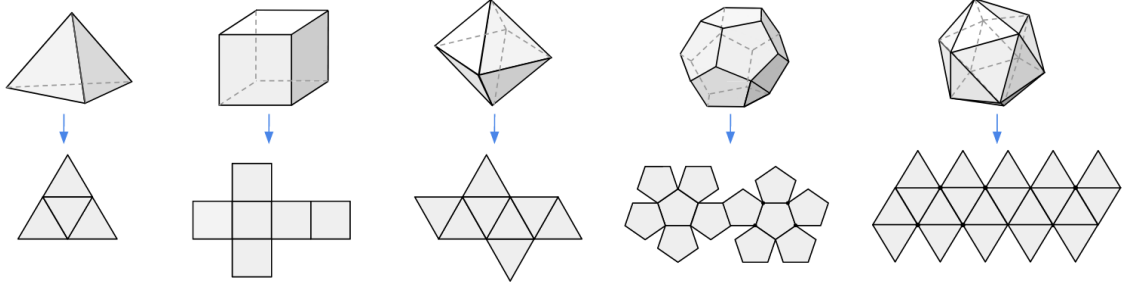


Figure 3: The regular polyhedra can all be unfolded into nets in \mathbb{R}^2 .

To provide a concrete example, we will consider the cube case and explicitly write out all of the required boundary conditions. The cube unfolding that we will work with is given in Fig. (4).

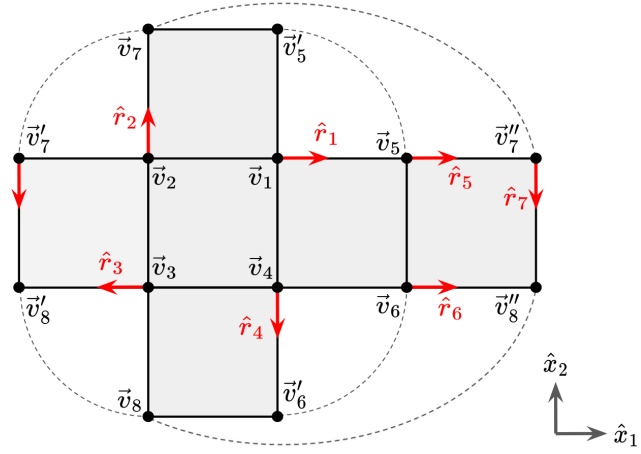


Figure 4: The net of an unfolded cube. The vertices that are connected after folding are indicated by dashed curves on the figure and have the same numeric subscript. The red vectors \vec{r}_n will be used to set the boundary conditions ensuring that wavefunctions are smooth across edges of the cube.

Fix the side length of the squares to be L , and let $C_\theta : \mathbb{R}^2 \rightarrow \mathbb{R}^2$ be the linear transformation that enacts counterclockwise rotation about the origin in the (x_1, x_2) plane by θ . Then solving the Helmholtz equation for a particle on a cube is equivalent to solving the same equation for a wave propagating in \mathbb{R}^2 with the following boundary conditions to ensure continuity on the cube:

- $\psi(\vec{v}_i + \alpha \hat{r}_i) = \psi(\vec{v}_i + \alpha C_{\pi/2} \hat{r}_i)$ for $i \in \{1, 2, 3, 4\}$
- $\psi(\vec{v}_i + \alpha \hat{r}_i) = \psi(\vec{v}_i + \alpha C_{\pi/2}^2 \hat{r}_i)$ for $i \in \{5, 6\}$
- $\psi(\vec{v}_i + \alpha \hat{r}_i) = \psi(\vec{v}_i + \alpha \hat{r}_i)$ for $i \in \{7\}$

as well as the following boundary conditions to ensure smoothness on the cube:

- $\frac{\partial \psi}{\partial x_j} \Big|_{v_i + \alpha \hat{r}_i} = \frac{\partial \psi}{\partial (C_{\pi/2} x_j)} \Big|_{v_i + \alpha C_{\pi/2} \hat{r}_i}$ for $i \in \{1, 2, 3, 4\}$ and $j \in \{1, 2\}$
- $\frac{\partial \psi}{\partial x_j} \Big|_{v_i + \alpha \hat{r}_i} = \frac{\partial \psi}{\partial (C_{\pi/2}^2 x_j)} \Big|_{v_i + \alpha C_{\pi/2}^2 \hat{r}_i}$ for $i \in \{5, 6\}$ and $j \in \{1, 2\}$

- $\frac{\partial \psi}{\partial x_j} \Big|_{v_i + \alpha \hat{r}_i} = \frac{\partial \psi}{\partial x_j} \Big|_{v_i + \alpha \hat{r}_i}$ for $i \in \{7\}$ and $j \in \{1, 2\}$

where the conditions above hold for all $\alpha \in [0, 1]$. Analogous boundary conditions can be imposed on the nets of the remaining regular polyhedra. To reduce repetitiveness in calculations we will next provide a general approach to solving the Helmholtz equation on the nets of any regular polyhedra. Then we will proceed to examine each polyhedron separately.

2 Solvable wavefunctions

2.1 General properties

The solutions of the Helmholtz equation for wave propagating in \mathbb{R}^2 must be a linear combination of solutions of the form $e^{i\vec{k}\cdot\vec{x}}$ where $\vec{k} = (k_1, k_2)$ is the wavevector of the wavefunction. For such waves propagating on a polyhedral surface the wave vector must rotate by an angle which is some multiple of the conical singularity of the polyhedron each time the wave encounters the boundary of the net. See Fig. (5). Alternatively, the conical singularity angle can be viewed as the angle between the initial vector \vec{k} and the image of the vector \vec{k} after parallel transport around a loop on the polyhedral surface containing one vertex.

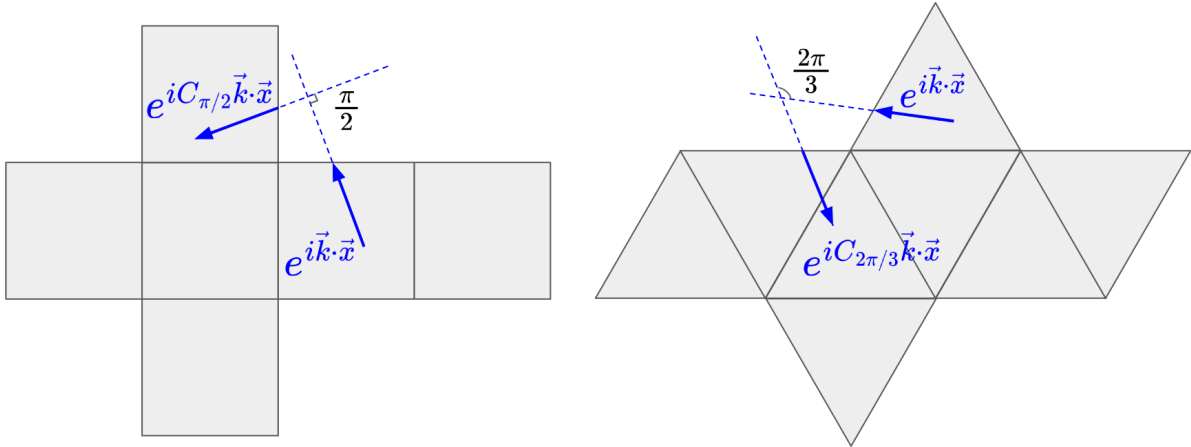


Figure 5: Propagation of a wave $e^{i\vec{k}\cdot\vec{x}}$ after crossing a boundary on the net of a cube (left) and the net of an octahedron (right). Recall that a cube has conical singularity $\frac{\pi}{2}$ while the octahedron has conical singularity $\frac{2\pi}{3}$.

Thus, for a polyhedron with conical singularity θ satisfying $N_\theta \equiv \frac{2\pi}{\theta}$ we apply the following ansatz:

$$\psi(\vec{x}) = \sum_{n=0}^{N_\theta-1} a_n e^{iC_\theta^n \vec{k}\cdot\vec{x}}. \quad (1)$$

where $a_n \in \mathbb{C}$ are complex coefficients. The boundary conditions together with the Helmholtz equation impose further restrictions on the general form of the ansatz. To organize our calculations clearly, we present these conditions in the form of propositions and corollaries as follows.

Proposition 1. (*Vanishing derivative condition*) *If $\psi(\vec{x}) = \psi(x_1, x_2)$ is a wavefunction for a particle confined to any regular polyhedral surface, then $\partial_{x_1}\psi(\vec{v}_i) = \partial_{x_2}\psi(\vec{v}_i) = 0$ at all vertices \vec{v}_i of the polyhedron.*

Proof. Choose any vertex \vec{v}_i of the polyhedron. Then unfold the polyhedron in a manner such that exactly one of the edges meeting at \vec{v}_i is cut while all the other edges remain uncut. Any sufficiently small open neighborhood of \vec{v}_i would then be isometric to a flat cone with cone angle equal to the polyhedron's conical singularity θ . For all regular polyhedra except the octahedron we can write $\theta = \frac{\pi}{m}$ where $m \in \{1, 2, 3, 5\}$ (see Fig. (6)). We will first prove the theorem for non-octahedral polyhedra ($\theta = \frac{\pi}{m}$) and then consider the special case of the octahedron ($\theta = \frac{2\pi}{3}$).

Let \hat{r}_1 and $\hat{r}_2 = C_\theta \hat{r}_1$ be unit vectors whose directions are parallel to the cut edges of the polyhedron as shown in Fig. (6). For simplicity, we orient our $x_1 x_2$ coordinate system such that $\hat{x}_1 = \hat{r}_1$. Next,

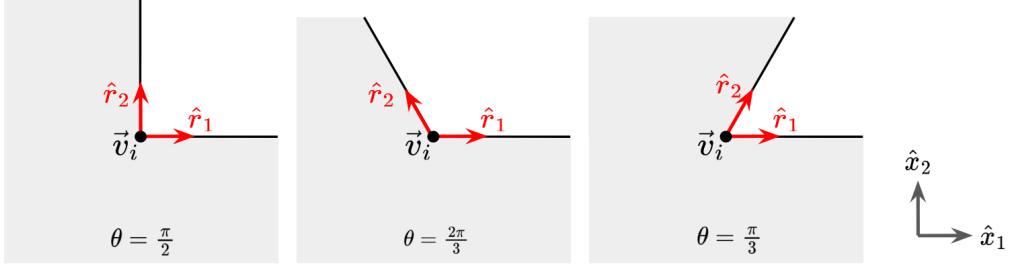


Figure 6: A neighborhood of the vertex \vec{v}_i after unfolding of the polyhedra for the cases of $\theta = \frac{\pi}{2}$ (cube), $\theta = \frac{2\pi}{3}$ (octahedron), and $\theta = \frac{\pi}{3}$ (dodecahedron)

to ensure that the wavefunction is smooth along the cut boundary we enforce the following boundary condition:

$$\partial_{\hat{u}}\psi(\vec{v}_i + \alpha\hat{r}_1) = \partial_{C_\theta\hat{u}}\psi(\vec{v}_i + \alpha\hat{r}_2) \text{ for all } \alpha = [0, L] \text{ and all unit vectors } \hat{u} \in \mathbb{R}^2 \quad (2)$$

where L is the side length of each polyhedral face. Here, the notation $\partial_{\hat{u}}$ denotes a directional derivative in the $\hat{u} \in \mathbb{R}^2$ direction. From this boundary equation we can obtain the following sequence of equations by sequentially setting $\hat{u} = \{\hat{x}_j, C_\theta\hat{x}_j, C_\theta^2\hat{x}_j, \dots, C_\theta^n\hat{x}_j\}$ where $j \in \{1, 2\}$ and $\alpha = 0$:

$$\partial_{\hat{x}_j}\psi(\vec{v}_i) = \partial_{C_\theta\hat{x}_j}\psi(\vec{v}_i) = \partial_{C_\theta^2\hat{x}_j}\psi(\vec{v}_i) = \dots = \partial_{C_\theta^n\hat{x}_j}\psi(\vec{v}_i). \quad (3)$$

Since $C_\theta^n\hat{x}_j = -\hat{x}_j$ then the equations above imply that $\partial_{\hat{x}_j}\psi(\vec{v}_i) = \partial_{-\hat{x}_j}\psi(\vec{v}_i) = -\partial_{\hat{x}_j}\psi(\vec{v}_i)$ from which it is necessarily true that $\partial_{\hat{x}_j}\psi(\vec{v}_i) = 0$ where $j \in \{1, 2\}$.

For the octahedron, applying $\hat{u} = \{\hat{x}_j, C_{2\pi/3}\hat{x}_j, C_{2\pi/3}^2\hat{x}_j\}$ with $\alpha = 0$ to the boundary conditions gives the sequence of equations $\partial_{\hat{x}_j}\psi(\vec{v}_i) = \partial_{C_{2\pi/3}\hat{x}_j}\psi(\vec{v}_i) = \partial_{C_{2\pi/3}^2\hat{x}_j}\psi(\vec{v}_i)$ but since $\hat{x}_j = -\frac{1}{\sqrt{2}}(C_{2\pi/3}\hat{x}_j + C_{2\pi/3}^2\hat{x}_j)$ then

$$\begin{aligned} \partial_{\hat{x}_j}\psi(\vec{v}_i) &= -\frac{1}{\sqrt{2}}(\partial_{C_{2\pi/3}\hat{x}_j}\psi(\vec{v}_i) + \partial_{C_{2\pi/3}^2\hat{x}_j}\psi(\vec{v}_i)) \\ &= -\frac{1}{\sqrt{2}}\partial_{\hat{x}_j}\psi(\vec{v}_i) \end{aligned}$$

from which it follows that $\partial_{\hat{x}_j}\psi(\vec{v}_i) = 0$ for $j \in \{1, 2\}$, as desired. \square

In upcoming calculations, it will also be convenient to work with a generalization of the coefficients a_n in Eqn. (1). In particular, for a wavefunction $\psi(\vec{x}) = \sum_{n=0}^{N_\theta-1} a_n e^{iC_\theta^n \vec{k} \cdot \vec{x}}$ we define for any vertex \vec{v} of the polyhedra the generalized coefficients

$$\tilde{a}_{n,\vec{v}} \equiv a_n e^{iC_\theta^n \vec{k} \cdot \vec{v}}$$

for any $n \in (1, 2, 3, \dots, N_\theta - 1)$. It follows that

$$\psi(\vec{v} + \vec{x}) = \sum_{n=0}^{N_\theta-1} a_n e^{iC_\theta^n \vec{k} \cdot (\vec{v} + \vec{x})} \sum_{n=0}^{N_\theta-1} \tilde{a}_{n,\vec{v}} e^{iC_\theta^n \vec{k} \cdot \vec{x}}.$$

The vanishing derivative condition imposes some restrictions on the possible values of the coefficients $\tilde{a}_{n,\vec{v}}$.

Corollary 1.1. *Let $\psi(\vec{x}) = \sum_{n=0}^{N_\theta-1} a_n e^{iC_\theta^n \vec{k} \cdot \vec{x}}$ be a wavefunction for a particle confined to a regular*

polyhedral surface. Then in the cases $N_\theta = 2, 3, 4$, or 6 , the vanishing derivative condition requires that

- $N_\theta = 2 : \tilde{a}_{n,\vec{v}} = \tilde{a}_{\text{mod}(n+1,2),\vec{v}}$
- $N_\theta = 3 : \tilde{a}_n = \tilde{a}_{\text{mod}(n+1,3),\vec{v}}$
- $N_\theta = 4 : \tilde{a}_n = \tilde{a}_{\text{mod}(n+2,4),\vec{v}}$
- $N_\theta = 6 : \tilde{a}_n + \tilde{a}_{\text{mod}(n+1,6)} = \tilde{a}_{\text{mod}(n+4,6)} + \tilde{a}_{\text{mod}(n+5,6),\vec{v}}.$

Proof. After fixing some vertex \vec{v} we can unfold the polyhedron so that only one of the edges at \vec{v} is cut. For further convenience, we can rotate the unfolding in the (x_1, x_2) plane so that the edges of the unfolded polyhedron at \vec{v} are parallel to \hat{x}_1 and $C_\theta \hat{x}_1$. Then the vanishing derivative condition requires that $\partial_{C_\theta^{\tilde{n}} \hat{x}_j} \psi(\vec{v} + \alpha C_\theta^{\tilde{m}} \hat{x}_1)|_{\alpha=0} = 0$ where $j \in \{1, 2\}$ and $\tilde{m}, \tilde{n} \in \{0, 1, 2, \dots, N_\theta - 1\}$. We compute the directional derivative as follows

$$\begin{aligned} \partial_{C_\theta^{\tilde{n}} \hat{x}_j} \psi(\vec{v} + \alpha C_\theta^{\tilde{m}} \hat{x}_1) &= \partial_{C_\theta^{\tilde{n}} \hat{x}_j} \sum_{n=0}^{N_\theta-1} \tilde{a}_{n,\vec{v}} e^{i\alpha C_\theta^n \vec{k} \cdot C_\theta^{\tilde{m}} \hat{x}_1} \\ &= \partial_{\hat{x}_j} \sum_{n=0}^{N_\theta-1} \tilde{a}_n e^{i\alpha C_\theta^{n-\tilde{m}+\tilde{n}} \vec{k} \cdot \hat{x}_1} \\ &= \sum_{n=0}^{N_\theta-\tilde{n}} \tilde{a}_{n,\vec{v}} (C_\theta^{n-\tilde{m}+\tilde{n}} \vec{k})_j e^{i\alpha C_\theta^{n-\tilde{m}+\tilde{n}} \vec{k} \cdot \hat{x}_1} \\ &= \sum_{n=0}^{N_\theta-1} \tilde{a}_{\text{mod}(n-\tilde{n}, N_\theta), \vec{v}} (C_\theta^{n-\tilde{m}} \vec{k})_j e^{i\alpha C_\theta^{n-\tilde{m}} \vec{k} \cdot \hat{x}_1}. \end{aligned}$$

Then after setting $\tilde{m} = 0$ and $\alpha = 0$ we find that

$$\sum_{n=0}^{N_\theta-1} \tilde{a}_{\text{mod}(n-\tilde{n}, N_\theta), \vec{v}} (C_\theta^n \vec{k})_j = 0,$$

which implies that all cyclic permutations of the vector $(\tilde{a}_{0,\vec{v}}, \tilde{a}_{1,\vec{v}}, \tilde{a}_{2,\vec{v}}, \dots, \tilde{a}_{N_\theta-1,\vec{v}})$ are orthogonal to the vector space spanned by $(\vec{k}_j, (C_\theta \vec{k})_j, \dots, (C_\theta^{N_\theta-1} \vec{k})_j)$ for $j \in \{1, 2\}$. It is straightforward to verify that the vectors $(1, -1)$, $(1, -1, 0)$, $(1, 0, -1, 0)$, and $(1, 1, 0, -1, -1, 0)$ are contained in the span of $\{(\vec{k}_j, (C_\theta \vec{k})_j, \dots, (C_\theta^{N_\theta-1} \vec{k})_j)\}$ for $N_\theta = 2, 3, 4$, and 6 , respectively. For instance, one could evaluate the vectors $(\vec{k}_j, (C_\theta \vec{k})_j, \dots, (C_\theta^{N_\theta-1} \vec{k})_j)$ in the basis $\{\hat{k}_j\}$. The orthogonality conditions then impose the given restrictions on the coefficients $\tilde{a}_{n,\vec{v}}$. \square

We will always place the origin of our $\{x_i\}$ coordinate system at a vertex. Then, an immediate result is that $a_0 = a_1$ for the tetrahedron and $a_0 = a_1 = a_2$ for the octahedron. Eventually, we will find that a similar relation holds for the coefficients a_n for the cube and icosahedron but this requires the enforcement of additional boundary conditions.

Corollary 1.2. *Enforcing the boundary conditions $\psi(\alpha \hat{x}_1) = \psi(\alpha \hat{x}_2)$ and $\partial_{\hat{x}_2} \psi(\alpha \hat{x}_1) = \partial_{-\hat{x}_1} \psi(\alpha \hat{x}_2)$ for all $\alpha \in [0, L]$ for the cube in addition to the vanishing derivative condition at the origin requires that $a_0 = a_1 = a_2 = a_3$.*

Proof. Since $a_0 = a_2$ and $a_1 = a_3$ we can write the cube wavefunction (up to normalization) as

$$\psi(\vec{x}) = a_0 \cos(k_1 x_1 + k_2 x_2) + a_1 \cos(-k_2 x_1 + k_1 x_2).$$

If $k_1 = k_2 = 0$ then the wavefunction is a trivial constant. If $k_1 = 0$ while $k_2 \neq 0$ then the condition $\psi(\alpha\hat{x}_1) = \psi(\alpha\hat{x}_2)$ becomes $a_0 + a_1 \cos(k_2\alpha) = a_0 \cos(k_2\alpha) + a_1$ which forces $a_0 = a_1$ by separation of k_2 -dependent and k_2 -independent parts. Similarly, if $k_1 = 0$ while $k_0 \neq 0$ then $\psi(\alpha\hat{x}_1) = \psi(\alpha\hat{x}_2)$ also forces $a_0 = a_1$. Lastly, if $k_1 \neq 0$ and $k_2 \neq 0$ we consider the derivatives

$$\begin{aligned}\partial_{\hat{x}_2} \psi(\alpha\hat{x}_1) &= -a_0 k_2 \sin(k_1\alpha) + a_1 k_1 \sin(k_2\alpha) \\ \partial_{-\hat{x}_1} \psi(\alpha\hat{x}_2) &= a_0 k_1 \sin(k_2\alpha) - a_1 k_2 \sin(k_1\alpha),\end{aligned}$$

so the condition $\partial_{\hat{x}_2} \psi(\alpha\hat{x}_1) = \partial_{-\hat{x}_1} \psi(\alpha\hat{x}_2)$ can be written

$$(a_1 - a_0) \frac{\sin(k_2\alpha)}{k_2} = (a_0 - a_1) \frac{\sin(k_1\alpha)}{k_1},$$

where we have divided by $k_1 k_2$ and re-arranged terms. It follows that $a_0 = a_1$. Thus, $a_0 = a_1 = a_2 = a_3$ for the cube as desired. \square

Corollary 1.3. *For the icosahedron, enforcing the boundary conditions $\psi(\alpha\hat{x}_1) = \psi(\alpha C_{\pi/3}\hat{x}_1)$ and $\partial_{C_{\pi/3}\hat{x}_1} \psi(\alpha\hat{x}_1) = \partial_{C_{\pi/3}\hat{x}_1} \psi(\alpha C_{\pi/3}\hat{x}_1)$ for all $\alpha \in [0, L]$ in addition to the vanishing derivative condition at the origin requires that $a_0 = a_1 = a_2 = a_3 = a_4 = a_5$.*

Proof. We note that it suffices to consider \vec{k} such that $k_1 \geq 0$ and $k_2 \leq \sqrt{3}k_1$ because all other wave vectors \vec{k} are simply rotations of such wave vectors by multiples of $\frac{\pi}{3}$ (aside from the trivial wavefunction with $\vec{k} = \vec{0}$). Further, rotations of \vec{k} by multiples of $\frac{\pi}{3}$ simply correspond to permutations of the indices a_n . Next, note that the boundary condition $\psi(\alpha\hat{x}_1) = \psi(\alpha C_{\pi/3}\hat{x}_1)$ can be written

$$\sum_{n=0}^6 a_n e^{i(C_{\pi/3}^n \vec{k})_1 \alpha} = \sum_{n=0}^6 a_{\text{mod}(n-1,6)} e^{i(C_{\pi/3}^n \vec{k})_1 \alpha}.$$

If $k_2 \neq 0$, then $(C_{\pi/3}^n \vec{k})_1$ is distinct for each $n \in \{0, 1, 2, \dots, 5\}$, so we must have $a_n = a_{\text{mod}(n-1,6)}$ which forces $a_0 = a_1 = a_2 = \dots = a_5$. If $k_2 = 0$ then the wavefunction becomes

$$\psi(\alpha\hat{x}_1) = a_0 e^{ik_1\alpha} + (a_1 + a_5) e^{i\frac{1}{2}k_1\alpha} + (a_2 + a_4) e^{-i\frac{1}{2}k_1\alpha} + a_3 e^{-ik_1\alpha},$$

so the boundary condition $\psi(\alpha\hat{x}_1) = \psi(\alpha C_{\pi/3}\hat{x}_1)$ forces $a_0 = a_5$, $a_1 + a_5 = a_0 + a_4$, $a_2 + a_4 = a_1 + a_3$, and $a_2 + a_3 = a_5 + a_0$. Together with the vanishing derivative condition at the origin, this forces $a_0 = a_2 = a_3 = a_5$ and $a_1 = a_4$. We can then write the wavefunction as

$$\psi(\vec{x}) = a_0 \cos(k_1 x_1) + a_1 \cos\left(\frac{1}{2}k_1 x_1 + \frac{\sqrt{3}}{2}k_1 x_2\right) + a_0 \cos\left(-\frac{1}{2}k_1 x_1 + \frac{\sqrt{3}}{2}k_1 x_2\right).$$

Then the condition $\partial_{C_{\pi/3}\hat{x}_1} \psi(\alpha\hat{x}_1) = \partial_{C_{\pi/3}\hat{x}_1} \psi(\alpha C_{\pi/3}\hat{x}_1)$ reduces to

$$-\frac{1}{2}k_1 a_0 \sin(k_1\alpha) - k_1(a_0 + a_1) \sin\left(\frac{1}{2}k_1\alpha\right) = -\frac{1}{2}a_1 k_1 \sin(k_1\alpha) - \frac{1}{2}k_1 a_0 \sin\left(\frac{1}{2}k_1\alpha\right)$$

for all $\alpha \in [0, L]$ which forces $a_0 = a_1$. Then $a_0 = a_1 = a_2 = \dots = a_5$, as desired. \square

Lastly, the following results will be useful for checking that the polyhedron wavefunctions satisfy all the necessary boundary conditions.

Proposition 2. *If $\tilde{a}_{1,\vec{v}} = \tilde{a}_{2,\vec{v}} = \dots = \tilde{a}_{N_\theta-1,\vec{v}}$ for some vertex \vec{v} , then the wavefunction $\psi(\vec{x})$ is invariant under rotations by C_θ around \vec{v} where θ is the conical singularity of the polyhedron.*

Proof. It is clear from inspection that for any vector \vec{x} the wavefunction

$$\psi(\vec{v} + \vec{x}) = \sum_{n=0}^{N_\theta-1} a_n e^{iC_\theta^n \vec{k} \cdot (\vec{v} + \vec{x})} = \sum_{n=0}^{N_\theta-1} \tilde{a}_{n,\vec{v}} e^{iC_\theta^n \vec{k} \cdot \vec{x}}$$

is invariant under the transformation $\vec{x} \rightarrow C_\theta \vec{x}$. \square

Lastly, since the wavefunction $\psi(\vec{x})$ must be smooth, an immediate corollary of this proposition is as follows:

Corollary 2.1. *If $\tilde{a}_{1,\vec{v}} = \tilde{a}_{2,\vec{v}} = \dots = \tilde{a}_{N_\theta-1,\vec{v}}$ for some vertex \vec{v} , then $\partial_{\hat{x}_1} \psi(\vec{x})|_{\vec{x}=\vec{v}} = \partial_{\hat{x}_2} \psi(\vec{x})|_{\vec{x}=\vec{v}} = 0$.*

In the following sections we will specialize to cases covering each type of polyhedron. Note that we will not study the pentagon-faced dodecahedron in this paper due to the lack of a lattice respecting pentagonal symmetry which prohibits a numerical study dodecahedron wavefunctions. We will, however, study the remaining regular polyhedra as well as the square and rectangular prisms in depth.

2.2 Tetrahedron

For the tetrahedron, we use the unfolding illustrated below in Fig. (7).

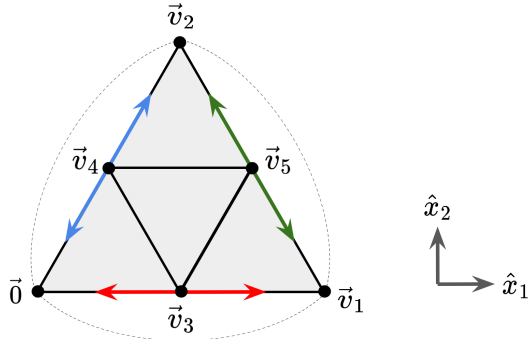


Figure 7: An unfolding of the tetrahedron with side length L and vertices at $\vec{v}_1 = (L, 0)$ and $\vec{v}_2 = (\frac{L}{2}, \frac{L\sqrt{3}}{2})$. The vertices joined by the dotted line are joined together after folding. Edges that are identified after folding are indicated by colored arrows.

The tetrahedron has conical singularity, $\theta = \pi$, so setting $a_0 = a_1$ in the ansatz in Eqn. (1) gives

$$\psi(\vec{x}) = A \cos(k_1 x_1 + k_2 x_2).$$

for some normalization constant A . First, note that $\psi(\vec{x})$ obtains an extremal value at the origin. Since the origin is identified with the vertices at $\vec{v}_1 = (2L, 0)$ and $\vec{v}_2 = (L, \sqrt{3}L)$, then we require that $a = \tilde{a}_{\vec{v}_i}$ for $i \in \{1, 2\}$ to ensure that the wavefunction is well-defined. Equivalently, we must have

$$\vec{k} \cdot \vec{v}_i = 2\pi m_i$$

for $i \in \{1, 2\}$ where m_i are any integers. This system of equations quantizes the wavevector \vec{k} as

$$\vec{k} = \frac{\pi}{L} \left(m_1, \frac{2m_2 - m_1}{\sqrt{3}} \right) = \frac{\pi}{L} \left(m + n, \frac{m - n}{\sqrt{3}} \right)$$

where we have set $m = m_2$ and $n = m_1 - m_2$ and m and n can be any integers. Thus, the tetrahedron wavefunction is

$$\psi_{m,n}(\vec{x}) = A \cos \left[\frac{\pi}{L} \left((m+n)x_1 + \frac{(m-n)x_2}{\sqrt{3}} \right) \right]$$

where m and n can be any integers or

$$\psi_{n_1,n_2}(\vec{x}) = A \cos \left[\frac{\pi}{L} \left(n_1 x_1 + \frac{n_2 x_2}{\sqrt{3}} \right) \right] \quad (4)$$

where n_1 and n_2 must be integers of the same parity. Our wavefunctions and quantization condition agree with those found in [6]. Lastly, we note that the condition $\vec{k} \cdot \vec{v}_i = 2\pi m_i$ ensures that $\vec{k} \cdot \vec{v}_3 = \pi m_1$ and $\vec{k} \cdot \vec{v}_4 = \pi m_2$ where $\vec{v}_3 = \frac{1}{2}\vec{v}_1$ and $\vec{v}_4 = \frac{1}{2}\vec{v}_2$ as illustrated in Fig. (7). It follows that $\vec{k} \cdot \vec{v}_5 = \pi(m_1 + m_2)$, so then $\tilde{a}_{1,\vec{v}_j} = \tilde{a}_{2,\vec{v}_j}$, for $j \in \{3, 4, 5\}$ so $\psi(x)$ is invariant under rotations by π about any of the vertices \vec{v}_3, \vec{v}_4 , and \vec{v}_5 . Thus, all edges that are glued together during folding are correctly identified with smooth derivatives over the edges, so the wavefunctions satisfy all boundary conditions on the tetrahedron net (see Fig. (7)).

It is also proved in [6] that this set of tetrahedron eigenmodes is complete and each mode has energy

$$E = k^2 = \frac{(2\pi)^2}{3L^2} (m^2 + mn + n^2).$$

The modes $\psi_{m,n}, \psi_{-m-n,m}$, and $\psi_{n,-m-n}$ are degenerate and correspond to rotations of \vec{k} by $\frac{2\pi}{3}$. Similarly, $\psi_{n,m}$ is also degenerate with $\psi_{m,n}$ and corresponds to the symmetry of the wave vector under reflections about the line $x_2 = 1$. Several examples of tetrahedron eigenmodes are plotted in Figs. (8) and (9).

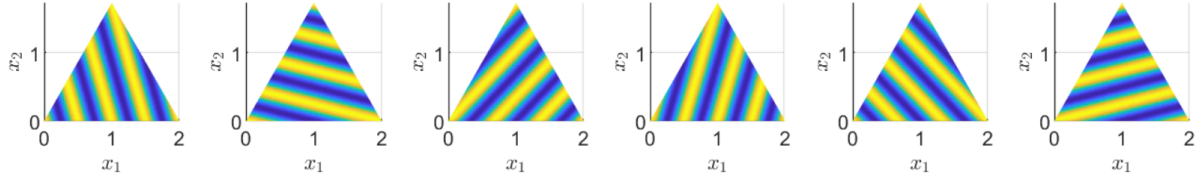


Figure 8: From left to right: degenerate tetrahedron eigenmodes $\psi_{m,n}$, $\psi_{-m-n,m}$, $\psi_{n,-m-n}$, $\psi_{n,m}$, $\psi_{-n-m,n}$, and $\psi_{m,-n-m}$ with $n = 2$ and $m = 3$.

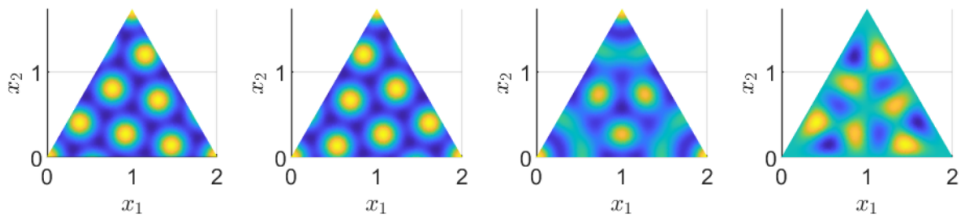


Figure 9: From left to right: a threefold superposition of degenerate tetrahedron eigenmodes $\psi_1 = \psi_{m,n} + \psi_{-n-m,m} + \psi_{n,-m-n}$, a threefold superposition of degenerate eigenmodes $\psi_2 = \psi_{n,m} + \psi_{-n-m,m} + \psi_{n,-m-n}$, symmetric superposition $\psi_1 + \psi_2$, anti-symmetric superposition $\psi_1 - \psi_2$ with $n = 2$ and $m = 3$.

2.3 Cube

We will use the cube net illustrated in Fig. (10) with the origin placed at \vec{v}_1 . Recall that the cube has

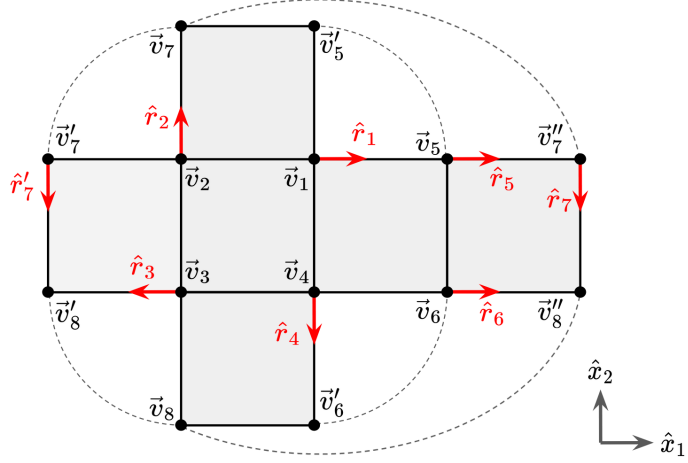


Figure 10: The net of an unfolded cube. Vertices that are identified after folding are joined by dashed lines. Edges that are identified by the wavefunction are indicated by the red arrows.

conical singularity $\theta = \frac{\pi}{2}$ and satisfies $a_0 = a_1 = a_2 = a_3$ so the wavefunction can be written as

$$\psi(\vec{x}) = A(\cos(k_1 x_1 + k_2 x_2) + \cos(-k_2 x_1 + k_1 x_2)).$$

for some normalization constant A . First we note that a necessary condition for a vanishing derivative at a vertex \vec{v} is that $\tilde{a}_{0,\vec{v}} = \tilde{a}_{2,\vec{v}}$ and $\tilde{a}_{1,\vec{v}} = \tilde{a}_{3,\vec{v}}$. Equivalently, $e^{i\vec{k}\cdot\vec{v}} = e^{-i\vec{k}\cdot\vec{v}}$ and $e^{iC_{\pi/2}\vec{k}\cdot\vec{v}} = e^{-iC_{\pi/2}\vec{k}\cdot\vec{v}}$, so we obtain the system of equations

$$\begin{cases} \vec{k} \cdot \vec{v} &= n_1\pi \\ C_{\pi/2}\vec{k} \cdot \vec{v} &= n_2\pi \end{cases}$$

for some integers n_1, n_2 . Using $\vec{v} = \vec{v}_5 = (L, 0)$ then gives us the explicit solution

$$\vec{k} = \frac{\pi}{L}(n_1, n_2).$$

It then follows $\psi(\vec{x})$ reaches an extremal value at $\vec{x} = \vec{v}_7'' = (2L, 0)$. Since $\vec{v}_7 = (-L, L)$ is identified with \vec{v}_7'' then $\psi(\vec{x})$ also must reach an extremal value at $\vec{x} = \vec{v}_7$. Thus $\vec{k} \cdot \vec{v}_7 = \vec{k} \cdot (-\vec{v}_5 + \vec{v}_5') = \pi(-n_1 + n_2)$ must be an even multiple of π , so n_1 and n_2 must be integers of same parity. The wavefunction ansatz then becomes

$$\psi_{n_1, n_2}(\vec{x}) = A_{n_1, n_2} \left[\cos\left(\frac{\pi}{L}(n_1 x_1 + n_2 x_2)\right) + \cos\left(\frac{\pi}{L}(n_1 x_2 - n_2 x_1)\right) \right]. \quad (5)$$

where n_1 and n_2 are any integers with same parity. Alternatively, we can define $n_1 = m + n$ and $n_2 = m - n$, and let the integers m and n vary freely. Then by using the identity $\cos(x+y) + \cos(x-y) = 2\cos(x)\cos(y)$ and absorbing constant factors into the normalization constant we alternatively write the wavefunctions as

$$\psi_{m,n}(\vec{x}) = A_{n,m} \cos\left(\frac{\pi}{L}(mx_1 + nx_2)\right) \cos\left(\frac{\pi}{L}(mx_2 - nx_1)\right). \quad (6)$$

Further, we note that the conditions that $\tilde{a}_{0,\vec{v}_5} = \tilde{a}_{2,\vec{v}_5}$ and $\tilde{a}_{0,\vec{v}'_5} = \tilde{a}_{2,\vec{v}'_5}$ ensure that $\tilde{a}_{0,\vec{v}} = \tilde{a}_{2,\vec{v}}$ for all vertices $\vec{v} = c_1\vec{v}_5 + c_2\vec{v}'_5$ since

$$\begin{aligned}\vec{k} \cdot \vec{v} - C_{\pi/2}^2 \vec{k} \cdot \vec{v} &= 2\vec{k} \cdot (c_1\vec{v}_5 + c_2\vec{v}'_5) \\ &= 2(an_1 + bn_2)\pi\end{aligned}$$

is an even multiple of π . Moreover, the condition that n_1 and n_2 have same parity ensures that $e^{i\vec{k} \cdot \vec{v}} = e^{iC_{\pi/2}\vec{k} \cdot \vec{v}}$ at all vertices $\vec{v} = c_1\vec{v}_5 + c_2\vec{v}'_5$ since

$$\begin{aligned}\vec{k} \cdot \vec{v} - C_{\pi/2} \vec{k} \cdot \vec{v} &= \vec{k} \cdot \vec{v} + \vec{k} \cdot C_{\pi/2} \vec{v} \\ &= \vec{k} \cdot (c_1\vec{v}_5 + c_2\vec{v}'_5) + \vec{k} \cdot (-c_2\vec{v}_5 + c_1\vec{v}'_5) \\ &= (c_1n_1 + c_2n_2)\pi + (c_2n_1 - c_1n_2)\pi \\ &= ((c_1 + c_2)n_1 + (c_2 - c_1)n_2)\pi\end{aligned}$$

is an even multiple of π . Thus, the wavefunctions are invariant under rotations by $\frac{\pi}{2}$ about all vertices \vec{v}_i . This allows the edges of the cube net to be identified as needed to satisfy all necessary boundary conditions (see Fig. (10)).

Next, we note that the energy spectrum of the eigenmodes is given by

$$k^2 = k_1^2 + k_2^2 = \frac{\pi^2}{L^2}(m^2 + n^2) = \frac{2\pi^2}{L^2}(n_1^2 + n_2^2). \quad (7)$$

It is then apparent that distinct pairs $(m, n) \in \mathbb{Z}^2$ do not always give distinct wavefunctions. In particular,

$$\psi_{m,n}(\vec{x}) = \psi_{-n,m}(\vec{x}) = \psi_{-m,-n}(\vec{x}) = \psi_{n,-m}(\vec{x}). \quad (8)$$

which reflects the symmetry of the wavefunction under rotations by $\frac{\pi}{2}, \pi$, and $\frac{3\pi}{2}$, respectively. Next, notice that some modes are non-degenerate: the fundamental mode $(m, n) = (0, 0)$, modes where exactly one of m or n is zero, and modes where $m = n$. If both of m and n are non-zero and non-equal then there is an a two-fold degeneracy of the mode $\psi_{m,n}$ with the mode $\psi_{-m,n}$ which reflects the symmetry of the wavefunction under reflection about the line $x_1 = x_2$. Additionally, for some relatively rare values of $N = m^2 + n^2$ where the decomposition of N into a sum of two squares is not unique, additional two-fold degeneracies would be introduced. Several examples of modes and superpositions of degenerate modes are given in Figs. (11) and (12). In Section 3.1, we will demonstrate that this set of eigenmodes is incomplete, in contrast with the tetrahedron.

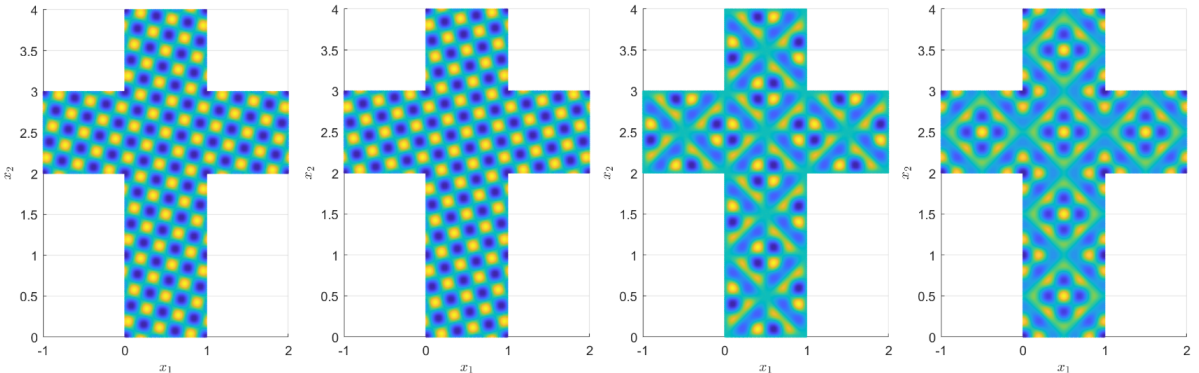


Figure 11: From left to right: plot of the degenerate modes $\psi_{2,3}$, $\psi_{2,-3}$, symmetric superposition $\psi_{2,3} + \psi_{2,-3}$, and asymmetric superposition $\psi_{2,3} - \psi_{2,-3}$.

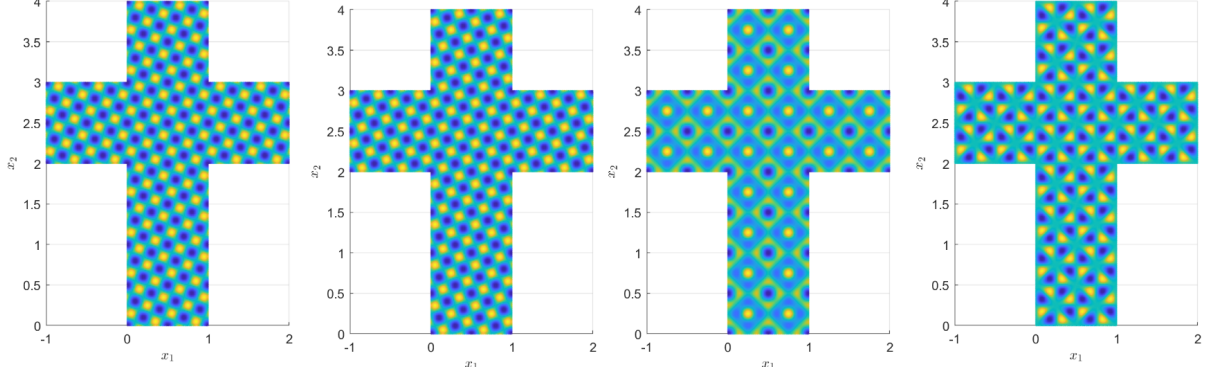


Figure 12: From left to right: plot of the degenerate modes $\psi_{2,4}$, $\psi_{2,-4}$, symmetric superposition $\psi_{2,4} + \psi_{2,-4}$, and asymmetric superposition $\psi_{2,4} - \psi_{2,-4}$.

2.4 Octahedron

Recall that the octahedron has conical singularity $\theta = \frac{2\pi}{3}$ and the vanishing derivative condition at the origin requires that $a_0 = a_1 = a_2$. Thus, we can write the ansatz as

$$\psi(\vec{x}) = a(e^{i\vec{k}\cdot\vec{x}} + e^{iC_{2\pi/3}\vec{k}\cdot\vec{x}} + e^{iC_{2\pi/3}^2\vec{k}\cdot\vec{x}})$$

The vanishing derivative condition at a vertex \vec{v} then requires that $\tilde{a}_{0,\vec{v}} = \tilde{a}_{1,\vec{v}} = \tilde{a}_{2,\vec{v}}$, so we obtain the system of equations

$$\begin{cases} (C_{2\pi/3}\vec{k} - \vec{k}) \cdot \vec{v} = 2\pi m_1 \\ (C_{2\pi/3}^{-1}\vec{k} - \vec{k}) \cdot \vec{v} = 2\pi m_2 \end{cases}$$

for some integers m_1, m_2 . For convenience, we can use $\vec{v} = (L, 0)$, so the system becomes

$$\begin{cases} -\frac{3}{2}k_1 - \frac{\sqrt{3}}{2}k_2 = \frac{2\pi}{L}m_1 \\ -\frac{3}{2}k_1 + \frac{\sqrt{3}}{2}k_2 = \frac{2\pi}{L}m_2 \end{cases}$$

which gives the solution

$$\vec{k} = \frac{2\pi}{L} \left(-\frac{m_1 + m_2}{3}, \frac{m_2 - m_1}{\sqrt{3}} \right) = \frac{2\pi}{L} \left(\frac{n_1}{3}, \frac{n_2}{\sqrt{3}} \right)$$

where n_1 and n_2 are integers of same parity. In general, we can assume that the wavefunctions of the octahedron are real since the Hamiltonian is real. Thus we can take a to be real and simply take the real and imaginary parts of $\psi(\vec{x})$ to obtain explicit expressions for the wavefunctions as follows:

$$\begin{aligned} \psi_{n_1, n_2}^{(c)}(\vec{x}) &= A_{n_1, n_2} \left[\cos \left[\frac{2\pi}{L} \left(\frac{n_1}{3}x_1 + \frac{n_2}{\sqrt{3}}x_2 \right) \right] + \cos \left[\frac{\pi}{L} \left(-\left(\frac{n_1}{3} + n_2 \right)x_1 + \sqrt{3} \left(\frac{n_1 - n_2}{3} \right)x_2 \right) \right] \right. \\ &\quad \left. + \cos \left[\frac{\pi}{L} \left(-\left(n_2 - \frac{n_1}{3} \right)x_1 + \sqrt{3} \left(\frac{n_1 + n_2}{3} \right)x_2 \right) \right] \right] \end{aligned}$$

and after replacing cosines with sines we obtain additional wavefunctions

$$\begin{aligned} \psi_{n_1, n_2}^{(s)}(\vec{x}) &= A_{n_1, n_2} \left[\sin \left[\frac{2\pi}{L} \left(\frac{n_1}{3}x_1 + \frac{n_2}{\sqrt{3}}x_2 \right) \right] + \sin \left[\frac{\pi}{L} \left(-\left(\frac{n_1}{3} + n_2 \right)x_1 + \sqrt{3} \left(\frac{n_1 - n_2}{3} \right)x_2 \right) \right] \right. \\ &\quad \left. + \sin \left[\frac{\pi}{L} \left(-\left(n_2 - \frac{n_1}{3} \right)x_1 + \sqrt{3} \left(\frac{n_1 + n_2}{3} \right)x_2 \right) \right] \right]. \end{aligned}$$

Lastly, since $\psi(\vec{x})$ is invariant under rotations by $\frac{2\pi}{3}$ about the vertex at $(0, L)$ and under rotations by $\frac{2\pi}{3}$ about the origin, then $\psi(\vec{x})$ is also invariant under rotations by $\frac{2\pi}{3}$ about the vertex at $(-\frac{1}{2}L, \frac{\sqrt{3}}{2}L)$. Via an analogous argument as in the cube case, the wavefunctions are thus invariant under rotations about any vertex \vec{v} . It is then immediate that the edges 4 are identified in Fig. (13). From inspection, edges

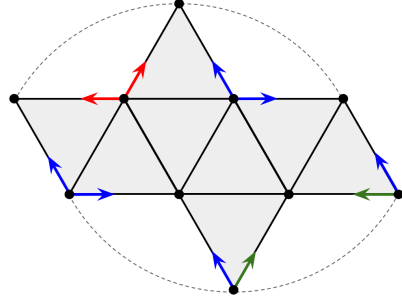


Figure 13: The net of an unfolded octahedron. Vertices that are identified after folding are joined by dashed lines. Arrows of the same color indicate edges that are identified.

that are glued together after folding are correctly identified so all of the necessary boundary conditions are satisfied. Next, as usual, the wavenumber of the wavefunctions is

$$k^2 = \frac{4\pi^2}{3L^2} \left(\frac{n_1^2}{3} + n_2^2 \right)$$

which indicates that degeneracies can occur between wavefunctions ψ_{n_1, n_2} , $\psi_{n_1, -n_2}$, ψ_{-n_1, n_2} and $\psi_{-n_1, -n_2}$. From inspection we note that the wavefunctions ψ_{n_1, n_2} and $\psi_{-n_1, -n_2}$ are equivalent, and thus, in general there is a two-fold degeneracy of $\psi_{n_1, n_2}(\vec{x})$ with $\psi_{n_1, -n_2}(\vec{x})$ or $\psi_{-n_1, n_2}(\vec{x})$ except in cases where one of n_1 or n_2 is zero. This degeneracy reflects the symmetry of the wavefunction about the line $x_2 = \sqrt{3}x_1$.

Lastly, there is an additional two-fold degeneracy between $\psi_{n_1, n_2}^{(c)}$ and $\psi_{n_1, n_2}^{(s)}$. Several examples of degenerate modes are illustrated in Figs. (14), (15), and (16), and various superpositions of degenerate modes are illustrated in Fig. (17).

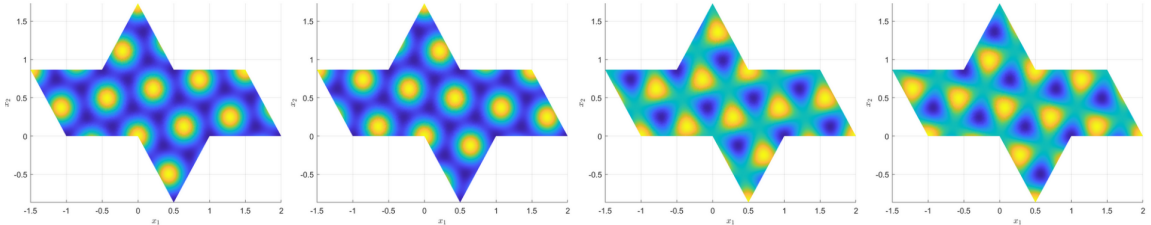


Figure 14: A four-degenerate energy level of octahedron wavefunctions. From left to right: degenerate cosine modes $\psi_{4,2}^{(c)}$ and $\psi_{4,-2}^{(c)}$ and degenerate sine modes $\psi_{4,2}^{(s)}$ and $\psi_{4,-2}^{(s)}$

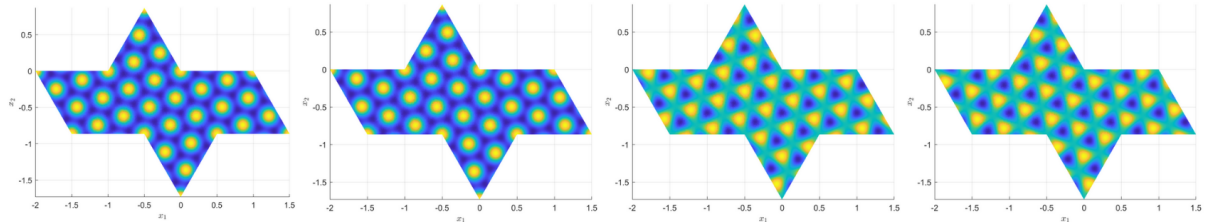


Figure 15: A four-degenerate energy level of octahedron wavefunctions. From left to right: degenerate cosine modes $\psi_{6,4}^{(c)}$ and $\psi_{6,-4}^{(c)}$ and degenerate sine modes $\psi_{6,4}^{(s)}$ and $\psi_{6,-4}^{(s)}$

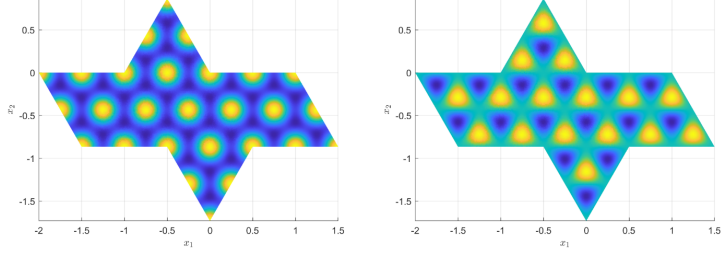


Figure 16: A two-degenerate energy level of octahedron wavefunctions. From left to right: degenerate cosine mode $\psi_{0,4}^{(c)}$ and degenerate sine mode $\psi_{0,4}^{(s)}$

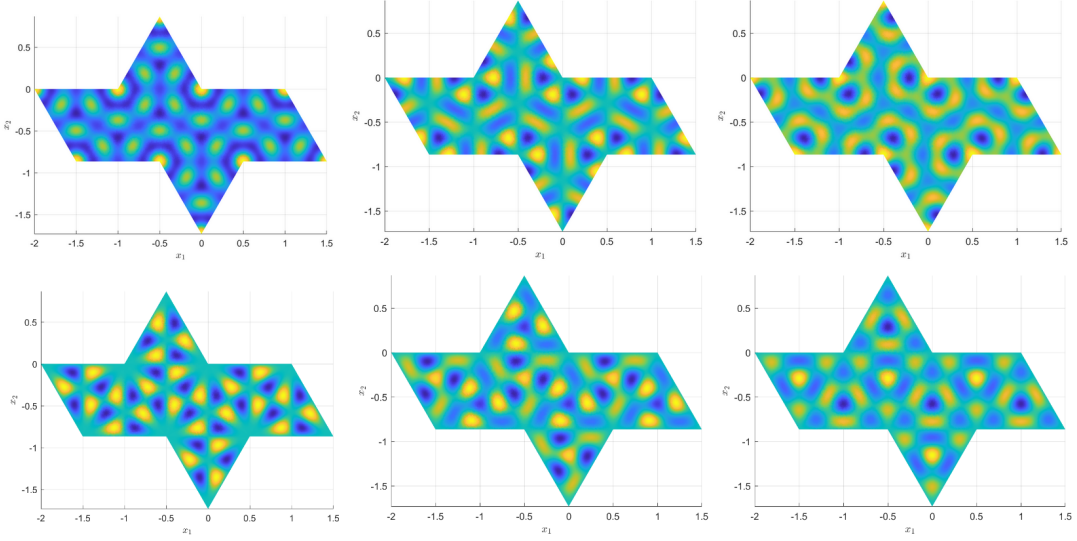


Figure 17: Top row from left to right: symmetric superposition of degenerate cosine modes $\psi_{6,4}^{(c)} + \psi_{6,-4}^{(c)}$, symmetric superposition of degenerate sine modes $\psi_{6,4}^{(s)} + \psi_{6,-4}^{(s)}$, and symmetric superposition of all degenerate modes $\psi_{6,4}^{(c)} + \psi_{6,-4}^{(c)} + \psi_{6,4}^{(s)} + \psi_{6,-4}^{(s)}$. Bottom row from left to right: anti-symmetric superposition of degenerate cosine modes $\psi_{6,4}^{(c)} - \psi_{6,-4}^{(c)}$, anti-symmetric superposition of degenerate sine modes $\psi_{6,4}^{(s)} - \psi_{6,-4}^{(s)}$, and anti-symmetric superposition of all degenerate modes $\psi_{6,4}^{(c)} - \psi_{6,-4}^{(c)} + \psi_{6,4}^{(s)} - \psi_{6,-4}^{(s)}$

2.5 Icosahedron

The icosahedron has conical singularity $\theta = \frac{\pi}{3}$. The vanishing derivative condition at the origin together with the icosahedron boundary conditions requires that $a_0 = a_1 = a_2 = a_3 = a_4 = a_5$. Thus, we can write the ansatz as

$$\psi(\vec{x}) = A[\cos(\vec{k} \cdot \vec{x}) + \cos(C_{\pi/3}\vec{k} \cdot \vec{x}) + \cos(C_{\pi/3}^2\vec{k} \cdot \vec{x})].$$

The vanishing derivative condition at a vertex \vec{v} then requires that $\tilde{a}_{0,\vec{v}} + \tilde{a}_{1,\vec{v}} = \tilde{a}_{3,\vec{v}} + \tilde{a}_{4,\vec{v}}$, so

$$\begin{aligned} e^{i\vec{k} \cdot \vec{v}} + e^{iC_{\pi/3}\vec{k} \cdot \vec{v}} &= e^{iC_{\pi/3}^3\vec{k} \cdot \vec{v}} + e^{iC_{\pi/3}^4\vec{k} \cdot \vec{v}} \\ &= e^{-i\vec{k} \cdot \vec{v}} + e^{-iC_{\pi/3}\vec{k} \cdot \vec{v}}. \end{aligned}$$

It follows that $e^{i\vec{k} \cdot \vec{v}} + e^{iC_{\pi/3}\vec{k} \cdot \vec{v}}$ is real, so its imaginary part must vanish i.e. $\sin(\vec{k} \cdot \vec{v}) + \sin(C_{\pi/3}\vec{k} \cdot \vec{v}) = 0$. Similarly, since $\tilde{a}_{6,\vec{v}} + \tilde{a}_{0,\vec{v}} = \tilde{a}_{2,\vec{v}} + \tilde{a}_{3,\vec{v}}$ then $\sin(C_{\pi/2}^{-1}\vec{k} \cdot \vec{v}) + \sin(\vec{k} \cdot \vec{v}) = 0$. This gives the system of

equations

$$\begin{cases} (C_{\pi/3}\vec{k} - \vec{k}) \cdot \vec{v} = \pi m_1 \\ (C_{\pi/3}^{-1}\vec{k} - \vec{k}) \cdot \vec{v} = \pi m_2 \end{cases}$$

for some integers m_1, m_2 which must be odd. For convenience, we can use $\vec{v} = (L, 0)$, so the system becomes

$$\begin{cases} -\frac{1}{2}k_1 - \frac{\sqrt{3}}{2}k_2 = \frac{\pi}{L}m_1 \\ -\frac{1}{2}k_1 + \frac{\sqrt{3}}{2}k_2 = \frac{\pi}{L}m_2 \end{cases}$$

which gives the solution

$$\vec{k} = \frac{\pi}{L} \left(-(m_1 + m_2), \frac{m_2 - m_1}{\sqrt{3}} \right) = \frac{2\pi}{L} \left(n_1, \frac{n_2}{\sqrt{3}} \right).$$

where n_1 and n_2 are arbitrary integers since $m_1 + m_2$ and $m_2 - m_1$ must be even. Then we obtain the explicit wavefunctions

$$\begin{aligned} \psi_{n_1, n_2}(\vec{x}) = A_{n_1, n_2} & \left[\cos \left[\frac{2\pi}{L} \left(n_1 x_1 + \frac{n_2}{\sqrt{3}} x_2 \right) \right] + \cos \left[\frac{\pi}{L} \left(-(n_1 + n_2)x_1 + \sqrt{3} \left(n_1 - \frac{n_2}{3} \right) x_2 \right) \right] \right. \\ & \left. + \cos \left[\frac{\pi}{L} \left(-(n_2 - n_1)x_1 + \sqrt{3} \left(n_1 + \frac{n_2}{3} \right) x_2 \right) \right] \right]. \end{aligned}$$

Note however, that the boundary condition of the icosahedron net requires that $\psi(3L, 0) = \psi(-2L, 0)$. Evaluating the condition gives

$$\cos(6\pi n_1) + \cos(3\pi(n_1 + n_2)) + \cos(3\pi(n_2 - n_1)) = \cos(4\pi n_1) + \cos(2\pi(n_2 - n_1)) + \cos(2\pi(n_2 - n_1))$$

from which it is clear that n_1 and n_2 must have same parity. Thus, we note that the icosahedron wavefunctions are actually identical to the cosine octahedron wavefunctions when n_1 in the octahedron wavefunction is a multiple of 3. Lastly, we note that the icosahedron wavefunction are invariant under the transformations $(x_1, x_2) \mapsto (x_1 + L, x_2)$ and $(x_1, x_2) \mapsto (x_1 + \frac{L}{2}, x_2 + \frac{\sqrt{3}}{2}L)$. Thus, since the wavefunctions are invariant under rotations by $\frac{\pi}{3}$ about the origin, then they are also invariant under rotations by $\frac{\pi}{3}$ about any vertex \vec{v} . Thus, the edges of the icosahedron net are identified as needed to satisfy all boundary conditions as shown in Fig. (18).

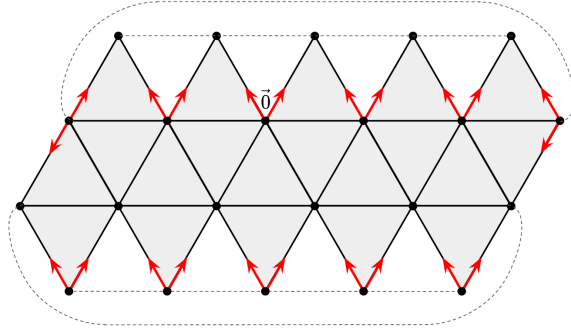


Figure 18: A net of the icosahedron. Identified edges are indicated in red. Vertices that are joined after folding are connected by dashed lines.

Next we note that the icosahedron has energy spectrum given by

$$k^2 = \frac{4\pi^2}{3L^2}(3n_1^2 + n_2^2).$$

Again, from inspection of the wavefunctions, we note that ψ_{n_1, n_2} and $\psi_{-n_1, -n_2}$ are equivalent, and thus, there is a two-fold degeneracy of $\psi_{n_1, n_2}(\vec{x})$ with $\psi_{n_1, -n_2}(\vec{x})$ or $\psi_{-n_1, n_2}(\vec{x})$ except in cases where one of n_1 or n_2 is zero, and this degeneracy reflects the symmetry of the wavefunction about the line $x_2 = \sqrt{3}x_1$. Several examples of icosahedron wavefunctions are plotted in Figs. (19) and (20).

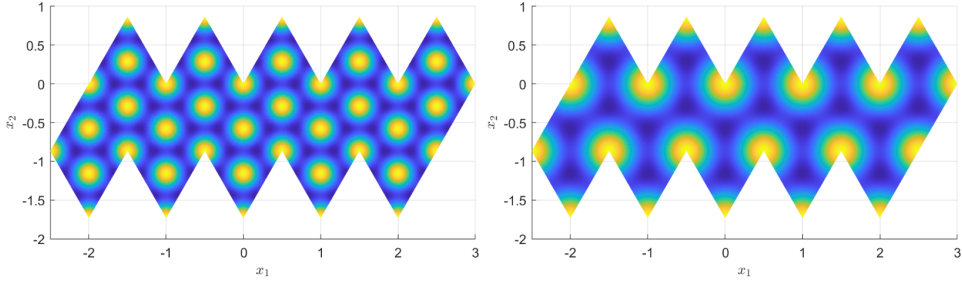


Figure 19: Non-degenerate wavefunctions $\psi_{2,0}$ (left) and $\psi_{0,2}$ (right)

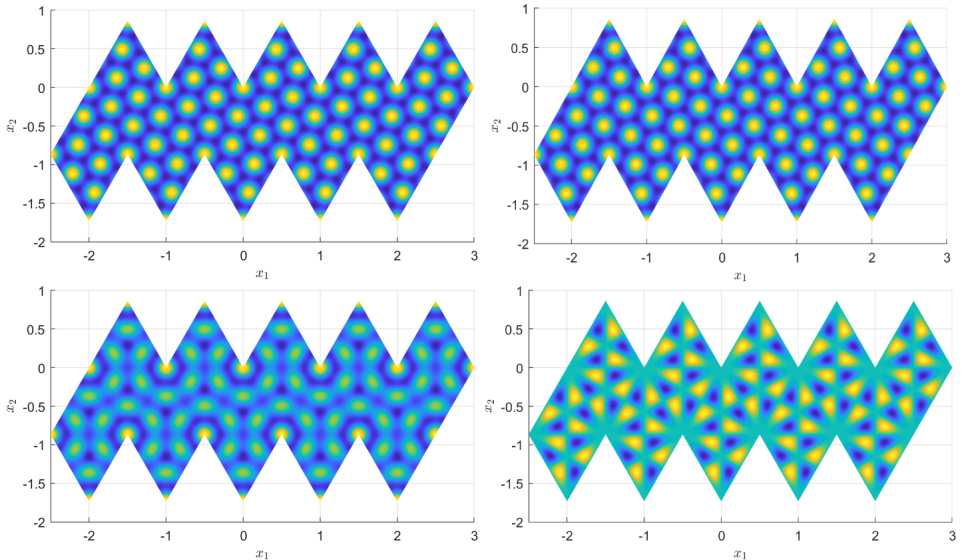


Figure 20: Top row: degenerate wavefunctions $\psi_{2,4}$ (left) and $\psi_{2,-4}$ (right). Bottom row: symmetric superposition $\psi_{2,4} + \psi_{2,-4}$ (left) and anti-symmetric superposition $\psi_{2,4} - \psi_{2,-4}$ (right).

2.6 Square prism

The ratio of the unequal side lengths of the square prism can either be rational or irrational. In this section we consider each case separately.

2.6.1 Rational square prism

The square prism side length ratios will be denoted $L_1 = l_1 L$ and $L_2 = l_2 L$ where $L_1 \times L_1$ is the dimension of the square faces, $L_1 \neq L_2$, and L is a length scaling factor. Since L_1/L_2 is rational then we may assume that l_1 and l_2 are positive, relatively prime integers.

The square prism has conical singularity $\theta = \frac{\pi}{2}$ so we may use the cube wavefunction ansatz. Recall

that a necessary requirement for vanishing derivative at a vertex \vec{v} is that

$$\begin{cases} \vec{k} \cdot \vec{v} = n_1\pi \\ C_{\pi/2}\vec{k} \cdot \vec{v} = n_2\pi. \end{cases}$$

Notice that if the vanishing derivative condition is satisfied at some set of vertices $\{\vec{v}_i\}$, then it is satisfied at all linear combinations of $\{\vec{v}_i\}$ with integer coefficients.

Working with the net shown in Fig. (21), we note that the vanishing derivative condition must be satisfied at the vertices located at $L_1\hat{x}_1$, $L_1\hat{x}_2$, $-L_2\hat{x}_1$, and $-L_2\hat{x}_2$. Thus, the vanishing derivative condition is satisfied at all vertices $X_1\hat{x}_1 + X_2\hat{x}_2$ where X_1 and X_2 are linear combinations of L_1 and L_2 with integer coefficients.

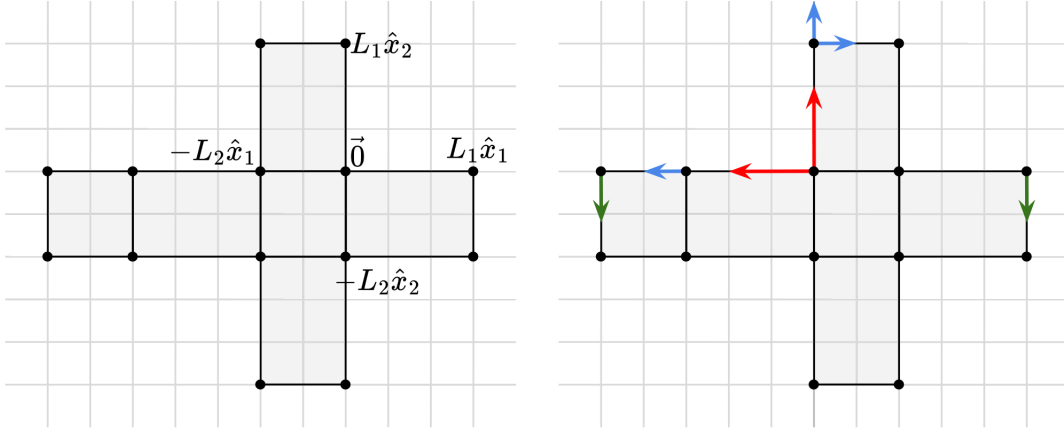


Figure 21: The net of a rational square prism with $l_1 = 2$ and $l_2 = 3$. Grid lines have spacing L . Identified edges are shown by colored arrows.

Next, since l_1 and l_2 are relatively prime then there exists integers u and v such that $l_1u + l_2v = 1^1$. Thus, the vanishing derivative condition is satisfied at $L\hat{x}_1$ and $L\hat{x}_2$, so the wavefunction satisfies the condition on the lattice with basis vectors $L\hat{x}_1$ and $L\hat{x}_2$. Thus, we can simply use the cube wavefunction for a cube of side length L and consider any necessary restrictions on the integers n_1 and n_2 arising from the square prism boundary conditions.

We note that the condition that $\psi(\alpha, -L_1) = \psi(0, -L - \alpha)$ for $\alpha \in [0, L_2]$ simplifies to $(-1)^{n_1 l_1} = (-1)^{n_2 l_1}$, and the condition that $\psi(-\alpha, L_2) = \psi(-2L_1 - L_2 + \alpha, 0)$ for $\alpha \in [0, L_1]$ simplifies to $(-1)^{n_1 l_2} = (-1)^{n_2 l_2}$. Since at least one of l_1 and l_2 must be odd then n_1 and n_2 must have same parity.

Lastly, we demonstrate that these restrictions suffice to satisfy all boundary conditions. Most of the necessary edge identifications follow from one or two applications of invariance of the cube wavefunctions about vertices of the net (e.g. red and blue in Fig. (21)). The remaining edges along the lines $x_1 = -(2L_1 + L_2)$ and $x_1 = L_2$ (shown in green in Fig. (21)) are identified by noting that the wavefunction ansatz is invariant under transformations $x_1 \rightarrow x_1 + 2L$. Thus, the square prism wavefunctions are exactly the same as the cube wavefunctions for a cube with side length L .

2.6.2 Irrational square prism

Now, denote the side lengths of the square prism as \tilde{L}_1 and $\tilde{L}_2 = l\tilde{L}_1$ where $\tilde{L}_1 \times \tilde{L}_1$ is the dimension of the square faces, and l is irrational. Similarly to before, the vanishing derivative condition must be

¹The Euclidean algorithm can be applied to find integers u and v such that $l_1u + l_2v = \gcd(l_1, l_2)$

satisfied at the four vertices $\tilde{L}_1\hat{x}_1, \tilde{L}_1\hat{x}_2, -\tilde{L}_2\hat{x}_1$ and $-\tilde{L}_2\hat{x}_2$. Employing the cube wavefunction ansatz, the wavefunction satisfies the vanishing derivative condition at all vertices $\tilde{X}_1\hat{x}_1 + \tilde{X}_2\hat{x}_2$ where \tilde{X}_1 and \tilde{X}_2 are linear combinations of \tilde{L}_1 and \tilde{L}_2 with integer coefficients.

However, since l is irrational then the set $\{u\tilde{L}_1 + v\tilde{L}_2 \mid u, v \in \mathbb{Z}\}$ is dense in \mathbb{R}^2 . Further we note that if the vanishing derivative condition is satisfied at \vec{x} then the derivative must vanish at $2\vec{x}$. As a result, the partial derivatives $\partial_1\psi$ and $\partial_2\psi$ of the wavefunction must vanish on a dense subset of \mathbb{R}^2 . Then, since $\partial_i\psi : \mathbb{R}^2 \rightarrow \mathbb{R}$ is a continuous mapping to a Hausdorff space that vanishes on a dense subset of \mathbb{R}^2 then $\partial_i\psi$ must vanish everywhere for $i = 1, 2$.³ Thus, $\nabla\psi = \vec{0}$, so ψ is a constant. Therefore, there are no non-trivial wavefunctions on the irrational square prism in the form of the cube wavefunction ansatz.

2.7 Rectangular prism

The ratio of the unequal side lengths of the rectangular prism can either be all rational or contains at least one irrational ratio. We consider each case separately.

2.7.1 Rational rectangular prism

The square prism side length ratios will be denoted $L_1 = l_1L$, $L_2 = l_2L$, and $L_3 = l_3L$ where L is a length scaling factor and $L_1 \neq L_2 \neq L_3$. Since $\frac{L_1}{L_2}$ and $\frac{L_2}{L_3}$ are rational then assume that l_1, l_2 , and l_3 are positive integers with no common divisors.

Since the rectangular prism has conical singularity $\theta = \frac{\pi}{2}$ we again use the cube wavefunction ansatz. The wavefunction ansatz must satisfy the vanishing derivative condition at vertices $L_1\hat{x}_1, L_2\hat{x}_2$, and $-L_3\hat{x}_1$. By rotational invariance of the solvable wavefunctions under rotations by $\frac{\pi}{2}$ about the origin, the extremal value condition is also satisfied at vertices $L_1\hat{x}_2, -L_2\hat{x}_1$, and $-L_3\hat{x}_2$. Thus the wavefunction satisfies the extremal value condition at all vertices $X_1\hat{x}_1 + X_2\hat{x}_2$ where X_1 and X_2 are linear combinations of L_1, L_2 , and L_3 with integer coefficients.

Since $\gcd(l_1, l_2, l_3) = 1$ then there exists integers u, v , and w such that $ul_1 + vl_2 + wl_3 = 1$.⁴ A similar application of boundary conditions such as $\psi(\alpha, -L_2) = \psi(0, L_2 - \alpha)$ for $\alpha \in [0, L_3]$ and $\psi(-\alpha, L_3) = \psi(-2L_1 - L_3 + \alpha, 0)$ for $\alpha \in [0, L_1]$ again forces n_1 and n_2 to have same parity. Thus, the

²To prove this statement, it suffices to show that $uL_1 + vL_2$ where $\frac{L_1}{L_2}$ is irrational and u and v are any integers can be made arbitrarily small. By rescaling we can further assume that $L_2 = 1$ and L_1 is irrational. Then by expanding L_1 as a decimal, we can write $L_1 = \sum_{j=-M}^{\infty} \frac{c_j}{10^j}$ for some fixed and bounded positive integer M and some integers c_j . Then for an arbitrary large positive integer M' we have

$$L_1 = \sum_{j=-M}^{M'} \frac{c_j}{10^j} + \mathcal{O}(10^{-M'-1}) \quad (9)$$

where $\mathcal{O}(10^{-M'-1})$ is a bounded error term satisfying $|\mathcal{O}(10^{-M'-1})| < 10^{-M'}$. Multiplying both sides of Eqn. (9) by 10^M then gives

$$10^M L_1 = \sum_{j=-M}^{M'} c_j 10^{M'-j} + \mathcal{O}(10^{-M'-1}),$$

so setting $u = 10^M$ and $v = -\sum_{j=-M}^{M'} c_j 10^{M'-j}$ ensures that $|uL_1 + vL_2| < 10^{-M'}$, as desired.

³Suppose to the contrary that ψ is non-constant and $\psi = c$ on a dense subset of \mathbb{R}^2 for some constant $c \in \mathbb{R}$. Then choose some $\vec{x} \in \mathbb{R}^2$ such that $\psi(\vec{x}) = c' \neq c$. Since \mathbb{R} is Hausdorff we can choose an open interval $I \subset \mathbb{R}$ such that $c' \in I$ and $c \notin I$. Since ψ is continuous then the inverse image $\psi^{-1}(I)$ is an open, non-empty subset of \mathbb{R}^2 . Since $\psi = c$ on a dense subset of \mathbb{R}^2 then there must exist some point $\vec{y} \in \psi^{-1}(I)$ such that $\psi(\vec{y}) = c$, a contradiction, since $\psi(\vec{y}) = c \notin I$.

⁴The Euclidean algorithm can be used to find integers u and v such that $u'l_1 + v'l_2 = \gcd(l_1, l_2)$. The algorithm can again be used to find integers w and w' such that $w'\gcd(l_1, l_2) + wl_3 = \gcd(\gcd(l_1, l_2), l_3) = \gcd(l_1, l_2, l_3)$. Then setting $u = w'u'$ and $v = w'v'$ gives $ul_1 + vl_2 + wl_3 = 1$, as desired.

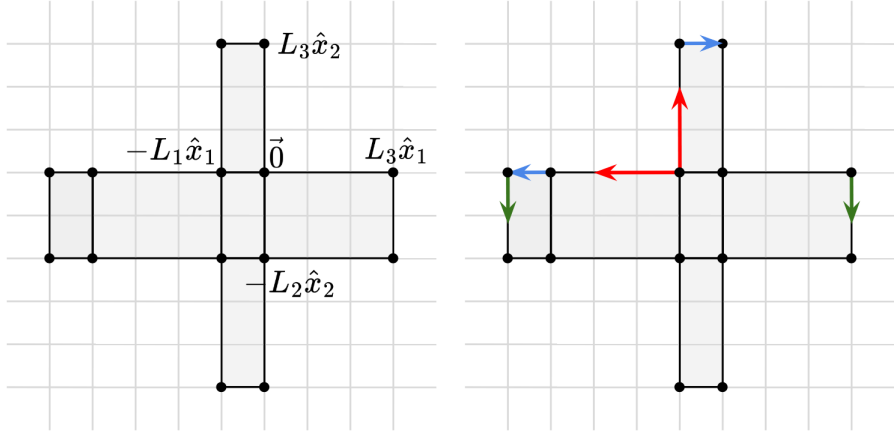


Figure 22: The net of a rational rectangular prism with $l_1 = 1$, $l_2 = 2$, and $l_3 = 3$. Grid lines have spacing L . Identified edges are shown by colored arrows on the right.

wavefunctions of the rectangular prism are identical to the wavefunctions on a cube with side length L , and all the necessary edges are identified to allow folding of the rectangular prism net.

2.7.2 Irrational rectangular prism

If the rectangular prism has at least one side length ratio which is irrational we again find that no non-trivial wavefunctions exist on the net. More explicitly, by relabeling edges or rotating axes as necessary we can assume that $\frac{L_i}{L_j}$ is irrational and the vanishing derivative condition is satisfied at the vertices $L_i\hat{x}_1$ and $L_j\hat{x}_2$. After substituting $L_i \rightarrow \tilde{L}_1$ and $L_j \rightarrow \tilde{L}_2$, the remainder of the proof is identical to the square prism case.

3 Unsolvable wavefunctions on the cube

In this section, we will analyze the cube wavefunctions in greater detail. First, we will demonstrate that the solvable cube wavefunctions found in Section 2.3 are incomplete, and then we will use a computational approach to understand the remaining cube wavefunctions. We conjecture that the remaining wavefunctions are unsolvable and quantum chaotic [7–9] and support this conjecture using evidence from the structure of the energy level spacings of the cube wavefunctions.

3.1 Incompleteness of solvable eigenmodes

We provide three proofs that the previously-computed solvable wavefunctions on a cube are incomplete. The proofs will use a direct computation of the completeness relation, a symmetry-based argument, and thermodynamics-based argument, respectively. The thermodynamics-based proof will additionally show that the solvable wavefunctions comprise $\frac{1}{12}$ of the complete set of cube wavefunctions.

3.1.1 Proof of incompleteness by direct computation

We define the inner product of the wave functions as

$$(\psi, \phi) = \int_{\Omega} d\vec{x} \psi^*(\vec{x}) \phi(\vec{x})$$

where $\Omega \subset \mathbb{R}^2$ indicates the area of the unfolded cube. It is then straightforward to calculate the normalization constants of the modes:

$$A_{n_1, n_2} = A_{m, n} = \begin{cases} \frac{A}{2} & (n_1, n_2) = (m, n) = \vec{0} \\ A & \text{otherwise.} \end{cases}$$

where $A := \frac{2}{L\sqrt{6}}$. To demonstrate that the modes are complete, we will attempt to show the completeness relation

$$\int_{\Omega} d\vec{x} \left(\sum_{\text{unique modes}} \psi(\vec{x}) \psi(\vec{x}) \right) = 1.$$

To do so, we will first evaluate the summation

$$\Psi(\vec{x}, \vec{x}') = \sum_{(m, n) \in \mathcal{D}} \psi_{m, n}(\vec{x}) \psi_{m, n}(\vec{x}')$$

where $\mathcal{D} = \{(m, n) \in \mathbb{Z}^2 \mid m > |n|, m > 0\} \cup \{(m, n) \in \mathbb{Z}^2 \mid m = -n \geq 0\}$ is an index set chosen so that each unique wavefunction is counted exactly once while the ground state is counted exactly once (see Figure 23). For future calculations, it will be more convenient to index the wavefunctions by the (n_1, n_2) indices. To convert the index set \mathcal{D} for indices (m, n) to the corresponding index set \mathcal{D}' for indices (n_1, n_2) we note that

$$\begin{bmatrix} n_1 \\ n_2 \end{bmatrix} = \begin{bmatrix} 1 & -1 \\ 1 & 1 \end{bmatrix} \begin{bmatrix} m \\ n \end{bmatrix} = \sqrt{2} \begin{bmatrix} \cos \frac{\pi}{4} & -\sin \frac{\pi}{4} \\ \sin \frac{\pi}{4} & \cos \frac{\pi}{4} \end{bmatrix} \begin{bmatrix} m \\ n \end{bmatrix}$$

so \mathcal{D}' can be obtained from \mathcal{D} by a counterclockwise rotation by $\frac{\pi}{4}$ about the origin and scaling by $\sqrt{2}$ (see Figure 23). Note that \mathcal{D}' misses all points (n_1, n_2) where n_1 and n_2 have differing parity, as expected. However, in future calculations it will be convenient to sum over the "filled-in" set $\mathcal{D}'' = \{(n_1, n_2) \in$

$\mathbb{Z}^2 \setminus \{(n_1, n_2) \mid n_1 > 0, n_2 > 0\} \cup \{(n_1, 0) \mid n_1 \geq 0\}$ instead of \mathcal{D}' (see Figure 23), and simultaneously introduce a factor of $\cos^2(\frac{\pi}{2}(n_1 + n_2))$ in the summand to eliminate terms where n_1 and n_2 have differing parity.

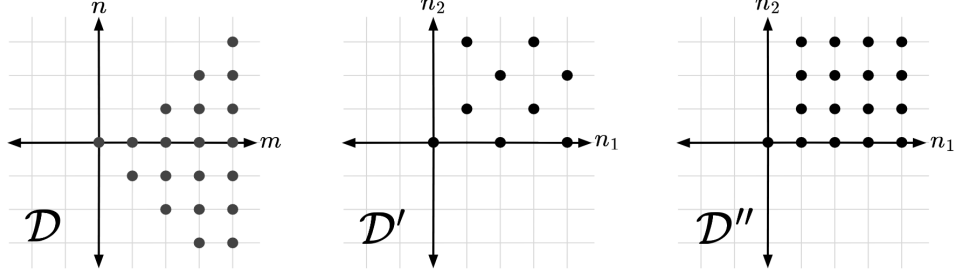


Figure 23: Illustration of the index sets \mathcal{D} , \mathcal{D}' , and \mathcal{D}'' given in Eq. 6.

As a result, we may write

$$\begin{aligned}\Psi(\vec{x}, \vec{x}') &= \sum_{(n_1, n_2) \in \mathcal{D}''} \psi_{n_1, n_2}(\vec{x}) \psi_{n_1, n_2}(\vec{x}') \cos^2\left(\frac{\pi}{2}(n_1 + n_2)\right) \\ &= \sum_{(n_1, n_2) \in \mathcal{D}'} \frac{A_{n_1, n_2}^2}{2} \left[\cos\left(\frac{\pi}{L}(n_1 x_1 + n_2 x_2)\right) + \cos\left(\frac{\pi}{L}(n_1 x_2 - n_2 x_1)\right) \right] \\ &\quad \times \left[\cos\left(\frac{\pi}{L}(n_1 x'_1 + n_2 x'_2)\right) + \cos\left(\frac{\pi}{L}(n_1 x'_2 - n_2 x'_1)\right) \right] \times \cos^2\left(\frac{\pi}{2}(n_1 + n_2)\right)\end{aligned}$$

where we have simply plugged in the expression for the modes from Eq. 5. By multiplying out each summand and using the two identities $2 \cos(x) \cos(y) = \cos(x+y) + \cos(x-y)$ and $\cos(x+N\pi) = \cos(x-N\pi)$ where $N \in \mathbb{Z}$ the expression expands into

$$\begin{aligned}\Psi(\vec{x}, \vec{x}') &= \sum_{(n_1, n_2) \in \mathcal{D}''} \sum_{j=0}^1 \frac{A_{n_1, n_2}^2}{4} \left[\cos\left(\frac{\pi}{L}(n_1(x_1 \pm x'_1 + jL) + n_2(x_2 \pm x'_2 + jL))\right) \right. \\ &\quad + \cos\left(\frac{\pi}{L}(n_1(x_2 \pm x'_1 + jL) - n_2(x_1 \mp x'_2 + jL))\right) \\ &\quad + \cos\left(\frac{\pi}{L}(n_1(x_1 \pm x'_2 + jL) + n_2(x_2 \mp x'_1 + jL))\right) \\ &\quad \left. + \cos\left(\frac{\pi}{L}(n_1(x_2 \pm x'_2 + jL) - n_2(x_1 \pm x'_1 + jL))\right) \right]\end{aligned}$$

where each cosine term is counted twice in each term in the series, once with each set of $+$ and $-$ signs. This gives a total of sixteen terms in the series for each pair of indices $(n_1, n_2) \in \mathbb{C}$. Then using the

identity $\cos(x) = \frac{1}{2}(e^{ix} + e^{-ix})$, pairs of the cosine terms in the series can be rewritten as

$$\begin{aligned}
& \sum_{(n_1, n_2) \in \mathcal{D}''} \frac{A_{n_1, n_2}^2}{4} \left[\cos\left(\frac{\pi}{L}(n_1 u + n_2 v)\right) + \cos\left(\frac{\pi}{L}(n_1 v - n_2 u)\right) \right] \\
&= \frac{A_{0,0}^2}{2} + \sum_{(n_1, n_2) \in \mathcal{D}'' - \{\vec{0}\}} \frac{A_{n_1, n_2}^2}{4} \left[\cos\left(\frac{\pi}{L}(n_1, n_2) \cdot (u, v)\right) + \cos\left(\frac{\pi}{L}(-n_2, n_1) \cdot (u, v)\right) \right] \\
&= \frac{A^2}{8} \left\{ 1 + \sum_{(n_1, n_2) \in \mathcal{D}'' - \{\vec{0}\}} \left(\exp\left[i\frac{\pi}{L}(n_1, n_2) \cdot (u, v)\right] + \sum_{(n_1, n_2) \in \mathcal{D}'' - \{\vec{0}\}} \exp\left[i\frac{\pi}{L}(-n_1, -n_2) \cdot (u, v)\right] \right. \right. \\
&\quad \left. \left. + \sum_{(n_1, n_2) \in \mathcal{D}'' - \{\vec{0}\}} \exp\left[i\frac{\pi}{L}(-n_2, n_1) \cdot (u, v)\right] + \sum_{(n_1, n_2) \in \mathcal{D}'' - \{\vec{0}\}} \exp\left[i\frac{\pi}{L}(n_2, -n_1) \cdot (u, v)\right] \right) \right\} \\
&= \frac{A^2}{8} \left\{ 1 + \sum_{j=0}^3 \sum_{(n_1, n_2) \in \mathcal{D}'' - \{\vec{0}\}} \exp\left[i\frac{\pi}{L}C_{\pi/4}^j(n_1, n_2) \cdot (u, v)\right] \right\} \\
&= \frac{A^2}{8} \left\{ 1 + \sum_{j=0}^3 \sum_{(n_1, n_2) \in C_{\pi/4}^j(\mathcal{D}'' - \{\vec{0}\})} \exp\left[i\frac{\pi}{L}(n_1, n_2) \cdot (u, v)\right] \right\} \\
&= \frac{A^2}{8} \sum_{n_1, n_2 = -\infty}^{\infty} \exp\left[i\frac{\pi}{L}(n_1, n_2) \cdot (u, v)\right]
\end{aligned}$$

where in the second to last equality we have inverted the rotations $C_{\pi/4}^j(n_1, n_2) \rightarrow (n_1, n_2)$ and compensated by rotating the index sets $(\mathcal{D} - \{\vec{0}\}) \rightarrow C_{\pi/4}^j(\mathcal{D} - \{\vec{0}\})$ accordingly. Next, using the Fourier series of a Dirac comb

$$\sum_{M=-\infty}^{\infty} \exp\left[i\frac{2\pi}{a}Mx\right] = a \sum_{M=\infty}^{\infty} \delta(x - aM)$$

with $a = 2L$ and $(M, x) = (n_1, u)$ or (n_2, v) gives

$$\frac{A^2}{8} \sum_{n_1, n_2 = -\infty}^{\infty} \exp\left[i\frac{\pi}{L}(n_1 u + n_2 v)\right] = \frac{1}{3} \sum_{n_1, n_2 = -\infty}^{\infty} \delta(u + 2n_1 L) \delta(v + 2n_2 L).$$

Thus, $\Psi(\vec{x}, \vec{x}')$ is in fact a two-dimensional Dirac comb:

$$\begin{aligned}
\Psi(\vec{x}, \vec{x}') &= \frac{1}{3} \sum_{n_1, n_2 = -\infty}^{\infty} \sum_{j=0}^1 \left[\delta(x_1 + x'_1 + (2n_1 + j)L) \delta(x_2 + x'_2 + (2n_2 + j)L) \right. \\
&\quad + \delta(x_1 - x'_1 + (2n_1 + j)L) \delta(x_2 - x'_2 + (2n_2 + j)L) \\
&\quad + \delta(x_2 + x'_1 + (2n_1 + j)L) \delta(x_1 - x'_2 + (2n_2 + j)L) \\
&\quad \left. + \delta(x_2 - x'_1 + (2n_1 + j)L) \delta(x_1 + x'_2 + (2n_2 + j)L) \right]. \tag{10}
\end{aligned}$$

This Dirac comb plots two delta functions in each face of the unfolded cube, each with a magnitude of $\frac{1}{3}$ (see Fig. (24)). Thus, it is clear that $\Psi(\vec{x}, \vec{x}') \neq \delta(\vec{x} - \vec{x}')$ within the domain of the unfolded cube. Furthermore, the presence of twelve delta functions in the domain of the unfolded cube instead of one suggests (but does not prove) that we have only found 1/12 of all the eigenmodes.

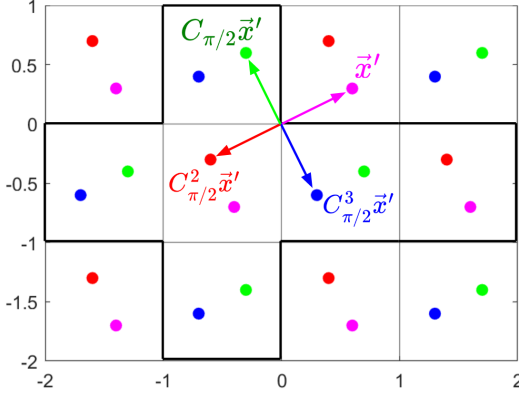


Figure 24: Illustration of Dirac comb given in Eq. 10 in the case where $\vec{x}' = (0.6L, 0.3L)$. Delta functions with magnitude $\frac{1}{3}$ are located at each of the colored plotted points. Points with the same color arise in the same term in the summand of Eq. 10. The domain of the unfolded cube is outlined in black.

3.1.2 Proof of incompleteness via thermodynamics

For simplicity we work with the assumption that $E = k^2$ by ignoring appropriate proportionality constants. Then, a general result of thermodynamics is that the expected number definite-energy wavefunctions below energy E_0 for a particle confined to a volume V is

$$N(E) = \frac{V\pi E_0}{(2\pi)^d} \quad (11)$$

where d is the dimension of the space [10]. In our case, the volume V is an area and $d = 2$. Eq. 11 can readily be demonstrated in the case where V is a rectangle with side lengths L_x and L_y . It follows that the wave vectors can take values $k_x = \frac{2\pi n_x}{L_x}$ and $k_y = \frac{2\pi n_y}{L_y}$ for any $n_x, n_y \in \mathbb{Z}$. Then in k -space each wavefunction occupies an area

$$k_x k_y = \frac{2\pi}{L_x} \frac{2\pi}{L_y} = \frac{(2\pi)^2}{V}. \quad (12)$$

Similarly, the total area occupied by all states in k -shape with energy below is E_0 is a circle of radius $k = \sqrt{E_0}$. Dividing the total area πE_0 by the area occupied by each state (Eq. 12) then gives Eq. 11. Further, this result can be generalized to any shape with volume V .

The area of the unfolded cube is $6L^2$, so below energy E , the expected number of states $N(E)$ and density of states $D(E) = \frac{dN(E)}{dE}$ are

$$N(E) = \frac{3L^2}{2\pi} E \quad \Rightarrow \quad D(E) = \frac{3L^2}{2\pi}. \quad (13)$$

Next, recall from Figure 23 that using n_1 and n_2 indices, each mode occupies an area of 2 in (n_1, n_2) space which corresponds to an area of $\frac{2\pi^2}{L^2}$ in (k_1, k_2) space. Furthermore, the total area occupied by distinct modes in (k_1, k_2) space is only a quarter-circle due to the four-fold symmetry of all modes except the ground state. It follows that

$$N_s(E) = \frac{\pi E}{4} \cdot \frac{L^2}{2\pi^2} = \frac{L^2}{8\pi} E \quad \Rightarrow \quad D_s(E) = \frac{L^2}{8\pi}$$

A comparison to Eq. 13 then shows that $D_s(E) = \frac{1}{12} D(E)$. Thus the solvable modes are incomplete and comprise only $\frac{1}{12}$ of the total number of states.

3.1.3 Proof of incompleteness by symmetry

The Hamiltonian governing a free particle $\mathcal{H} = \frac{\hat{p}^2}{2m}$ is rotationally invariant. It follows that $[\mathcal{H}, C_\theta] = 0$, and since both H and C_θ are Hermitian then \mathcal{H} and C_θ are simultaneously diagonalizable. Then by letting ψ be a simultaneous eigenstate of \mathcal{H} and C_θ we have

$$\mathcal{H}\psi = E\psi \quad \text{and} \quad C_\theta\psi = \lambda_\theta\psi$$

We consider the particular case where $\theta = \frac{\pi}{2}$ which corresponds to the rotational symmetry of the cube about the axes connecting opposite vertices as shown in Fig. (26) by the angle $\frac{2\pi}{3}$. Since $C_{2\pi/3}^3 = 1$ then it is required that

$$\lambda_\theta = e^{i\frac{2\pi n}{3}}$$

for some $n = 0, 1, 2$. Since $C_{\pi/2}\psi(\vec{x}) = \psi(C_{\pi/2}^{-1}\vec{x}) = \psi(\vec{x})$ it follows that all solvable eigenstates of \mathcal{H} are also eigenstates of $C_{\pi/2}$ with eigenvalue 1. However, it is impossible to construct eigenfunctions of $C_{\pi/2}$ with eigenvalues other than 1 using only the solvable eigenfunctions of \mathcal{H} indicating that they are incomplete.

3.2 Cube Symmetries

Future analysis will require substantial use of the symmetries of the cube which will be discussed in detail in this section. We define a symmetry of the cube as an isometric mapping of the cube to itself. The set of all symmetries of the cube form a group isomorphic to $O_h = T_d \times \mathbb{Z}/2\mathbb{Z}$ where T_d is symmetry group of the tetrahedron and $\mathbb{Z}/2\mathbb{Z}$ is the order 2 cyclic group.

The group T_d is isomorphic to the permutation group on four letters since the symmetries of the tetrahedron permute the four vertices of tetrahedron, giving a bijective correspondence between tetrahedron symmetries and permutations on four letters. To obtain the symmetry group of the cube note that the tetrahedron can be inscribed in the cube as shown in Fig. (25). Alternatively, symmetries of the cube can be viewed as permutations of the four diagonals illustrated in Fig. (25).

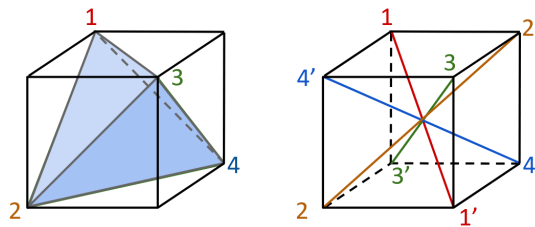


Figure 25: Illustration showing that T_d is isomorphic to the symmetry group S_4 . The symmetries of the cube are also symmetries of a tetrahedron inscribed in the cube or alternatively the four diagonals of the cube.

Thus, the set of tetrahedron symmetries is a subgroup of the set of cube symmetries, all of which are realizable on a physical cube via rotations. The cube has one additional generator in its symmetry group corresponding to the inversion mapping. Inversion can roughly be understood as turning the cube inside out and corresponds to the mapping $\vec{x} \mapsto -\vec{x}$ in \mathbb{R}^3 . Alternatively, inversion can be viewed as swapping the labels on each of the four diagonals in Fig. (25), that is, sending $n \mapsto n'$. Inversion cannot be performed on a physical cube and is a component of symmetries such as reflections. Additionally, all symmetries of the cube can be realized as a tetrahedron symmetry possibly followed by inversion. Lastly, since the inversion symmetry commutes with all symmetries in T_d then the symmetry group of

the cube is isomorphic to $O_h = T_d \times \mathbb{Z}/2\mathbb{Z}$.

Next, we note that each conjugacy class of $T_d \times \mathbb{Z}/2\mathbb{Z}$ corresponds to a specific type of symmetry of the cube. For example, the conjugacy class consisting of 3-cycles of T_d and no inversion corresponds to rotations by $\frac{2\pi}{3}$ about the diagonals of the cube. Each of the eight elements of the conjugacy class corresponds to such a rotation in one of two directions about one of the four diagonals of the cube. The rotation and reflection symmetries of the cube are illustrated in Figs. (26) and (27). Throughout this paper we use Schoenflies symmetry notation [11]:

- E = identity
- i = inversion
- C_n = rotation by $\frac{2\pi}{n}$ about an axis
- $\sigma_d, \sigma_h, \sigma_v$ = reflection through a diagonal, horizontal, or vertical plane, respectively
- S_n = improper rotation, i.e. a rotation by $\frac{2\pi}{n}$ about an axis followed by a σ_h reflection or equivalently, a rotation by $\frac{4\pi}{n}$ about an axis followed by inversion

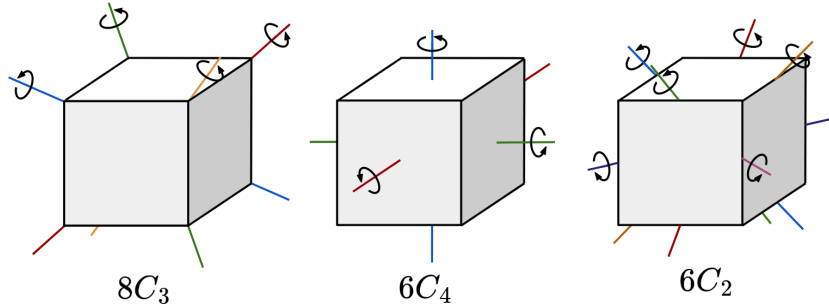


Figure 26: Rotation symmetries of the cube. The symmetries are labeled by the conjugacy class of elements corresponding to each symmetry as well as a representative element.

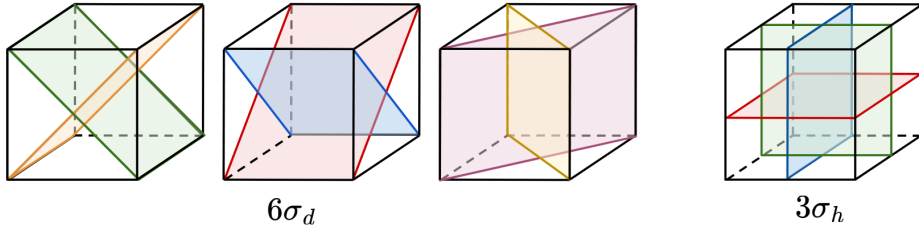


Figure 27: Reflection symmetries of the cube. The symmetries are labeled by the conjugacy class of elements corresponding to each symmetry as well as a representative element.

3.3 Computational approach

All MATLAB code used in this project can be accessed at <https://github.com/kimie-shen/senior-thesis>. We will examine the remaining wavefunctions on a cube by solving a discretized version of the wave equation. That is, we solve the wave equation on a lattice on the net of a cube as illustrated in Fig (28). In our analysis it will also be relevant to examine the tight-binding model, a model commonly used in condensed matter physics to approximate wavefunctions of many-particle systems where particles are located at discrete lattice points.

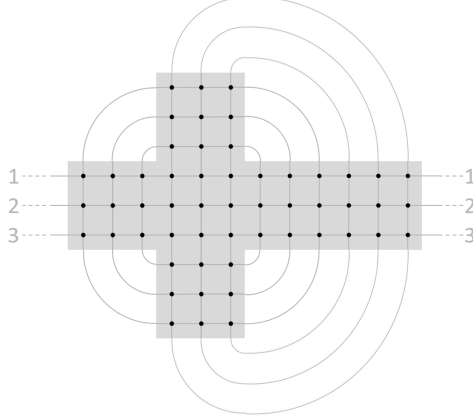


Figure 28: Lattice of points on the cube net with $N = 3$ sites per edge. Each point is joined by gray lines to its four nearest neighbors on the cube after folding.

3.3.1 Tight-binding Hamiltonian

Consider a crystal with a d -dimensional Bravais lattice with primitive basis vectors $\vec{a}_1, \vec{a}_2, \dots, \vec{a}_d$. Then any lattice point may be written as $\vec{R} = \sum_{i=1}^d n_i \vec{a}_i$ where $n_i \in \mathbb{Z}$. For our purposes we only need to consider a single band in the crystal. Thus, let $|\vec{R}\rangle$ denote an electron localized at lattice site \vec{R} , that is, a single-particle Wannier state. Let $c_{\vec{R}}^\dagger$ and $c_{\vec{R}}$ denote the creation and annihilation operators of $|\vec{R}\rangle$. Then, the Hamiltonian can be written in the Wannier basis as

$$H = \sum_{\vec{R}} \sum_{\vec{R}'} c_{\vec{R}}^\dagger \mathcal{H}_{\vec{R}, \vec{R}'} c_{\vec{R}'}, \quad \mathcal{H}_{\vec{R}, \vec{R}'} := \langle \vec{R} | H | \vec{R}' \rangle$$

where $\mathcal{H}_{\vec{R}, \vec{R}'}$ is called the hopping from site \vec{R} to \vec{R}' . Since Hamiltonian and Wannier functions are functions of $\vec{r} - \vec{R}$ it follows that the hopping $\mathcal{H}_{\vec{R}, \vec{R}'}$ only depends on $\vec{r} - \vec{R}$. Moreover, since the Wannier functions are localized near \vec{R} it suffices to consider only nearest neighbor hoppings. So it suffices to fix the values of $\mathcal{H}_{\vec{R}, \vec{R}}$ and $\mathcal{H}_{\vec{R}, \vec{R} + \vec{a}_i}$ to fully determine the tight-binding Hamiltonian.

For our purposes it will be most useful to consider a 2D lattice with primitive vectors $a_0 \hat{x}_1$ and $a_0 \hat{x}_2$ where $a_0 = \frac{L}{N}$ where N is the number of lattice points along each edge of the cube. It will also be helpful to set

$$\mathcal{H}_{\vec{R}, \vec{R}} = -\frac{4}{a_0^2} \quad \text{and} \quad \mathcal{H}_{\vec{R}, \vec{R} \pm a_0 \hat{x}_i} = +\frac{1}{a_0^2}. \quad (14)$$

for $i = 1, 2$. In the case of the cube, it is understood that $\vec{R} \pm a_0 \hat{x}_i$ refers to the four nearest neighbors of the point \vec{R} .

To see why the coefficients in Eqn. (14) are useful, consider a function f defined on a lattice on a cube net with separation a_0 between neighboring lattice points. Then a Taylor expansion to second order in a_0 of the expression $\partial_{x_i} f(\vec{R} + a_0 \hat{x}_i)$ for $i = 1, 2$ can be rearranged to give the approximation

$$\nabla^2 f(\vec{R}) = \frac{1}{a_0^2} (f(\vec{R} + a_0 \hat{x}_1) + f(\vec{R} - a_0 \hat{x}_1) + f(\vec{R} + a_0 \hat{x}_2) + f(\vec{R} - a_0 \hat{x}_2) - 4f(\vec{R})) + \mathcal{O}(a_0).$$

Then, the matrix of the tight-binding Hamiltonian in the Wannier basis becomes identical to the matrix operator that enacts ∇^2 on f in the basis $\{f(\vec{v})\}$ where \vec{v} is any lattice point. Thus, in the limit $a_0 \rightarrow 0$ the spectra of the tight-binding Hamiltonian provides all values of E for which the function $f(\vec{x})$ satisfies the equation $\nabla^2 f(\vec{x}) = -Ef(\vec{x})$.

We now can solve for the energy spectra of the tight-binding Hamiltonian. With the matrix component choices given in Eq. 14 the tight-binding Hamiltonian becomes

$$H = \frac{1}{a_0^2} \left(\sum_{\vec{R}} (c_{\vec{R}+a_0\hat{x}_1}^\dagger c_{\vec{R}} + c_{\vec{R}+a_0\hat{x}_2}^\dagger c_{\vec{R}} + h.c.) - 4 \sum_{\vec{R}} c_{\vec{R}}^\dagger c_{\vec{R}} \right). \quad (15)$$

Next since the Wannier function is defined as the Fourier transform of the single-particle wavefunction then we may write an analogous relation for their creation operators:

$$c_{\vec{R}}^\dagger = \frac{1}{\sqrt{N}} \sum_{\vec{k}} e^{-i\vec{k}\cdot\vec{R}} c_{\vec{k}}^\dagger \quad (16)$$

where $c_{\vec{k}}$ is the creation operator of an eigenstate $\psi_{\vec{k}}$, and \vec{k} is the quasi-momentum wavevector given by $\vec{k} = \frac{2\pi n_1}{a_0} + \frac{2\pi n_2}{a_0}$ for some $n_1, n_2 \in \mathbb{Z}$. Then plugging Eq. 16 into Eq. 15 allows us to diagonalize the Hamiltonian matrix as follows:

$$\begin{aligned} H &= \frac{1}{a_0^2} \sum_{\vec{R}} \sum_{\vec{k}, \vec{k}'} \frac{e^{-i(\vec{k}-\vec{k}')\cdot\vec{R}}}{N} \left((e^{-ik_{x_1}a_0} + e^{-ik_{x_2}a_0} + h.c.) - 4 \right) c_{\vec{k}}^\dagger c_{\vec{k}'} \\ &= \frac{1}{a_0^2} \sum_{\vec{k}, \vec{k}'} \delta(\vec{k} - \vec{k}') (2 \cos(k_{x_1}a_0) + 2 \cos(k_{x_2}a_0) - 4) c_{\vec{k}}^\dagger c_{\vec{k}'} \\ &= \sum_{\vec{k}} E_{\vec{k}} c_{\vec{k}}^\dagger c_{\vec{k}} \end{aligned}$$

where

$$E_{\vec{k}} = -\frac{2}{a_0^2} [2 - \cos(k_1 a_0) - \cos(k_2 a_0)] = -\frac{2N^2}{L^2} \left[2 - \cos\left(\frac{n_1 \pi}{N}\right) - \cos\left(\frac{n_2 \pi}{N}\right) \right]. \quad (17)$$

is the energy spectrum of the tight-binding Hamiltonian.

3.3.2 Discretization of the wavefunction

We can discretize the wavefunction on the cube lattice so that ψ becomes a vector of dimension $6N^2$. Letting $|i\rangle$ indicate that vector with i th component 1 and all other components 0, the set $\{|i\rangle | i = 1, 2, 3, \dots, 6N^2\}$ constitutes a basis for the discretized wavefunctions. The Hamiltonian operator can be implemented as a $6N^2 \times 6N^2$ matrix H where the matrix elements are

$$\langle i | H | j \rangle = \begin{cases} -\frac{4}{a_0^2} & i = j \\ +\frac{1}{a_0^2} & i \text{ and } j \text{ are adjacent lattice sites} \\ 0 & \text{otherwise.} \end{cases}$$

By computing all of the eigenvalues and eigenvectors of the H matrix, we can obtain a complete set of wavefunctions on the cube lattice along with their energies. We expect to find discretized versions of the solvable solutions from Eqn. (5) among the eigenvectors. In these cases the energy will be determined by the tight-binding model result in Eqn. (17) rather than the wavenumber in Eqn. (7). Note that the degeneracy structure of the solvable cube wavefunctions remain unchanged and in the limit $N \rightarrow \infty$, Eqn. (5) approaches Eqn. (7).

However there are additional degeneracies due to the cosine structure of Eqn. (17) that may occur

in the tight-binding model but not in the smooth solvable wavefunctions. For example,

$$\cos\left(\frac{15\pi}{75}\right) + \cos\left(\frac{25\pi}{75}\right) = \cos\left(\frac{0\pi}{75}\right) + \cos\left(\frac{30\pi}{75}\right),$$

so the discretized versions of the wavefunctions $\psi_{15,25}$ and $\psi_{0,30}$ will be degenerate in a tight-binding model with $N = 75$. However the smooth wavefunctions $\psi_{15,25}$ and $\psi_{0,30}$ have distinct wavenumbers and thus are not degenerate in the $N \rightarrow \infty$ limit. To prevent such accidental degeneracies from occurring we exclusively use prime numbers for N .

3.3.3 Symmetry matrices

Later, it will be helpful to implement symmetries of the cube as operators on the discretized wavefunctions. The symmetry can be viewed as a mapping that sends an lattice site i to a lattice site $S(i)$ for each $i = 1, 2, 3, \dots, 6N^2$. Such symmetries can be realized as $6N^2 \times 6N^2$ matrices M_S such that

$$\langle i | M_S | j \rangle = \begin{cases} 1 & j = S(i) \\ 0 & \text{otherwise.} \end{cases}$$

The symmetry matrices can be explicitly determined by enacting the relevant symmetry on the \mathbb{R}^2 plane containing the cube net and then re-arranging the faces of the net via rotations by $\frac{\pi}{4}$ around vertices as necessary so that the net maps to itself. For example a C_3 symmetry of the cube about an axis can be realized as a $\frac{\pi}{2}$ rotation of the \mathbb{R}^2 plane about that vertex. See Fig. (29).

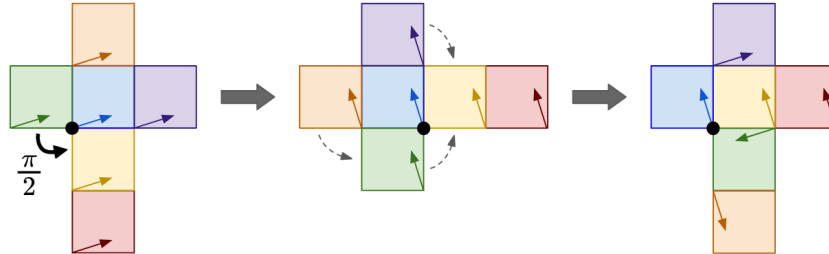


Figure 29: Realization of the C_3 cube symmetry on the net of the cube about the axis containing the vertex indicated by the black circle. The faces of the cube are colored so that they can be easily distinguished. Arrows are drawn to illustrate the rotations and reflections occurring to each face of the cube.

Eventually, we will need matrix implementations of C^3 , σ_d , C_2 and i symmetries, so we next examine the σ_d , C_2 and i symmetries. A σ_d symmetry of the cube can be realized on the cube net by reflecting the \mathbb{R}^2 plane about the line $x_1 = x_2$ and then re-arranging the net as needed. See Fig. (30).

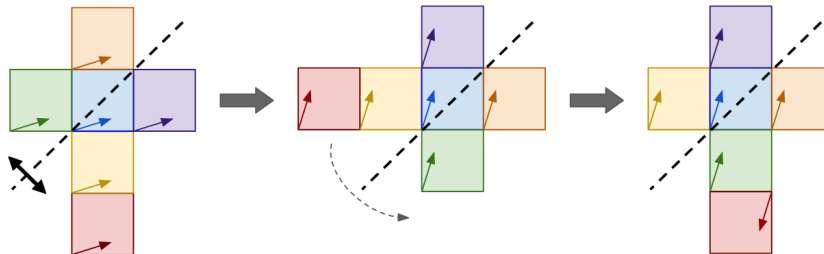


Figure 30: Realization of the σ_d cube symmetry on the net of the cube about plane containing the dashed line.

Next, a C_2 symmetry of the cube can be realized on the cube net by rotating the \mathbb{R}^2 plane about

one of the points of intersection of the symmetry axis with the cube. Again, the net can be re-arranged as necessary. See Fig. (31).

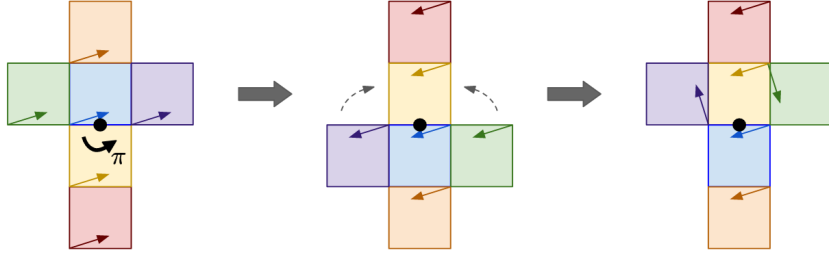


Figure 31: Realization of the C_2 cube symmetry on the net of the cube about the axis containing the black circle.

Lastly, the inversion symmetry can be obtained by performing all three of the σ_h symmetries successively. This process is illustrated in Fig. (32).

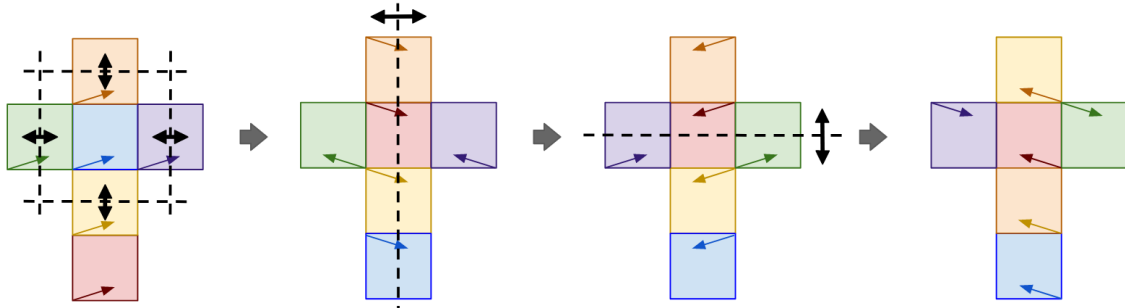


Figure 32: Realization of the i cube symmetry on the cube net. In the first step, the green, orange and purple faces are each individually reflected over their own reflection lines. The remaining three faces are reflected across the line in the yellow face so that the cube net is preserved. In the second step all six faces are reflected across the vertical dashed line. In the third step, all six faces are reflected across the horizontal dashed line and the net is re-arranged by sending the blue face to the bottom.

3.3.4 Diagonalizing the Hamiltonian

Next, note that for any discretized wavefunction $|\psi\rangle$ we may determine the expectation of any symmetry operation by computing $\langle\psi| M_S |\psi\rangle$ i.e. dotting the wavefunction vectors together using the symmetry matrix.

Next, since the Hamiltonian operator commutes with each of the symmetry operators but the symmetry operators in general do not commute, then we may simultaneously diagonalize the Hamiltonian matrix with one symmetry matrix. We chose to diagonalize H with the symmetry σ_d . Eventually, this will allow us to easily find discretized wavefunctions corresponding to degenerate solvable wavefunctions $|\psi_{n_1, n_2}\rangle$ and $|\psi_{n_1, -n_2}\rangle$. Note that the symmetric superposition $\frac{1}{\sqrt{2}}(|\psi_{n_1, n_2}\rangle + |\psi_{n_1, -n_2}\rangle)$ is an eigenvector of σ_d with eigenvalue +1 and the anti-symmetric superposition $\frac{1}{\sqrt{2}}(|\psi_{n_1, n_2}\rangle - |\psi_{n_1, -n_2}\rangle)$ is an eigenvector of σ_d with eigenvalue -1 (see Section 3.4.1).

The simultaneous diagonalization was implemented in MATLAB by generating the matrices H and σ_d separately and the computing eigenvectors and eigenvalues of the matrix $\tilde{H} = H + \phi\sigma_d$ where ϕ is the golden ratio, a scalar irrational number. Then, the energy eigenvalues of the resulting wavefunctions $|\psi\rangle$ were recovered by subtracting off $\langle\psi|\phi\sigma_d|\psi\rangle$ from the eigenvalue of $|\psi\rangle$ under \tilde{H} . Plots of the first 50 computed eigenvectors in order of increasing energy are illustrated in Appendix A.

Degenerate eigenvectors were determined by fixing a small tolerance (10^{-8}) relative to the typical eigenvalue spacings ($> 10^0$) and denoting eigenvectors whose eigenvalues differ by less than the tolerance as degenerate. Then, the O_h symmetry group acts on the space spanned by the eigenvectors in each degenerate energy level via a representation of the O_h group.

3.4 Representations of the cube symmetry group

Any representation of O_h must be either one of ten irreducible representations (irreps) of O_h or a direct product of multiple irreps of O_h . A straightforward way to determine which representation of O_h is acting on a vector space is to calculate traces of the symmetry operators acting on the vector space. For example, for a n -degenerate energy level spanned by eigenvectors $\{\psi_1, \psi_2, \dots, \psi_n\}$ the trace of a symmetry operator M_S is calculated as

$$\text{tr}(M_S) = \chi(M_S) = \sum_{i=1}^n \langle \psi_i | M_S | \psi_i \rangle.$$

The traces of symmetries belonging to the same conjugacy class are always identical. Therefore, it is informative to present the traces of each conjugacy class of O_h for each irreducible representation of O_h in a character table as shown in Table (3).

O_h	E	$8C_3$	$6C_2$	$6C_4$	$3(C_4)^2$	i	S_4	$8S_6$	$3\sigma_h$	$6\sigma_d$
A_{1g}	+1	+1	+1	+1	+1	+1	+1	+1	+1	+1
A_{2g}	+1	+1	-1	-1	+1	+1	-1	+1	+1	-1
E_g	+2	-1	0	0	+2	+2	0	-1	+2	0
T_{1g}	+3	0	-1	+1	-1	+3	+1	0	-1	-1
T_{2g}	+3	0	+1	-1	-1	+3	-1	0	-1	+1
A_{1u}	+1	+1	+1	+1	+1	-1	-1	-1	-1	-1
A_{2u}	+1	+1	-1	-1	+1	-1	+1	-1	-1	+1
E_u	+2	-1	0	0	+2	-2	0	+1	-2	0
T_{1u}	+3	0	-1	+1	-1	-3	-1	0	+1	+1
T_{2u}	+3	0	+1	-1	-1	-3	+1	0	+1	-1

Table 3: Character table for O_h [11]

Then the representation can be determined by matching the set of traces of each conjugacy class with the traces indicated in the character table. If the representation is irreducible, the traces will exactly match one of the rows of the table. Otherwise, if the representation is reducible, the traces will exactly match a sum of several rows of the table.

In our case, it suffices to calculate traces of the C_3 , C_2 , i and σ_d symmetries. In almost all energy levels, the representations are irreducible. The only exception consists of doubly-degenerate energy levels containing a symmetric and an anti-symmetric superposition of two degenerate solvable wavefunctions. However, since the symmetric and anti-symmetric superpositions of degenerate solvable wavefunctions are eigenvectors of all the symmetry operations then they should belong to a one-dimensional representation.

The presence of reducible representations of O_h among the energy spectra of H indicates an additional symmetry in the configuration of the system. In particular, adding a corner potential $V\delta(\vec{v})$ on the cube breaks the degeneracy between $\frac{1}{\sqrt{2}}(\psi_{n_1,n_2} + \psi_{n_1,-n_2})$ and $\frac{1}{\sqrt{2}}(\psi_{n_1,n_2} - \psi_{n_1,-n_2})$ since $\frac{1}{\sqrt{2}}(\psi_{n_1,n_2} + \psi_{n_1,-n_2})$ attains a maximal value at every vertex while $\frac{1}{\sqrt{2}}(\psi_{n_1,n_2} - \psi_{n_1,-n_2})$ vanishes at every vertex. The corner potential is configured in the tight-binding model by setting $\langle i | H | i \rangle = V$ for some non-zero real constant V at all lattice points i which are one of the three lattice points nearest to each vertex of the cube.

Since eigenfunctions that transform according to different irreps must have different energy eigenvalues, they belong to different eigenspaces of the H matrix. More formally, the Hamiltonian matrix is block diagonalized by the ten irreps i.e. $\langle \psi_{n_1, n_2}^{(\Gamma)} | H | \psi_{n'_1, n'_2}^{(\Gamma')} \rangle = E_{n_1, n_2} \delta_{\Gamma, \Gamma'}$ where $\psi_{n_1, n_2}^{(\Gamma)}$ is an eigenfunction that transforms according to irrep Γ and $\psi_{n'_1, n'_2}^{(\Gamma')}$ transforms according to Γ' . Thus, we can search for indicators of unsolvability within the ten subspaces spanned by eigenvectors transforming according to each irrep separately.

3.4.1 Irreps of the solvable cube wavefunctions

We conclude this section by determining the representations of O_h acting on the solvable cube wavefunctions. Since we only need to consider one-dimensional irreps, it suffices to consider the eigenvalues of the solvable wavefunctions under the symmetries σ_d and σ_h to distinguish the four one-dimensional irreps.

First consider the σ_d symmetry. Note that performing the transformation $(x_1, x_2) \rightarrow (x_2, x_1)$ on ψ_{n_1, n_2} precisely gives the degenerate wavefunction $\psi_{n_1, -n_2}$ and vice versa. Equivalently, in bra-ket notation,

$$\sigma_d |\psi_{n_1, n_2}\rangle = |\psi_{n_1, -n_2}\rangle.$$

Thus, the expectation of σ_d for non-degenerate solvable wavefunctions is

$$\langle \psi_{n_1, n_1} | \sigma_d | \psi_{n_1, n_1} \rangle = \langle \psi_{n_1, n_1} | \psi_{n_1, -n_1} \rangle = +1.$$

Similarly, for symmetric superpositions of degenerate solvable wavefunctions,

$$\begin{aligned} \left(\frac{\langle \psi_{n_1, n_2} | + \langle \psi_{n_1, -n_2} |}{\sqrt{2}} \right) \sigma_d \left(\frac{|\psi_{n_1, n_2}\rangle + |\psi_{n_1, -n_2}\rangle}{\sqrt{2}} \right) &= \frac{\langle \psi_{n_1, -n_2} | \sigma_d | \psi_{n_1, n_2} \rangle + \langle \psi_{n_1, n_2} | \sigma_d | \psi_{n_1, -n_2} \rangle}{2} \\ &= \frac{\langle \psi_{n_1, -n_2} | \psi_{n_1, -n_2} \rangle + \langle \psi_{n_1, n_2} | \psi_{n_1, n_2} \rangle}{2} \\ &= +1, \end{aligned}$$

and for the anti-symmetric superpositions

$$\begin{aligned} \left(\frac{\langle \psi_{n_1, n_2} | - \langle \psi_{n_1, -n_2} |}{\sqrt{2}} \right) \sigma_d \left(\frac{|\psi_{n_1, n_2}\rangle - |\psi_{n_1, -n_2}\rangle}{\sqrt{2}} \right) &= -\frac{\langle \psi_{n_1, -n_2} | \sigma_d | \psi_{n_1, n_2} \rangle + \langle \psi_{n_1, n_2} | \sigma_d | \psi_{n_1, -n_2} \rangle}{2} \\ &= -\frac{\langle \psi_{n_1, -n_2} | \psi_{n_1, -n_2} \rangle + \langle \psi_{n_1, n_2} | \psi_{n_1, n_2} \rangle}{2} \\ &= -1. \end{aligned}$$

Next note that the σ_h symmetry can be realized via a reflection about the line $x_1 = \frac{L}{2}$ in the plane \mathbb{R}^2 . We make the transformation $x_1 \rightarrow L - x_1$ in the wavefunction $\psi_{n_1, n_2}(\vec{x})$ and obtain

$$\begin{aligned} \psi_{n_1, n_2}(L - x_1, x_2) &= A_{n_1, n_2} \left[\cos \left(\frac{\pi}{L} (n_1(L - x_1) + n_2 x_2) \right) + \cos \left(\frac{\pi}{L} (n_1 x_2 - n_2(L - x_1)) \right) \right] \\ &= A_{n_1, n_2} \left[(-1)^{n_1} \cos \left(\frac{\pi}{L} (-n_1 x_1 + n_2 x_2) \right) + (-1)^{n_2} \cos \left(\frac{\pi}{L} (n_1 x_2 + n_2 x_1) \right) \right] \\ &= \begin{cases} \psi_{n_1, -n_2}(\vec{x}) & n_1, n_2 \text{ even} \\ -\psi_{n_1, -n_2}(\vec{x}) & n_1, n_2 \text{ odd.} \end{cases} \end{aligned}$$

Therefore,

$$\sigma_h |\psi_{n_1, n_2}\rangle = (-1)^{n_1} |\psi_{n_1, -n_2}\rangle = \begin{cases} |\psi_{n_1, -n_2}\rangle & n_1, n_2 \text{ even} \\ -|\psi_{n_1, -n_2}\rangle & n_1, n_2 \text{ odd.} \end{cases}$$

Thus, the expectation of σ_h for symmetric and anti-symmetric superpositions of degenerate solvable wavefunctions is

$$\left(\frac{\langle \psi_{n_1, n_2} | \pm \langle \psi_{n_1, -n_2} |}{\sqrt{2}} \right) \sigma_h \left(\frac{|\psi_{n_1, n_2}\rangle \pm |\psi_{n_1, -n_2}\rangle}{\sqrt{2}} \right) = \pm (-1)^{n_1}.$$

Finally, we can classify all of the solvable wavefunctions into irreps as shown in Table (4). It is clear that accidental degeneracies can occur between irreps A_{1g} and A_{1u} and between irreps A_{2g} and A_{2u} . We thus can compute the characters for the accidental degeneracies in Table (5).

Wavefunction	Parity of n_1, n_2	$\langle \sigma_d \rangle$	$\langle \sigma_h \rangle$	Irrep
$\frac{1}{\sqrt{2}}(\psi_{n_1, n_2}\rangle + \psi_{n_1, -n_2}\rangle)$	even	+1	+1	A_{1g}
$\frac{1}{\sqrt{2}}(\psi_{n_1, n_2}\rangle + \psi_{n_1, -n_2}\rangle)$	odd	+1	-1	A_{2u}
$\frac{1}{\sqrt{2}}(\psi_{n_1, n_2}\rangle - \psi_{n_1, -n_2}\rangle)$	even	-1	-1	A_{1u}
$\frac{1}{\sqrt{2}}(\psi_{n_1, n_2}\rangle - \psi_{n_1, -n_2}\rangle)$	odd	-1	+1	A_{2g}

Table 4: Irreps of the solvable cube wavefunctions

D_{2h}	E	$8C_3$	$6C_2$	$6C_4$	$3(C_4)^2$	i	S_4	$8S_6$	$6\sigma_h$	$3\sigma_d$
$A_{1g} + A_{1u}$	+2	+2	+2	+2	+2	0	0	0	0	0
$A_{2g} + A_{2u}$	+2	+2	-2	-2	+2	0	0	0	0	0

Table 5: Character table for accidental degeneracies of the cube wavefunctions

Based on Tables (3) and (5), we note that it suffices to calculate traces of the symmetries C_2, C_3, i and σ_d to differentiate all the charge sectors and potential accidental degeneracies.

3.4.2 Counting solvable wavefunctions

Classification of the solvable wavefunctions allows us to count the number of solvable wavefunctions in each irrep. The tight-binding model places an upper limit of $|n_1| \leq N$ and $|n_2| \leq N$. It also suffices to consider non-negative values for n_1 and n_2 . There are $\lceil \frac{N}{2} \rceil$ wavefunctions ψ_{n_1, n_1} with n_1 even and $\lfloor \frac{N}{2} \rfloor$ wavefunctions ψ_{n_1, n_1} with n_1 odd and $n_1 < N$. There are $\binom{\lceil \frac{N}{2} \rceil}{2}$ symmetric superpositions with n_1 and n_2 both even and unequal. Similarly, there are $\binom{\lfloor \frac{N}{2} \rfloor}{2}$ symmetric superpositions with n_1 and n_2 both odd, unequal, and $n_1, n_2 < N$. Lastly, there are $\binom{\lfloor \frac{N}{2} \rfloor}{2}$ anti-symmetric superpositions with n_1 and n_2 both even and non-zero, and there are $\binom{\lceil \frac{N}{2} \rceil}{2}$ anti-symmetric superpositions with n_1 and n_2 both odd and unequal. Noting that $n + \binom{n}{2} = \binom{n+1}{2}$, we obtain the number of solvable wavefunctions in each irrep:

$$A_{1g} : \binom{\lceil \frac{N}{2} \rceil + 1}{2} \quad A_{1u} : \binom{\lfloor \frac{N}{2} \rfloor}{2} \quad A_{2g} \text{ and } A_{2u} : \binom{\lceil \frac{N}{2} \rceil}{2}.$$

We note that the expected proportion of solvable wavefunctions among the complete set of wavefunctions in the $N \rightarrow \infty$ limit can be calculated as

$$\lim_{N \rightarrow \infty} \frac{\binom{\lceil \frac{N}{2} \rceil + 1}{2} + \binom{\lfloor \frac{N}{2} \rfloor}{2} + 2\binom{\lceil \frac{N}{2} \rceil}{2}}{6N^2} = \frac{1}{12}, \quad (18)$$

as expected.

3.5 Energy level statistics

Ultimately, we aim to show that the one-dimensional irreps consist solely of solvable wavefunctions while the higher dimensional irreps solely contain unsolvable and quantum chaotic wavefunctions via an analysis of the energy level statistics within each irrep.

3.5.1 Level spacing ratios

We first use a conjecture from random matrix theory that the consecutive energy level spacings of a Hamiltonian whose classical counterpart is integrable follow a distinct probability distribution in comparison to Hamiltonians whose classical counterpart is non-integrable.

More precisely, we define the energy spacings as $\delta_n \equiv E_{n+1} - E_n$. Then, the Berry-Tabour conjecture states that the energy spacings of the Hamiltonian of an integrable system follow a Poisson distribution $\mathbb{P}(\delta) = e^{\delta/\lambda}$ [12]. Meanwhile, the Bohigas-Giannoni-Schmit conjecture states that the energy spacings of the Hamiltonian of a quantum chaotic system follow the same energy spacings as one of three classical random matrix ensembles [9,13,14] which, in turn, follow a Wigner-Dyson distribution $\mathbb{P}(\delta) = \delta^\beta e^{-\delta^2/\lambda^2}$ [15,16]. Here, λ is a parameter, and β is the Dyson index that varies according to the random matrix ensemble as follows:

$$\begin{cases} \beta = 1 & \text{GOE (Gaussian Orthogonal Ensemble)} \\ \beta = 2 & \text{GUE (Gaussian Unitary Ensemble)} \\ \beta = 4 & \text{GSE (Gaussian Symplectic Ensemble).} \end{cases}$$

Here, matrix ensemble refers to a Hermitian matrix whose entries are real (GOE), complex (GUE), or quaternionic (GSE) and vary according to identical and independent distributions.

Next, we classify the Hamiltonian in Eqn. (15) into one of the random matrix ensembles. Since the system contains no spin, the time reversal operator is $\hat{T} = \hat{K}$ where \hat{K} is the anti-unitary complex conjugation operator. Note Eqn. (15) is invariant under \hat{K} since $\hat{K}c_{\vec{x}}\hat{K}^{-1} = c_{\vec{x}}$, so the Hamiltonian does not follow GUE statistics. Furthermore, $K^2 = 1$, eliminating GSE statistics, so the Hamiltonian must follow GOE statistics.

Histograms of the consecutive energy level spacings within each irrep were plotted in Fig. (33) for the one-dimensional irreps and in Fig. (34) for the higher dimensional irreps.

From inspection, it is clear that the energy spacing distributions in the one-dimensional irreps generally decrease as the energy spacing increases, consistent with the Poisson distribution. Meanwhile, the energy spacing distributions in higher-dimensional irreps tend toward zero as the energy spacing approaches zero, consistent with the Wigner-Dyson distribution. This is known as energy level repulsion.

A more rigorous method to quantify how well the energy spacing levels follow a Poisson or Wigner-Dyson distribution is to compute the mean level spacing ratio (LSR) denoted $r = \langle r_n \rangle$ where r_n is defined as [15,17]

$$r_n \equiv \frac{\min(\delta_n, \delta_{n+1})}{\max(\delta_n, \delta_{n+1})}.$$

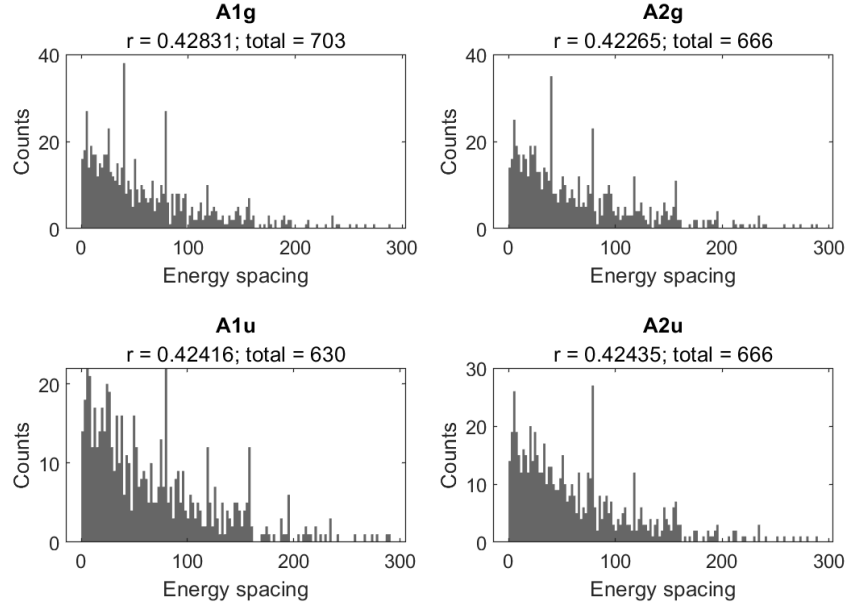


Figure 33: Energy-level spacing histograms for the one-dimensional irreps. The total number of eigenfunctions in each irrep and the mean level spacing ratio r are indicated in the subtitle of each plot.

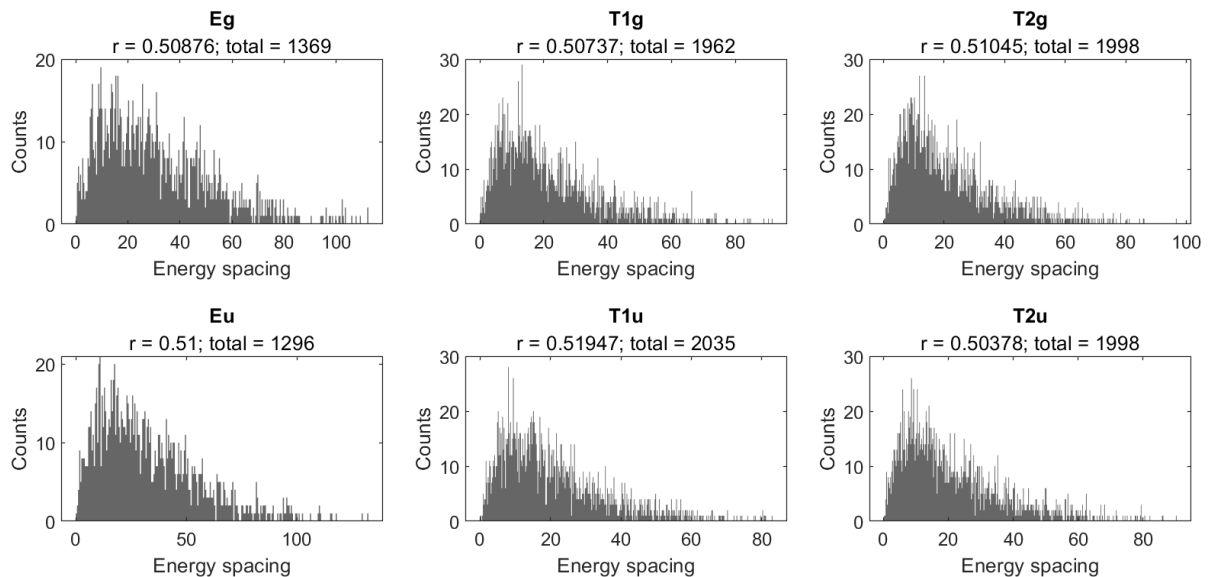


Figure 34: Energy-level spacing histogram for the two- and three-dimensional irreps. The total number of eigenfunctions in each irrep and the mean level spacing ratio r are indicated in the subtitle of each plot.

Then the value of $r = \langle r_n \rangle$ indicates the probability distribution as follows [15]:

$$r = \begin{cases} 2\ln 2 - 1 \approx 0.39 & \text{Poisson} \\ 4 - 2\sqrt{3} \approx 0.53 & \text{Wigner-Dyson, } \beta = 1 \text{ (GOE)} \\ 2\frac{\sqrt{3}}{\pi} - \frac{1}{2} \approx 0.60 & \text{Wigner-Dyson, } \beta = 2 \text{ (GUE)} \\ \frac{32}{15}\frac{\sqrt{3}}{\pi} - \frac{1}{2} \approx 0.68 & \text{Wigner-Dyson, } \beta = 4 \text{ (GSE)}. \end{cases}$$

Thus, we expect $r \rightarrow 0.39$ as $N \rightarrow \infty$ in the one-dimensional irreps and $r \rightarrow 0.53$ as $N \rightarrow \infty$ in the higher dimensional irreps. In particular, to examine the impact of finite system size on the LSR values we plot the LSR computed in each irrep as a function of N in Figs. (35) and (36). The largest possible value of N for which my laptop has sufficient memory to handle all of the necessary computations is $N = 75$. Thus, we used primes ≤ 75 for N .

Indeed we note that $r \rightarrow 0.39$ in the one-dimensional irreps and $r \rightarrow 0.53$ in the higher dimensional irreps, indicating that deviations of r from the ideal values may be due to finite size effects. Furthermore, the computed values of r support our conjecture that the one-dimensional irreps solely contain solvable wavefunctions while the higher dimensional irreps solely contain unsolvable wavefunctions.

Another way to demonstrate this is to compare the expected number of solvable wavefunctions with the number of wavefunctions classified into the one-dimensional irreps. Consistent with Eqn. (18), the number of wavefunctions in the one-dimensional irreps approaches $\frac{1}{12}$ as N increases as shown in Fig. (37). For $N = 73$ we also predicted $\binom{\lceil \frac{N}{2} \rceil + 1}{2} = 703$ wavefunctions in the A_{1g} irrep, $\binom{\lfloor \frac{N}{2} \rfloor}{2} = 630$ solvable wavefunctions in A_{1u} irrep, and $\binom{\lceil \frac{N}{2} \rceil}{2} = 666$ in the A_{2g} and A_{2u} irreps. In all cases, the computed number of wavefunctions in the irreps agree with our predictions.

To conclude our discussion of level spacing ratios, we note that in the $N \rightarrow \infty$ limit, the solvable wavefunctions expected to be present in of the irreps A_{1g} , A_{1u} , A_{2g} , and A_{2u} show energy level spacing distributions which are clearly Poisson and the LSR approaches arbitrarily close to $2\ln 2 - 1 \approx 0.386$. An example of the solvable wavefunctions for $N = 997$ is shown in Fig. (38).

3.5.2 Spectral form factor

Another diagnostic of quantum chaos is the general form of the spectral form factor [18–20] computed as follows:

$$K(t) = \left| \sum_n e^{iE_n t} \right|^2.$$

The spectral form factor can be viewed as the square magnitude of the analytic continuation of the standard partition function into the complex plane, $Z(\beta) = Z(\beta + it)$. The spectral form factor also plays a similar role as the partition function as a normalization factor. For example, some arbitrary operator $\hat{O}(t)$ can be diagonalized in the energy eigenbasis as follows:

$$\sum_{m,n} \langle m | \hat{O}(t) | n \rangle = \sum_{m,n} e^{i(E_m - E_n)t} \langle m | \hat{O} | n \rangle.$$

When $K(t)$ is plotted as a function of t on a log-log plot, the general form (with oscillations averaged out) is known as the slope-ramp-plateau and is sketched in Fig. (39) [9]. The ramp regime between t_{Th} and t_H is characteristic of systems demonstrating energy level repulsion. Plots of the SFF for the one-dimensional charge sectors are shown in Fig. (40) and the higher-dimensional irreps in Fig. (41).

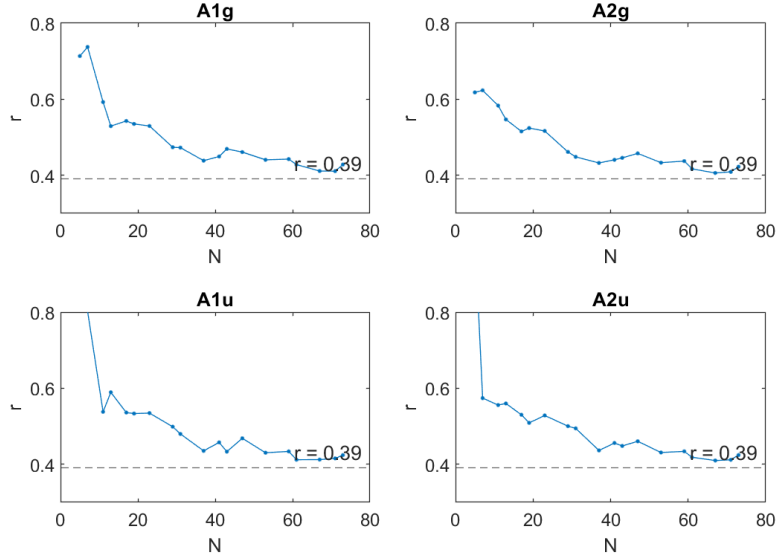


Figure 35: Plot of r values for each irrep as a function of N for the one-dimensional irreps.

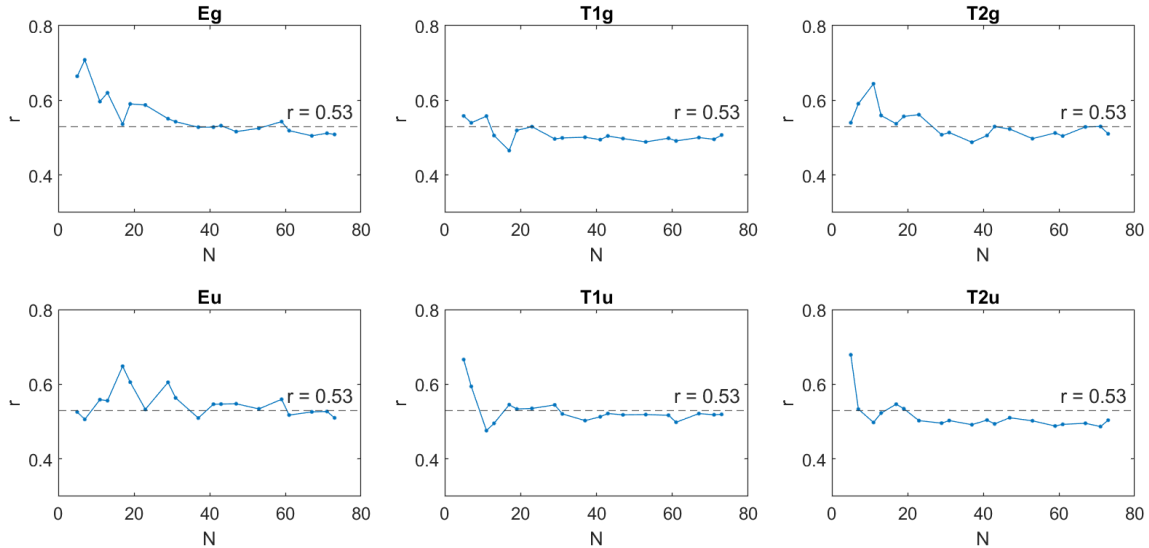


Figure 36: Plot of r values for each irrep as a function of N for the higher dimensional irreps.

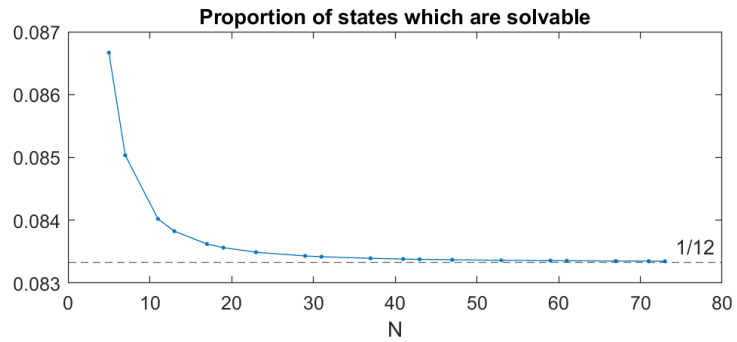


Figure 37: Plot of the proportion of eigenfunctions of \tilde{H} in the one-dimensional irreps.

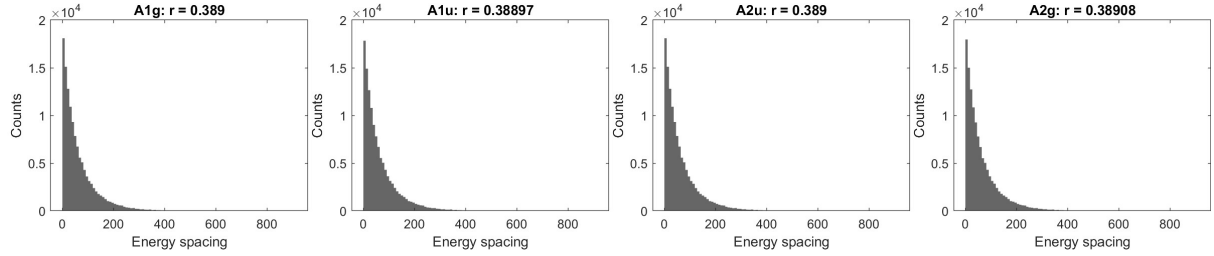


Figure 38: Distribution of energy spacings of solvable cube wavefunctions in the $N = 997$ tight-binding model.

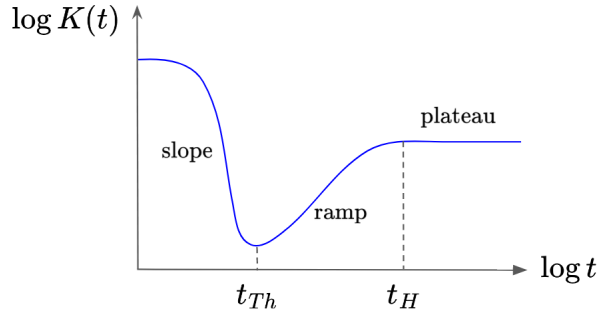


Figure 39: General form of the SFF for chaotic systems. Here, t_{Th} indicates the Thouless time and t_H indicates the Heisenberg time.

By inspection, the ramp regime is more prominent in the modes containing unsolvable wavefunctions, as expected. We conclude this chapter with a discussion on quantum scars.

3.6 Quantum scar states

Some of the computed eigenfunctions for the tight-binding model on a cube show evidence of enhanced density along unstable classical orbits, also known as quantum scars [21, 22] (see Fig. (42)). Such quantum scar states are unexpected since classically chaotic systems are ergodic, suggesting that the corresponding quantum eigenstates should uniformly explore the available phase space. Quantum scars provide corrections to this assumption. A well-known set of quantum scarred states are found on the Bunimovich stadium [23].

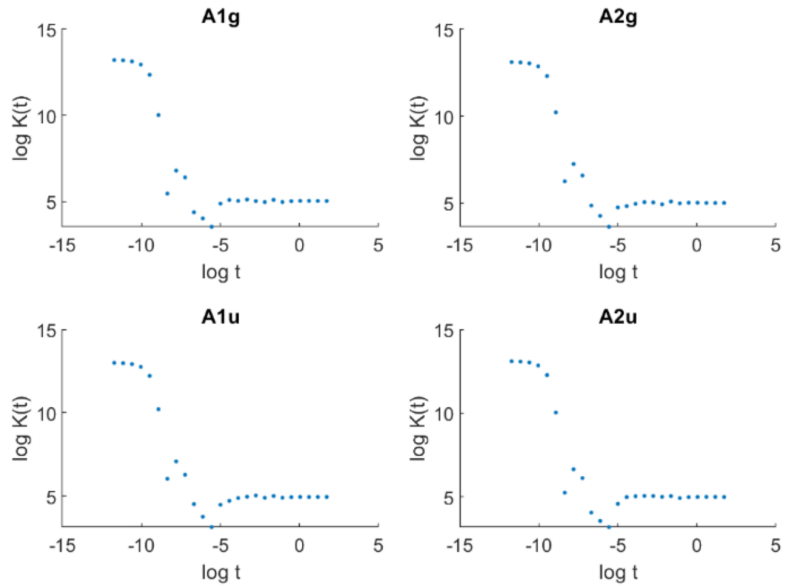


Figure 40: Averaged SFFs of the charge sectors containing solvable wavefunctions.

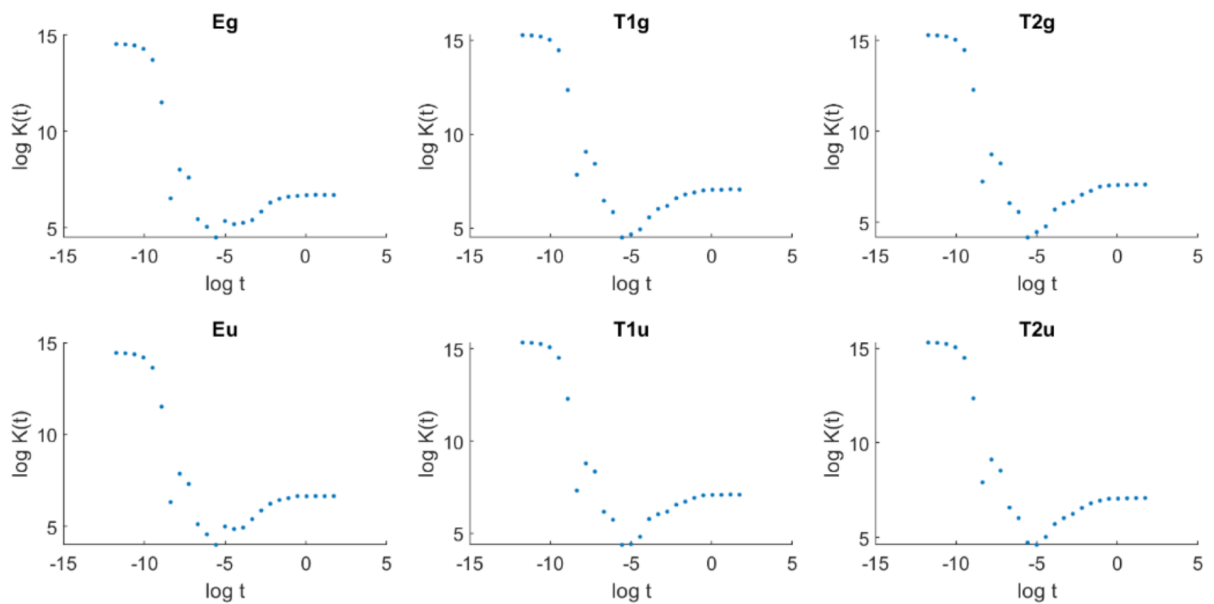


Figure 41: Averaged SFFs of the charge sectors containing unsolvable wavefunctions.

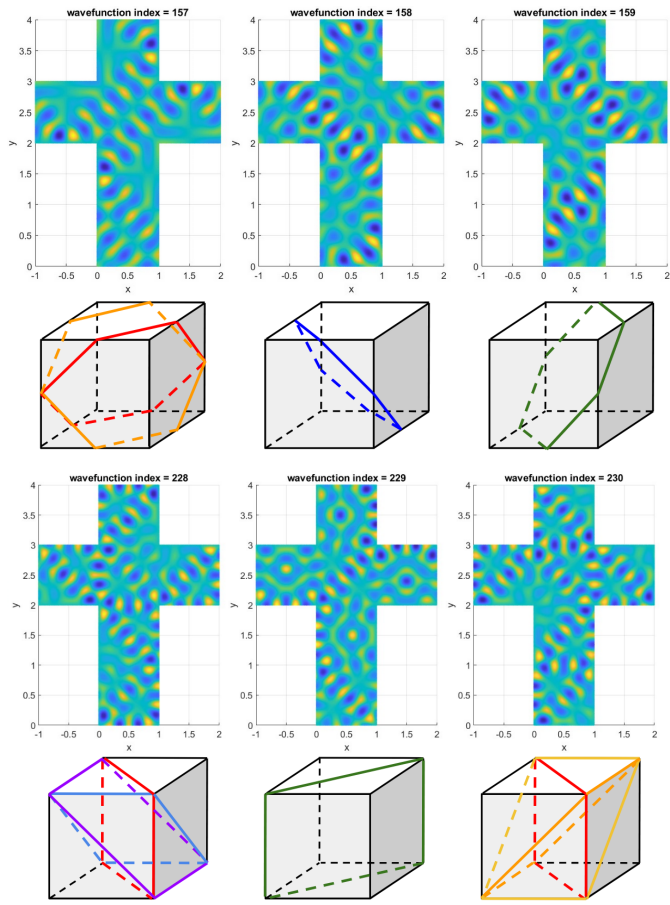


Figure 42: Two sets of three-fold degenerate cube eigenfunctions which show scarring.

4 Unsolvable wavefunctions on rectangle-faced polyhedra

In this chapter, we investigate the unsolvable wavefunctions on the square prism and the rectangular prism. First, we require the side length ratios to be rational in all cases so that non-trivial solvable wavefunctions exist.

4.1 Incompleteness of the solvable wavefunctions

4.1.1 Proof via symmetry

The square prism and rectangular prism do not have any symmetries of order 3, so the proof via symmetry cannot be directly generalized to the square prism case. However, the square prism has order 4 symmetries such as C_4 (see Fig. (44)). Since both H and C_4 are Hermitian and commute, then \mathcal{H} and C_4 are simultaneously diagonalizable. Let ψ be a simultaneous eigenstate of \mathcal{H} and C_4 , so

$$\mathcal{H}\psi = E\psi \quad \text{and } C_4\psi = \lambda\psi,$$

and since $C_4^4 = 1$ then it is required that

$$\lambda = e^{i\frac{\pi n}{2}} \tag{19}$$

for some $n = 0, 1, 2, 3$. In Section 4.3.2, we show that symmetric and anti-symmetric superpositions of all solvable modes are eigenstates of C_4 with eigenvalues ± 1 , consistent with Eqn. (19). Then, however, any linear combination of solvable modes must a purely real C_4 eigenvalue so it is impossible to construct simultaneous eigenfunctions of H and C_4 with complex C_4 eigenvalues such as $\pm i$ using only the solvable eigenfunctions of \mathcal{H} , indicating that they are incomplete.

The rectangular prism only has order 2 symmetries, so a proof of incompleteness of the solvable modes via symmetry cannot be performed in a similar manner.

4.1.2 Proof via direct computation

Additionally, the remaining proofs can be generalized. The set of solvable eigenfunctions on a rectangular prism with side lengths $L_1 = l_1 L$, $L_2 = l_2 L$ and $L_3 = l_3 L$ is identical to the set of solvable eigenfunctions on a cube with side length L . The computation of the completeness relation in Eqn. (10) thus remains correct after transforming the normalization constant as $A \rightarrow A' = \frac{2}{L\sqrt{2(l_1l_2+l_1l_3+l_2l_3)}}$. It is readily apparent that two delta functions are present in every $L \times L$ grid square so that the completeness relation does not hold.

4.1.3 Proof via thermodynamics

For the proof via thermodynamics the only change is that $V \rightarrow V' = 2(l_1l_2 + l_1l_3 + l_2l_3)L^2$ so that the expected number of states with energy below E is

$$N(E) = \frac{(l_1l_2 + l_1l_3 + l_2l_3)L^2E_0}{2\pi} \rightarrow D(E) = \frac{(l_1l_2 + l_1l_3 + l_2l_3)L^2}{2\pi}.$$

It still holds that $N_s(E) = \frac{L^2}{8\pi}E \rightarrow D_s(E) = \frac{L^2}{8\pi}$ giving the result

$$D_s(E) = \frac{D(E)}{4(l_1l_2 + l_1l_3 + l_2l_3)} \quad \Rightarrow \quad \frac{D_s(E)}{D(E)} = \frac{1}{4(l_1l_2 + l_1l_3 + l_2l_3)}.$$

Thus, the solvable wavefunctions of a square prism are incomplete and comprise only $\frac{1}{4(l_1l_2+l_1l_3+l_2l_3)}$ of the complete set of wavefunctions. We proceed to examine the remaining wavefunctions following the same procedure as the cube case. The Hamiltonian was generated based on a tight-binding model on a lattice on the square prism net with N^2 sites within each $L \times L$ grid square. The σ_d matrix was also implemented analogously and the matrices H and σ_d were simultaneously diagonalized. We use prime numbers for N and take N as large as my laptop memory allows.

4.2 Van Hove Singularity

In the remaining polyhedra discussed in this paper, the energy levels of the discretized wavefunctions all demonstrated a one or more instances of a discrete version of Van Hove singularities. A Van Hove singularity occurs in the lattice tight binding model at energies where the corresponding Fermi surface first touches the boundary of the Brillouin zone. At energies near a Van Hove singularity, the density of states sharply peaks [24]. To show this note that the total number of states below energy E can be calculated as

$$N(E) = \sum_n \sum_{\vec{k}} \Theta(E - E_{n,\vec{k}}) = V \sum_n \int \frac{d^2 \vec{k}}{(2\pi)^2} \Theta(E - E_{n,\vec{k}}),$$

where $\Theta(\cdot)$ is the step function and V is the volume of the lattice. Then the density of states is

$$D(E) = \frac{1}{V} \frac{dN(E)}{dE} = \sum_n \int \frac{d^2 \vec{k}}{(2\pi)^2} \frac{d\Theta(E - E_{n,\vec{k}})}{dE} = \sum_n \int \frac{d^2 \vec{k}}{(2\pi)^2} \delta(E - E_{n,\vec{k}}).$$

This integral can be converted to an integral on the corresponding Fermi surface in the Brillouin zone denoted FS_E^n by noting that $\delta(E - E_{\vec{k}}) = \frac{\delta(k_{\perp})}{|\nabla_{\vec{k}} E_{\vec{k}}|}$ where k_{\perp} is the component of \vec{k} perpendicular to the Fermi surface. Then

$$D(E) = \sum_n \int_{FS_E^n} \frac{dk^{\parallel}}{(2\pi)^2} \frac{1}{|\nabla_{\vec{k}} E_{\vec{k}}|}.$$

It is clear then that the integrand of $D(E)$ diverges at points where the dispersion relation $E_{\vec{k}}$ where has an extremum. For example, in a square lattice we found that $E_{\vec{k}} = -\frac{2}{a_0^2}[2 - \cos(k_1 a_0) - \cos(k_2 a_0)]$, so

$$\nabla_{\vec{k}} E_{\vec{k}} = -\frac{2}{a_0} (\sin(k_1 a_0), \sin(k_2 a_0)) = -\frac{2N}{L} \left[\sin\left(\frac{n_1 \pi}{N}\right), \sin\left(\frac{n_2 \pi}{N}\right) \right].$$

Thus, a non-trivial Van Hove singularity occurs when $\vec{k} = \frac{\pi}{L}(0, N)$ or $\vec{k} = \frac{\pi}{L}(N, 0)$. At those points $E_{\vec{k}} = -\frac{4}{a_0}$ is exactly half the maximum possible energy.

In general, we would like to ensure that as many wavefunctions can be classified into irreps as possible, so the Van Hove singularity is problematic. One way to deal with this issue is to only consider energy levels below one-half the maximum energy since we are mainly interested in the small \vec{k} case. The Van Hove singularity was not observed in the cube but was observed in all other polyhedra examined in this paper. For full disclosure, an energy cutoff was applied in the analysis of the triangle-faced polyhedra but not in the analysis of the rectangle-faced polyhedra on accident by the author.

4.3 Square prism

4.3.1 Square prism symmetries

The symmetry group of the square prism is $D_{4h} = D_4 \times \mathbb{Z}/2\mathbb{Z}$. Note that any symmetry of the square prism can be written in terms of a symmetry of the square face possibly followed by a horizontal reflection. The square has symmetry group D_4 and the horizontal reflection element commutes with the symmetries of the square giving a symmetry group of $D_{4h} = D_4 \times \mathbb{Z}/2\mathbb{Z}$ for the square prism.

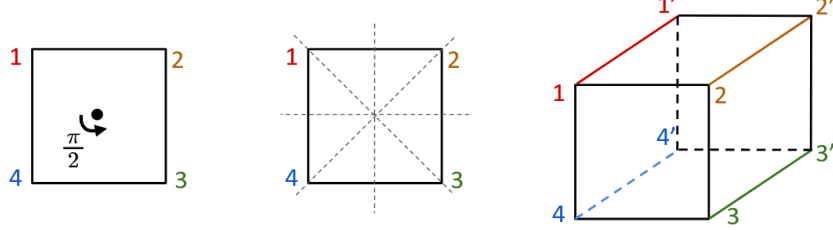


Figure 43: Rotation symmetries of the square (left), reflection symmetries of the square (middle), correspondence of square symmetries with symmetries of the square prism (right)

4.3.2 Representations of the symmetry group

The character table of D_{4h} is given in Table (??) below.

Next, we aim to determine the charge sectors to which the solvable wavefunctions belong. The solvable wavefunctions are eigenvectors of all the square prism symmetries, so they must belong to a one-dimensional charge sector. To distinguish the one-dimensional charge sectors, it suffices to consider the symmetries C_4 , σ_h and σ_d . The σ_d symmetry is still implemented in x_1x_2 space by the transformation $(x_1, x_2) \mapsto (x_2, x_1)$ which we have already studied in the cube case. Thus it remains to examine the C_4 and σ_h symmetries. The C_4 symmetry is implemented by a rotation by $\frac{\pi}{2}$ about the point $(\frac{L_1}{2}, \frac{L_1}{2})$ i.e. $(x_1, x_2) \mapsto (-x_2, x_1 - L_1)$. Making the transformation on the wavefunction $\psi_{n_1, n_2}(\vec{x})$ gives

$$\begin{aligned}\psi_{n_1, n_2}(-x_2, x_1 - L_1) &= A_{n_1, n_2} \left[\cos \left(\frac{\pi}{L} (-n_1 x_2 + n_2 (x_1 - L_1)) \right) + \cos \left(\frac{\pi}{L} (n_1 (x_1 - L_1) + n_2 x_2) \right) \right] \\ &= A_{n_1, n_2} \left[(-1)^{n_2 l_1} \cos \left(\frac{\pi}{L} (-n_1 x_2 + n_2 x_1) \right) + (-1)^{n_1 l_1} \cos \left(\frac{\pi}{L} (n_1 x_1 + n_2 x_2) \right) \right] \\ &= \begin{cases} \psi_{n_1, n_2}(\vec{x}) & n_1 l_1 \text{ even} \\ -\psi_{n_1, n_2}(\vec{x}) & n_1 l_1 \text{ odd.} \end{cases}\end{aligned}$$

Therefore,

$$C_4 |\psi_{n_1, n_2}\rangle = (-1)^{n_1 l_1} |\psi_{n_1, n_2}\rangle = \begin{cases} |\psi_{n_1, n_2}\rangle & n_1 l_1 \text{ even} \\ -|\psi_{n_1, n_2}\rangle & n_1 l_1 \text{ odd,} \end{cases}$$

so the expectation of C_4 for symmetric and anti-symmetric superpositions of degenerate solvable wavefunctions are

$$\left(\frac{\langle \psi_{n_1, n_2} | \pm \langle \psi_{n_1, -n_2} |}{\sqrt{2}} \right) C_4 \left(\frac{|\psi_{n_1, n_2}\rangle \pm |\psi_{n_1, -n_2}\rangle}{\sqrt{2}} \right) = (-1)^{n_1 l_1}.$$

Next, the σ_h symmetry can be implemented in x_1x_2 space by a reflection about the line $x_1 = -\frac{L_2}{2}$ i.e.

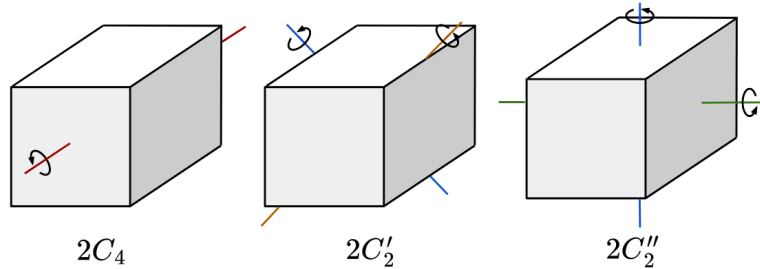


Figure 44: Rotation symmetries of the square prism

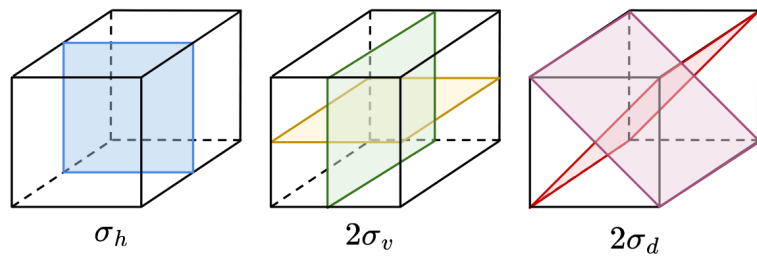


Figure 45: Reflection symmetries of the square prism.

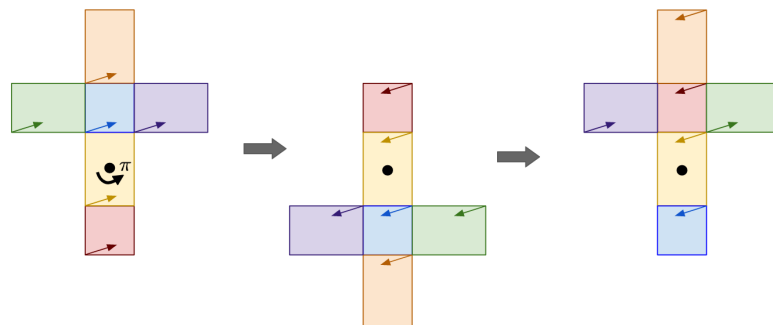


Figure 46: Implementation of a C''_2 symmetry of the square prism.

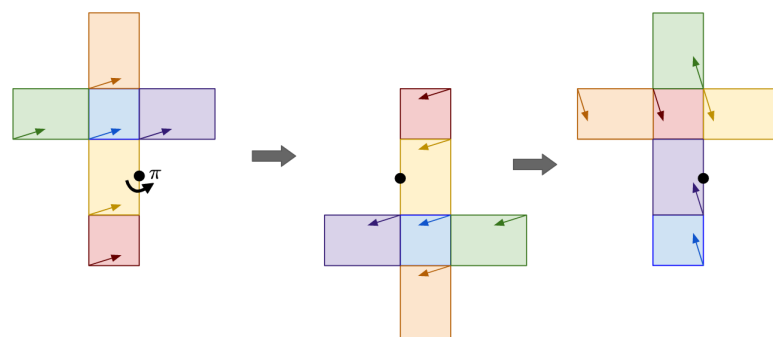


Figure 47: Implementation of a C'_2 symmetry of the square prism.

via the transformation $x_1 \mapsto -L_2 - x_1$. Making the transformation on the wavefunction $\psi_{n_1, n_2}(\vec{x})$ gives

$$\begin{aligned}\psi_{n_1, n_2}(-L_2 - x_1, x_2) &= A_{n_1, n_2} \left[\cos\left(\frac{\pi}{L}(n_1(-L_2 - x_1) + n_2 x_2)\right) + \cos\left(\frac{\pi}{L}(n_1 x_2 - n_2(-L_2 - x_1))\right) \right] \\ &= A_{n_1, n_2} \left[(-1)^{n_1 l_2} \cos\left(\frac{\pi}{L}(-n_1 x_1 + n_2 x_2)\right) + (-1)^{n_2 l_2} \cos\left(\frac{\pi}{L}(n_1 x_2 + n_2 x_1)\right) \right] \\ &= \begin{cases} \psi_{n_1, -n_2}(\vec{x}) & n_1 l_2 \text{ even} \\ -\psi_{n_1, -n_2}(\vec{x}) & n_1 l_2 \text{ odd.} \end{cases}\end{aligned}$$

Therefore,

$$\sigma_h |\psi_{n_1, n_2}\rangle = (-1)^{n_1 l_2} |\psi_{n_1, -n_2}\rangle = \begin{cases} |\psi_{n_1, -n_2}\rangle & n_1 l_2 \text{ even} \\ -|\psi_{n_1, -n_2}\rangle & n_1 l_2 \text{ odd,} \end{cases}$$

so the expectation of C_4 for symmetric and anti-symmetric superpositions of degenerate solvable wavefunctions are

$$\left(\frac{|\langle \psi_{n_1, n_2} | \pm \langle \psi_{n_1, -n_2} | \rangle|}{\sqrt{2}} \right) \sigma_d \left(\frac{|\psi_{n_1, n_2}\rangle \pm |\psi_{n_1, -n_2}\rangle}{\sqrt{2}} \right) = \pm (-1)^{n_1 l_2}.$$

Thus, the solvable wavefunctions can be classified as shown in Table (6).

Wavefunction	n_1, n_2	l_1	l_2	$\langle C_4 \rangle$	$\langle \sigma_h \rangle$	$\langle \sigma_d \rangle$	Irrep	Count
$\frac{1}{\sqrt{2}}(\psi_{n_1, n_2}\rangle + \psi_{n_1, -n_2}\rangle)$	even	odd	even	+1	+1	+1	A_{1g}	$(\lceil \frac{N}{2} \rceil + 1)_2$
$\frac{1}{\sqrt{2}}(\psi_{n_1, n_2}\rangle - \psi_{n_1, -n_2}\rangle)$	even	odd	even	+1	-1	-1	A_{1u}	$(\lfloor \frac{N}{2} \rfloor)_2$
$\frac{1}{\sqrt{2}}(\psi_{n_1, n_2}\rangle + \psi_{n_1, -n_2}\rangle)$	odd	odd	even	-1	+1	+1	B_{2g}	$(\lceil \frac{N}{2} \rceil)_2$
$\frac{1}{\sqrt{2}}(\psi_{n_1, n_2}\rangle - \psi_{n_1, -n_2}\rangle)$	odd	odd	even	-1	-1	-1	B_{2u}	$(\lceil \frac{N}{2} \rceil)_2$
$\frac{1}{\sqrt{2}}(\psi_{n_1, n_2}\rangle + \psi_{n_1, -n_2}\rangle)$	even	even	odd	+1	+1	+1	A_{1g}	$(\lceil \frac{N}{2} \rceil + 1)_2$
$\frac{1}{\sqrt{2}}(\psi_{n_1, n_2}\rangle - \psi_{n_1, -n_2}\rangle)$	even	even	odd	+1	-1	-1	A_{1u}	$(\lfloor \frac{N}{2} \rfloor)_2$
$\frac{1}{\sqrt{2}}(\psi_{n_1, n_2}\rangle + \psi_{n_1, -n_2}\rangle)$	odd	even	odd	+1	-1	+1	A_{2u}	$(\lceil \frac{N}{2} \rceil)_2$
$\frac{1}{\sqrt{2}}(\psi_{n_1, n_2}\rangle - \psi_{n_1, -n_2}\rangle)$	odd	even	odd	+1	+1	-1	A_{2g}	$(\lceil \frac{N}{2} \rceil)_2$
$\frac{1}{\sqrt{2}}(\psi_{n_1, n_2}\rangle + \psi_{n_1, -n_2}\rangle)$	even	odd	odd	+1	+1	+1	A_{1g}	$(\lceil \frac{N}{2} \rceil + 1)_2$
$\frac{1}{\sqrt{2}}(\psi_{n_1, n_2}\rangle - \psi_{n_1, -n_2}\rangle)$	even	odd	odd	+1	-1	-1	A_{1u}	$(\lfloor \frac{N}{2} \rfloor)_2$
$\frac{1}{\sqrt{2}}(\psi_{n_1, n_2}\rangle + \psi_{n_1, -n_2}\rangle)$	odd	odd	odd	-1	-1	+1	B_{1u}	$(\lceil \frac{N}{2} \rceil)_2$
$\frac{1}{\sqrt{2}}(\psi_{n_1, n_2}\rangle - \psi_{n_1, -n_2}\rangle)$	odd	odd	odd	-1	+1	-1	B_{1g}	$(\lceil \frac{N}{2} \rceil)_2$

Table 6: Irreps of the solvable square prism wavefunctions

We note that irreps A_{1g} and A_{1u} always contain the solvable wavefunctions with n_1 and n_2 both even regardless of the parity of l_1 and l_2 . For odd n_1 and n_2 , the irreps A_{1g} and A_{1u} contain solvable wavefunctions when l_1 and l_2 are both even, the irreps A_{2g} and A_{2u} contain solvable wavefunctions when l_1 is even and l_2 is odd, the irreps B_{1g} and B_{1u} contain solvable wavefunctions when l_1 and l_2 are both odd, and lastly, the irreps B_{2g} and B_{2u} contain solvable wavefunctions when l_1 is odd and l_2 is even. Thus, we can compute a character table for the accidental degeneracies given in Table (10).

Based on Tables (??) and (7), we note that it suffices to calculate traces of the symmetries C'_2, C''_2, i and σ_d to differentiate all the charge sectors and potential accidental degeneracies.

D_{2h}	E	$2C_4$	C_2	$2C'_2$	$2C''_2$	i	$2S_4$	σ_h	$2\sigma_v$	$2\sigma_d$
$A_{1g} + A_{1u}$	+2	+2	+2	+2	+2	0	0	0	0	0
$A_{2g} + A_{2u}$	+2	+2	+2	-2	-2	0	0	0	0	0
$B_{1g} + B_{1u}$	+2	-2	+2	+2	-2	0	0	0	0	0
$B_{2g} + B_{2u}$	+2	-2	+2	-2	+2	0	0	0	0	0

Table 7: Character table for accidental degeneracies of the square prism eigenstates

4.3.3 Counting solvable wavefunctions

Again the tight-binding model places limits $|n_1| \leq N$ and $|n_2| \leq N$, and we need only consider non-negative values of n_1 and n_2 . By the same argument as was used in the cube case, solvable wavefunctions with n_1 and n_2 even contribute $\binom{\lceil \frac{N}{2} \rceil + 1}{2}$ solvable wavefunctions in the A_{1g} irrep and $\binom{\lfloor \frac{N}{2} \rfloor}{2}$ solvable wavefunctions in the A_{1u} irrep. Further, the solvable wavefunctions with odd n_1 and n_2 contribute $\binom{\lfloor \frac{N}{2} \rfloor}{2}$ solvable wavefunctions in the irrep containing symmetric superpositions and $\binom{\lceil \frac{N}{2} \rceil}{2}$ solvable wavefunctions in the irrep containing anti-symmetric superpositions of wavefunctions with even and non-zero n_1 and n_2 . However, in the square prism case, these irreps vary depending on the parity of l_1 and l_2 . In total, we find the counts given in the rightmost column of Table (6).

Lastly, noting that there are a total of $(2l_1^2 + 4l_1l_2)N^2$ wavefunctions in the complete set then the proportion of solvable wavefunction in the $N \rightarrow \infty$ limit can be calculated as

$$\lim_{N \rightarrow \infty} \frac{\binom{\lceil \frac{N}{2} \rceil + 1}{2} + \binom{\lfloor \frac{N}{2} \rfloor}{2} + 2\binom{\lceil \frac{N}{2} \rceil}{2}}{(2l_1^2 + 4l_1l_2)N^2} = \frac{1}{4(l_1^2 + 2l_1l_2)}$$

as expected.

4.3.4 Energy level statistics

We proceed to examine the energy level spacing distributions (see Figs. (48) and (49)) and level spacing ratios (see Figs. (50), and (51)) within each charge sector. We first consider the example with $(l_1, l_2) = (1, 2)$ henceforth referred to as the $(1, 2)$ square prism.

First, note that the histograms in Fig. (49) demonstrate energy level repulsion, consistent with the prediction that they only contain unsolvable wavefunctions. Moreover, the $\langle r \rangle$ values in Fig. (51) converge to 0.53 as expected for a Wigner-Dyson distribution with $\beta = 1$.

However, notice that in Fig. (48), the energy spacing distribution does not vanish as $\delta_n \rightarrow 0$, consistent with a Poisson distribution. However, the distribution does not decrease uniformly, consistent with a Wigner-Dyson distribution. Similarly, note in Fig. (50) that the $\langle r \rangle$ values converge to some value between 0.39 and 0.53 as N increases. Thus, the mixture of both Poisson-like and Wigner-Dyson like properties suggest that the irreps A_{1g}, A_{1u}, B_{2g} and B_{2u} each contain a mixture of solvable and unsolvable wavefunctions.

As a last confirmation, note in Fig. (52) that the proportion of eigenfunctions in the irreps containing solvable wavefunctions converges to $\frac{1}{4}$ as $N \rightarrow \infty$ which is larger than the expected proportion of solvable wavefunctions, $\frac{1}{20}$, for a $(1, 2)$ square prism. We proceed to re-examine the A_{1g}, A_{1u}, B_{2g} and B_{2u} irreps after removing the solvable wavefunctions. We refer to these solvable wavefunctions within irreps containing a mixture of solvable and unsolvable states as quantum scar states.

The solvable modes were located within the irreps via the following procedure: no corner potential on the square prism was used, so eigenfunctions demonstrating accidental degeneracies were designated

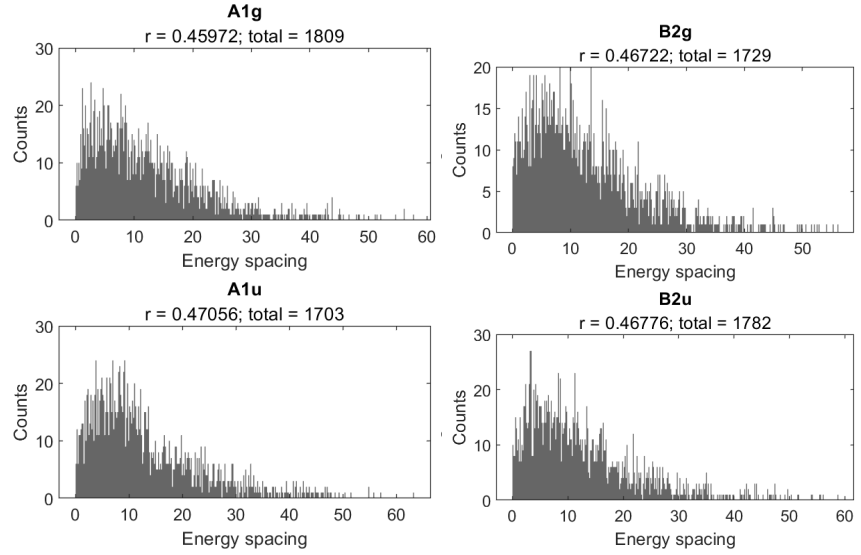


Figure 48: Energy-level spacing histograms for the irreps containing solvable (1, 2) square prism wavefunctions. The total number of eigenfunctions in each irrep and the mean level spacing ratio r are indicated in the subtitle of each plot.

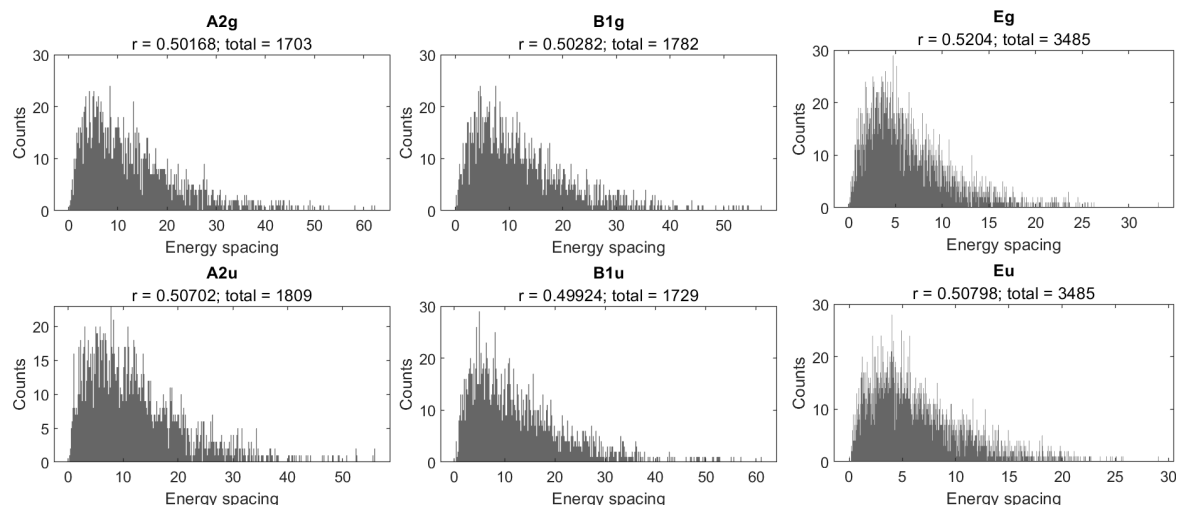


Figure 49: Energy-level spacing histogram for irreps that do not contain solvable (1, 2) square prism wavefunctions. The total number of eigenfunctions in each irrep and the mean level spacing ratio r are indicated in the subtitle of each plot.

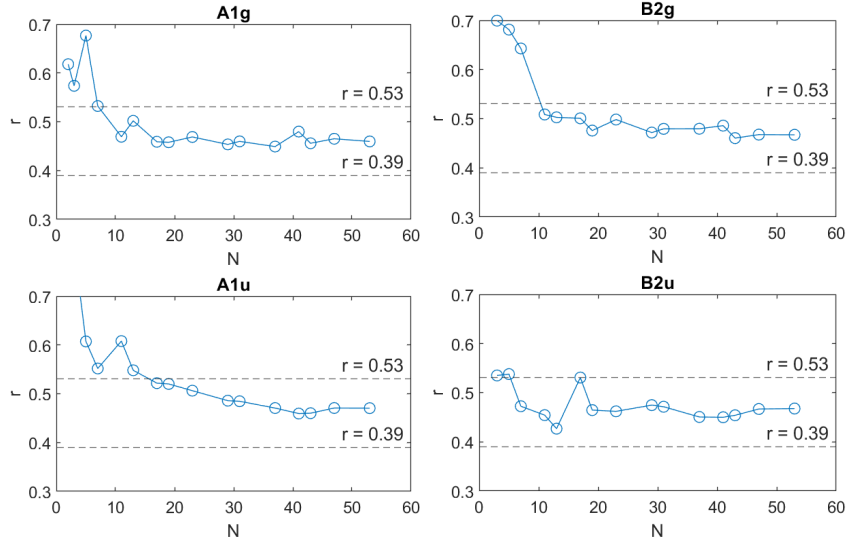


Figure 50: r values for irreps containing solvable (1, 2) square prism wavefunctions.

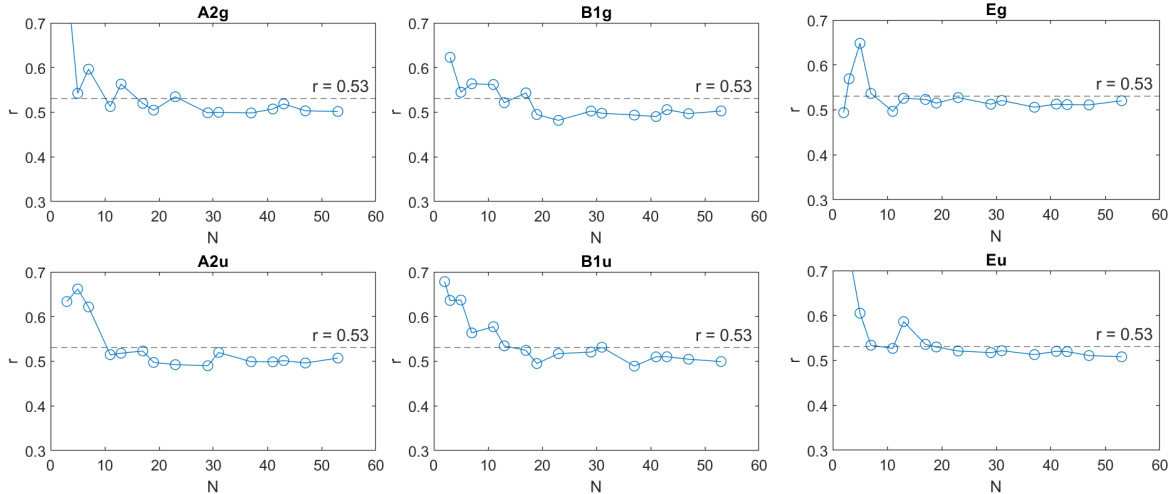


Figure 51: r values for irreps not containing solvable (1, 2) square prism wavefunctions.

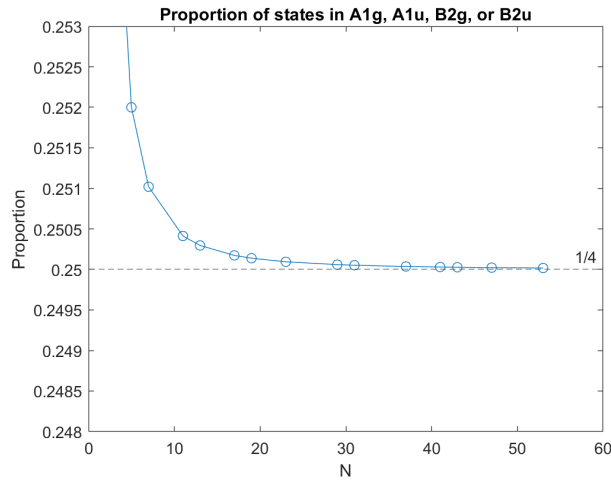


Figure 52: Proportion of eigenfunctions in irreps containing solvable wavefunctions.

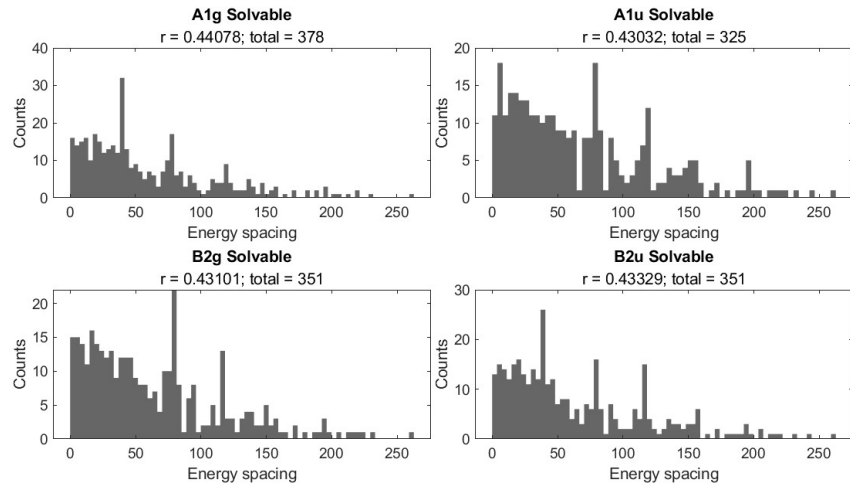


Figure 53: Energy-level spacing histogram for irreps containing solvable (1, 2) square prism wavefunctions after removal of unsolvable wavefunctions.

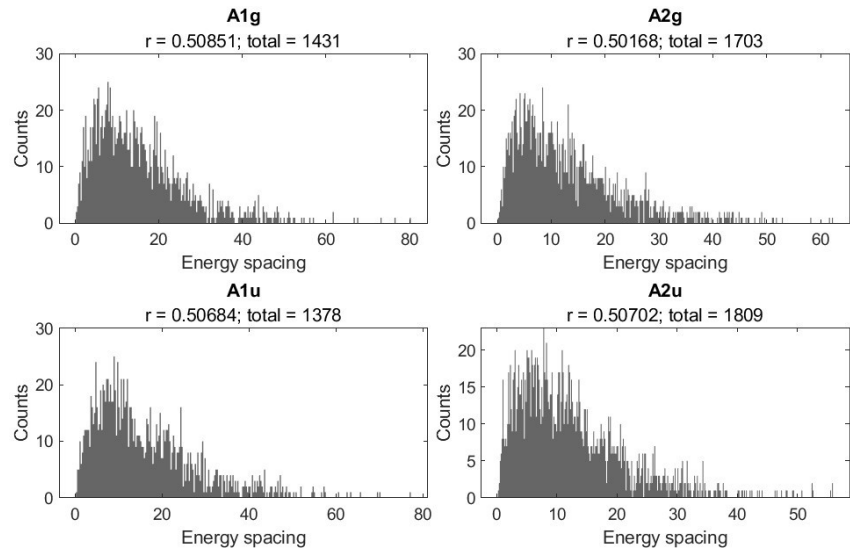


Figure 54: Energy-level spacing histogram for irreps containing solvable (1, 2) square prism wavefunctions after removal of solvable wavefunctions.

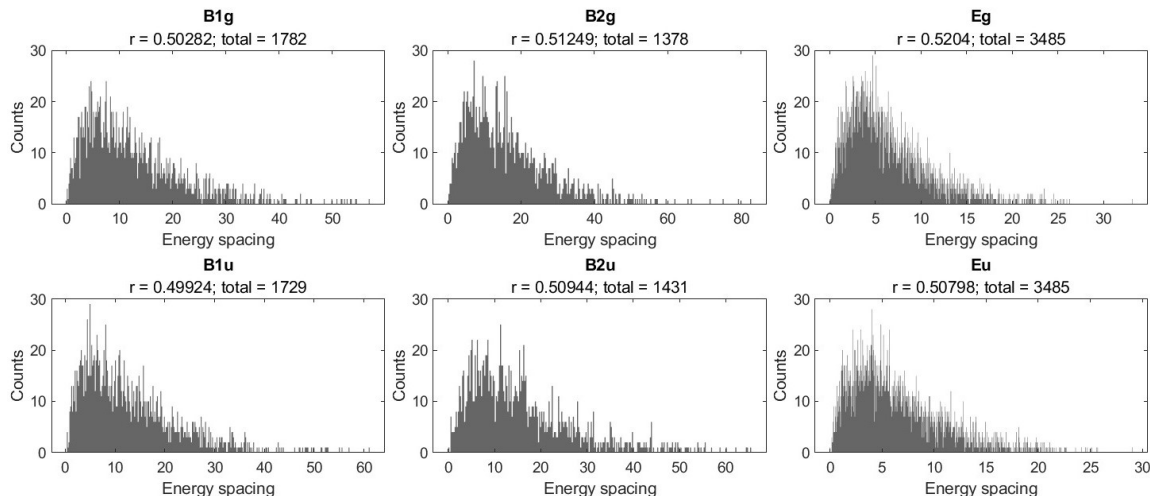


Figure 55: Energy-level spacing histograms for irreps not containing solvable (1, 2) square prism wavefunctions after removal of solvable wavefunctions

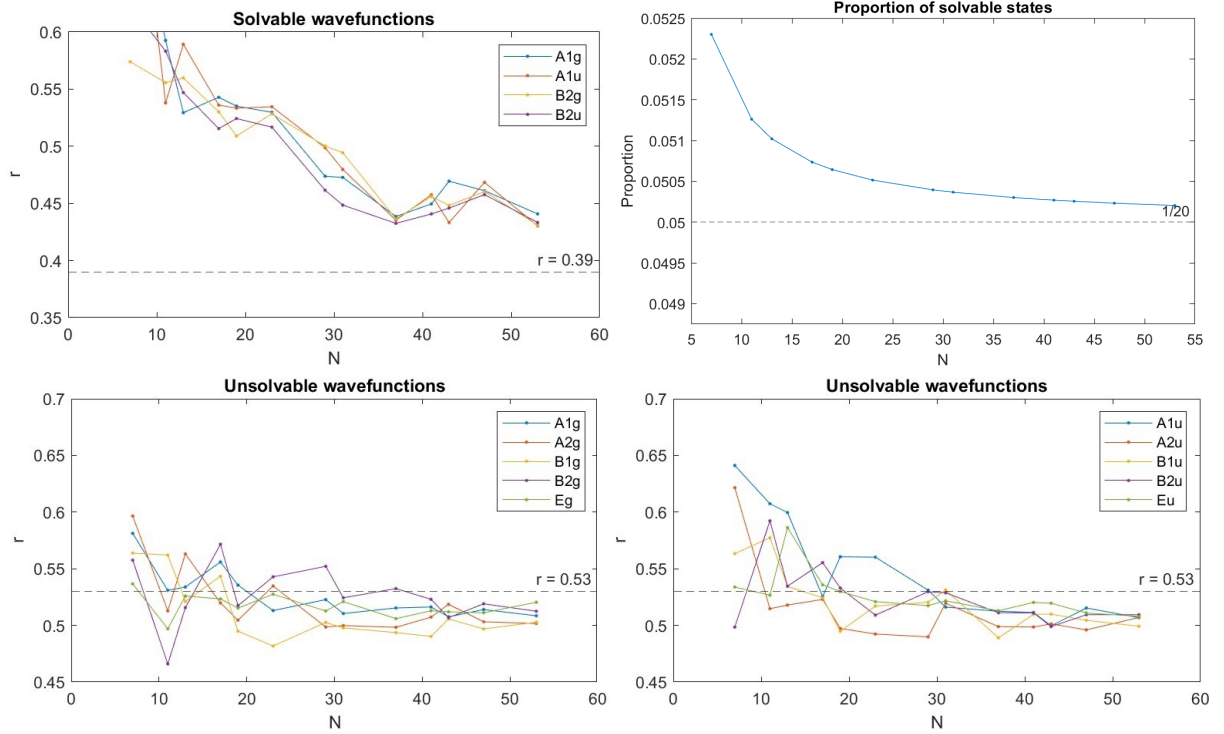


Figure 56: Top row: r values as a function of N for irreps containing solvable (1, 2) square prism wavefunctions after removal of unsolvable wavefunctions (left) and proportion of states identified as solvable (right). Bottom row: r values as a function of N for all irreps after removal of solvable wavefunctions

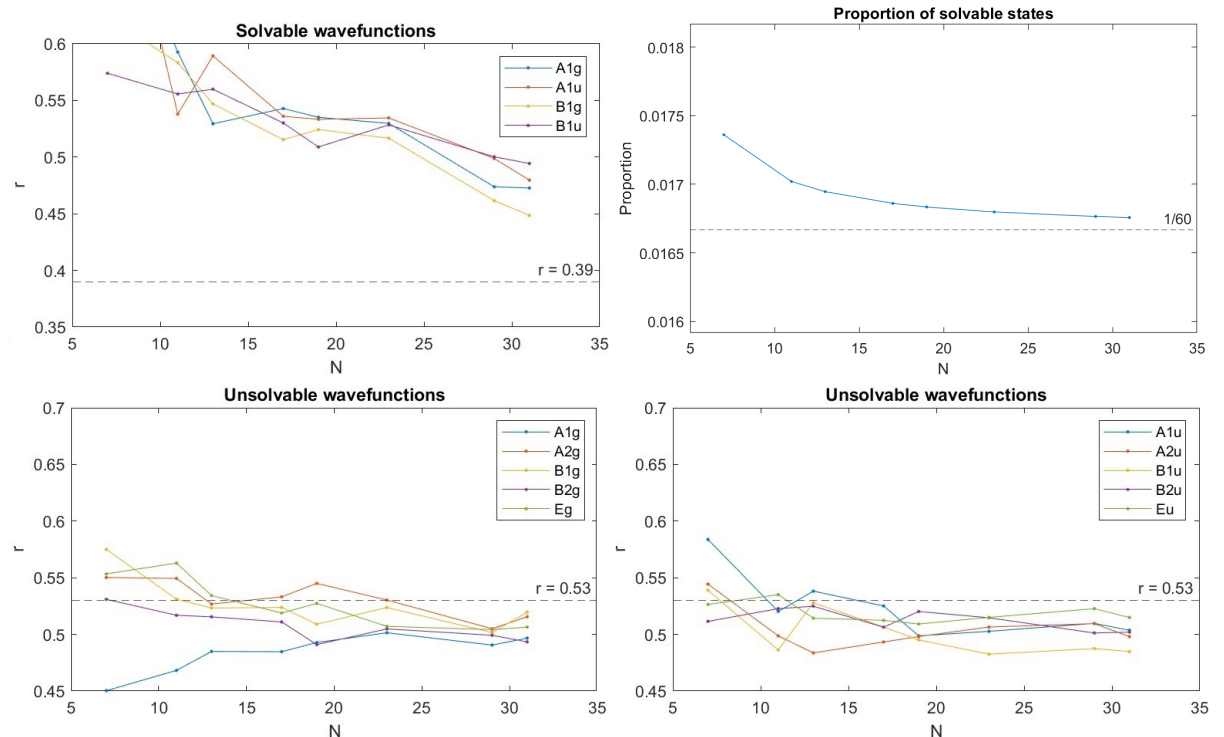


Figure 57: Top row: r values as a function of N for irreps containing solvable (3, 1) square prism wavefunctions after removal of unsolvable wavefunctions (left) and proportion of states identified as solvable (right). Bottom row: r values as a function of N for all irreps after removal of solvable wavefunctions

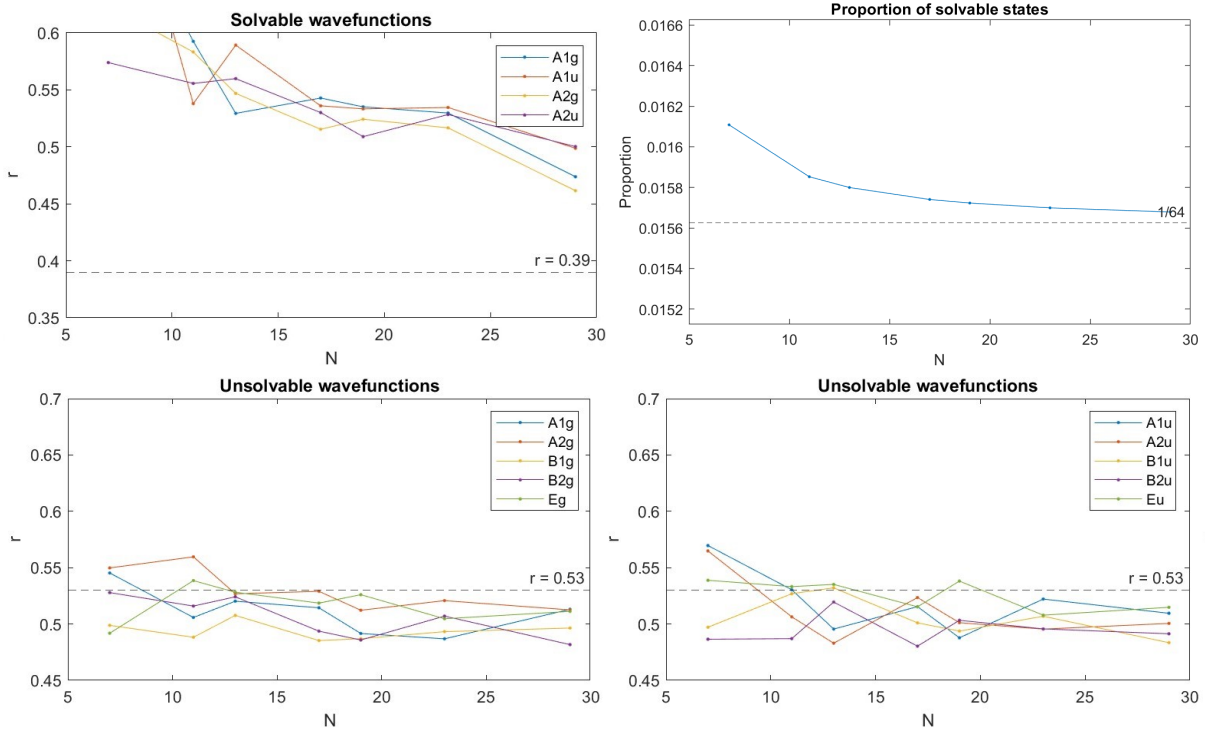


Figure 58: Top row: r values as a function of N for irreps containing solvable (2, 3) square prism wavefunctions after removal of unsolvable wavefunctions (left) and proportion of states identified as solvable (right). Bottom row: r values as a function of N for all irreps after removal of solvable wavefunctions

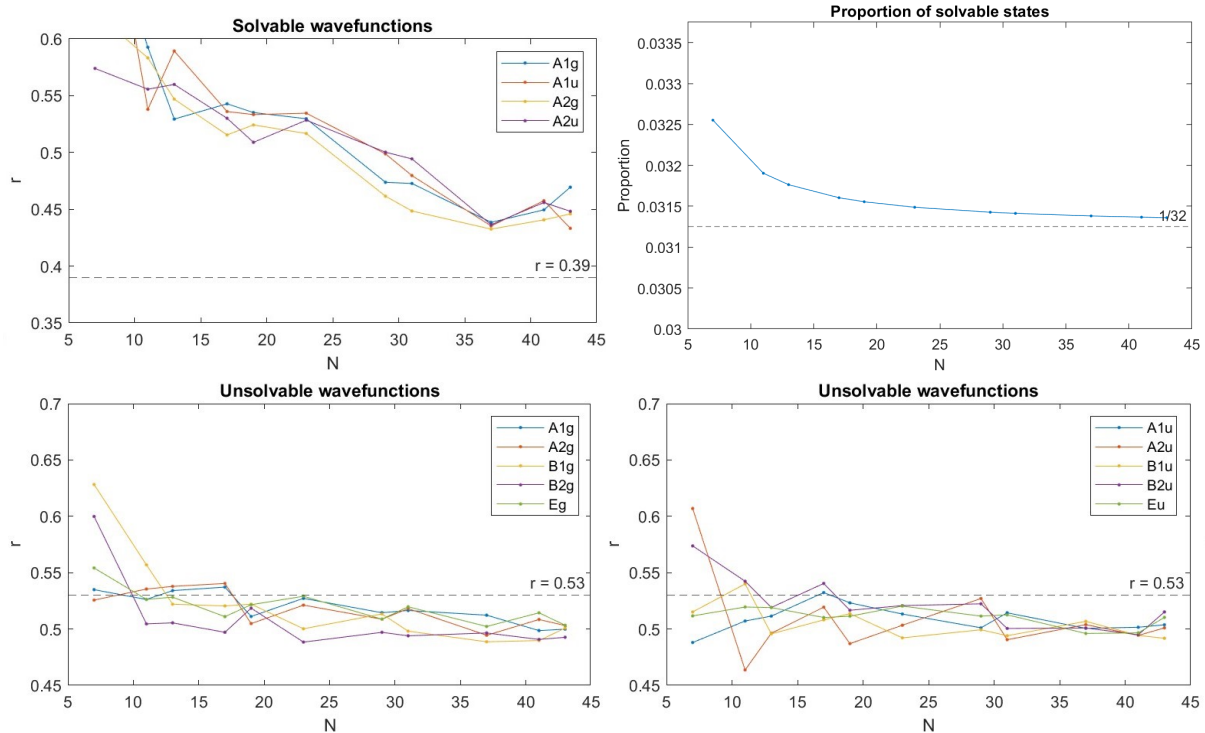


Figure 59: Top row: r values as a function of N for irreps containing solvable (2, 1) square prism wavefunctions after removal of unsolvable wavefunctions (left) and proportion of states identified as solvable (right). Bottom row: r values as a function of N for all irreps after removal of solvable wavefunctions

as solvable. The non-degenerate solvable states were then removed from the A_{1g} (and B_{2g} if l_1 is odd) irreps by matching the energies of the eigenfunctions with the energy levels predicted by the tight-binding model. After removal of the solvable modes we obtained the level spacing statistics shown in Figs. (53) through (59).

A similar analysis of $\langle r \rangle$ values was also performed on square prisms for other values of l_1 and l_2 . For brevity, only the plots of $\langle r \rangle$ as a function of N for each irrep are given after separation of the solvable wavefunctions from the remaining wavefunctions. In all cases, we note that $r \rightarrow 0.53$ for the irreps containing unsolvable wavefunctions and $r \rightarrow 0.39$ for the irreps containing solvable wavefunctions as expected.

4.3.5 Quantum scar states

Lastly, similarly to the cube case, the square prism contained some eigenfunctions showing enhanced probability density along classically unstable orbits. Some examples for the $(1, 2)$ square prism are shown in Fig. (60).

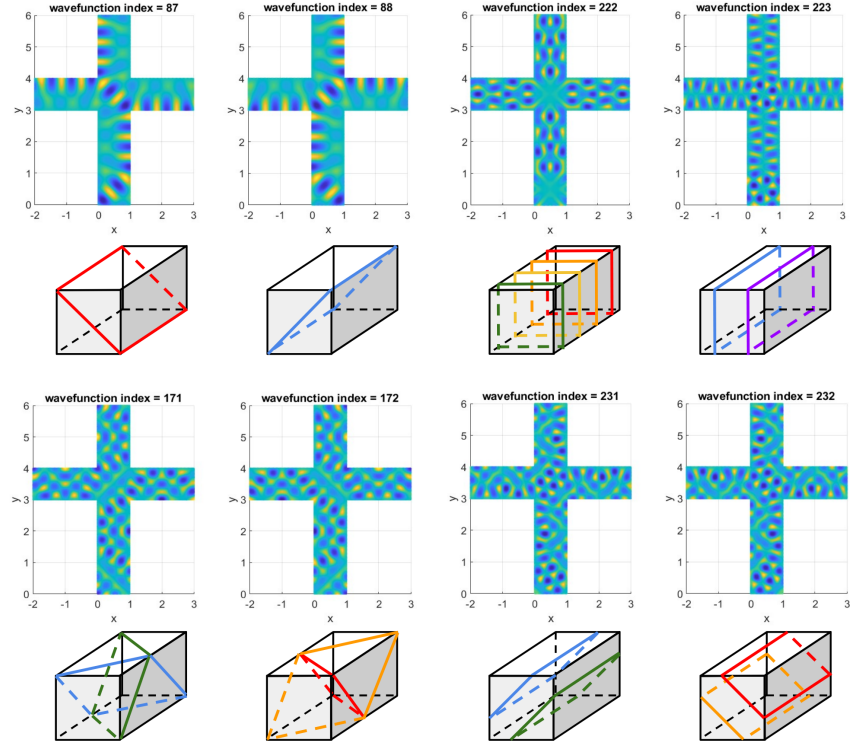


Figure 60: Four sets of doubly-degenerate eigenfunctions of the $(1, 2)$ square prism demonstrating quantum scarring along unstable classical orbits illustrated below the wavefunction plots.

4.4 Rectangular prism

4.4.1 Rectangular prism symmetries

The rectangular prism has symmetry group $D_{2h} = D_2 \times \mathbb{Z}/2\mathbb{Z}$ where D_2 is the dihedral group of order 4. Note that any symmetry of the square prism can be written in terms of a symmetry of a rectangular face possibly followed by a reflection through a plane parallel to the face (see Fig. (61)). The rectangle has symmetry group D_2 and the horizontal reflection element commutes with the symmetries of the square so the symmetry group of the rectangular prism is isomorphic to $D_{2h} = D_2 \times \mathbb{Z}/2\mathbb{Z}$.

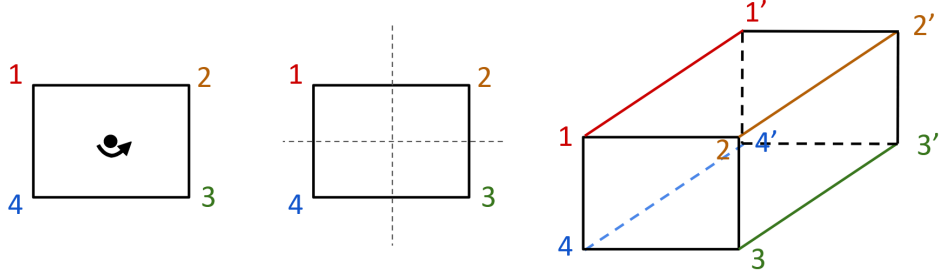


Figure 61: Correspondence of the rotational (left) and reflection (middle) symmetries of the rectangle with the symmetries of the rectangular prism (right).

The three rotation symmetries of the rectangular prism are given by π rotations about the axes as illustrated in Fig. (62). The three reflection symmetries are also illustrated in Fig. (62).

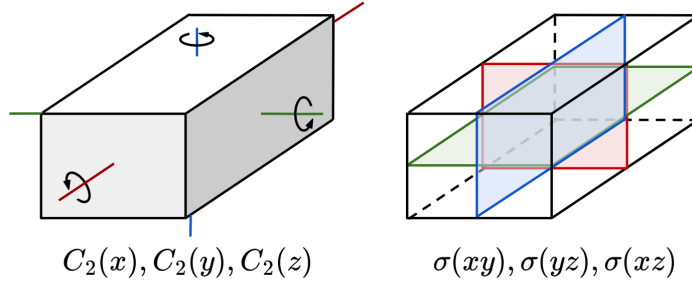


Figure 62: Rotational (left) and reflection (right) symmetries of the rectangular prism

4.4.2 Representations of the symmetry group

The character table for D_{2h} is given in Table (8). We first determine the irreps acting on the solvable wavefunctions on a rectangular prism.

D_{2h}	E	$C_2(z)$	$C_2(y)$	$C_2(x)$	i	$\sigma(xy)$	$\sigma(xz)$	$\sigma(yz)$
A_g	+1	+1	+1	+1	+1	+1	+1	+1
B_{1g}	+1	+1	-1	-1	+1	+1	-1	-1
B_{2g}	+1	-1	+1	-1	+1	-1	+1	-1
B_{3g}	+1	-1	-1	+1	+1	-1	-1	+1
A_u	+1	+1	+1	+1	-1	-1	-1	-1
B_{1u}	+1	+1	-1	-1	-1	-1	+1	+1
B_{2u}	+1	-1	+1	-1	-1	+1	-1	+1
B_{3u}	+1	-1	-1	+1	-1	+1	+1	-1

Table 8: Character table for D_{2h} [11]

We can distinguish the irreps using the symmetries $C_2(x)$, $C_2(y)$ and $\sigma(xy)$. We set our xyz axes so that $C_2(x)$ is implemented in x_1x_2 space by a rotation by π about $(\frac{L_1}{2}, L_3 + \frac{L_2}{2})$, $C_2(y)$ is a rotation by π

about $(\frac{L_1}{2}, \frac{3L_3}{2} + L_2)$. Lastly, $\sigma(xy)$ is a reflection by $x_1 = \frac{L_1}{2}$. These correspond to the transformations in the x_1x_2 plane given as $(x_1, x_2) \mapsto (-x_1 + L_1, -x_2 + L_2)$, $(x_1, x_2) \mapsto (-x_1 + L_1, -x_2 + L_3)$, and $(x_1, x_2) \mapsto (x_1, -x_2 + L_1)$, respectively. It is straightforward to verify that

$$\begin{aligned} C_2(x)|\psi_{n_1, n_2}\rangle &= (-1)^{n_1 l_1 + n_2 l_2} |\psi_{n_1, n_2}\rangle \\ C_2(y)|\psi_{n_1, n_2}\rangle &= (-1)^{n_1 l_1 + n_3 l_3} |\psi_{n_1, n_2}\rangle \\ \sigma(xy)|\psi_{n_1, n_2}\rangle &= (-1)^{n_1 l_1} |\psi_{n_1, -n_2}\rangle, \end{aligned}$$

so the symmetry expectations of symmetric and anti-symmetric superpositions of solvable wavefunctions are

$$\begin{aligned} \left(\frac{\langle \psi_{n_1, n_2} | \pm \langle \psi_{n_1, -n_2} |}{\sqrt{2}} \right) C_2(x) \left(\frac{|\psi_{n_1, n_2}\rangle \pm |\psi_{n_1, -n_2}\rangle}{\sqrt{2}} \right) &= (-1)^{n_1 l_1 + n_2 l_2} \\ \left(\frac{\langle \psi_{n_1, n_2} | \pm \langle \psi_{n_1, -n_2} |}{\sqrt{2}} \right) C_2(y) \left(\frac{|\psi_{n_1, n_2}\rangle \pm |\psi_{n_1, -n_2}\rangle}{\sqrt{2}} \right) &= (-1)^{n_1 l_1 + n_3 l_3} \\ \left(\frac{\langle \psi_{n_1, n_2} | \pm \langle \psi_{n_1, -n_2} |}{\sqrt{2}} \right) \sigma(xy) \left(\frac{|\psi_{n_1, n_2}\rangle \pm |\psi_{n_1, -n_2}\rangle}{\sqrt{2}} \right) &= \pm (-1)^{n_1 l_1}. \end{aligned}$$

Then we can determine the irreps of the solvable wavefunctions as given in Table (9). Note that when no corner potential is employed, accidental degeneracies always occur between A_u and A_g for any (l_1, l_2, l_3) . Furthermore, if all l_i are odd then accidental degeneracies only occur between A_u and A_g . In the cases where l_i and l_j (where $(j \neq i)$) have same parity while l_k (where $(i \neq k \neq j)$) has differing parity, then accidental degeneracies also occur between B_{kg} and B_{ku} . Thus, we may construct a character table for the accidentally degenerate energy levels given in Table (10). Considering Tables (8) and (10), we note that it suffices to consider the expectations of $C_2(x)$, $C_2(y)$, $C_2(z)$, and i to identify all irreps and potential accidental degeneracies.

4.4.3 Counting solvable wavefunctions

By the same argument as was employed in the cube and square prism case, solvable wavefunctions with n_1 and n_2 even contribute $\binom{\lceil \frac{N}{2} \rceil + 1}{2}$ solvable wavefunctions in the A_g irrep and $\binom{\lfloor \frac{N}{2} \rfloor}{2}$ solvable wavefunctions in the A_u irrep. Further, the solvable wavefunctions with odd n_1 and n_2 contribute $\binom{\lceil \frac{N}{2} \rceil}{2}$ solvable wavefunctions in the irrep containing symmetric superpositions of wavefunctions with odd n_1 and n_2 and $\binom{\lfloor \frac{N}{2} \rfloor}{2}$ solvable wavefunctions in the irrep containing anti-symmetric superpositions of wavefunctions with odd n_1 and n_2 . These irreps vary depending on the parity of l_1 and l_2 . In total, we find the counts given in the rightmost column of Table (9).

Lastly, noting that there are a total of $2(l_1 l_2 + l_1 l_3 + l_2 l_3)N^2$ wavefunctions in the complete set then the proportion of solvable wavefunction in the $N \rightarrow \infty$ limit can be calculated as

$$\lim_{N \rightarrow \infty} \frac{\binom{\lceil \frac{N}{2} \rceil + 1}{2} + \binom{\lfloor \frac{N}{2} \rfloor}{2} + 2\binom{\lceil \frac{N}{2} \rceil}{2}}{2(l_1 l_2 + l_1 l_3 + l_2 l_3)N^2} = \frac{1}{4(l_1 l_2 + l_1 l_3 + l_2 l_3)N^2},$$

as expected.

4.4.4 Energy level statistics

As in the square prism case, we again encounter the situation where solvable and unsolvable wavefunctions are both present in the same charge sectors. We thus proceed by separating the solvable and unsolvable

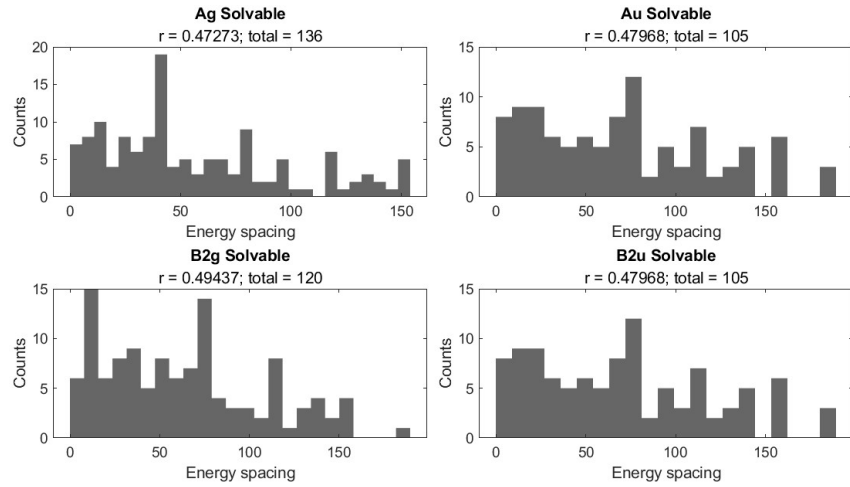


Figure 63: Energy level spacing histograms of wavefunctions of the (1, 2, 3) rectangular prism in the irreps containing solvable wavefunctions after removal of other wavefunctions

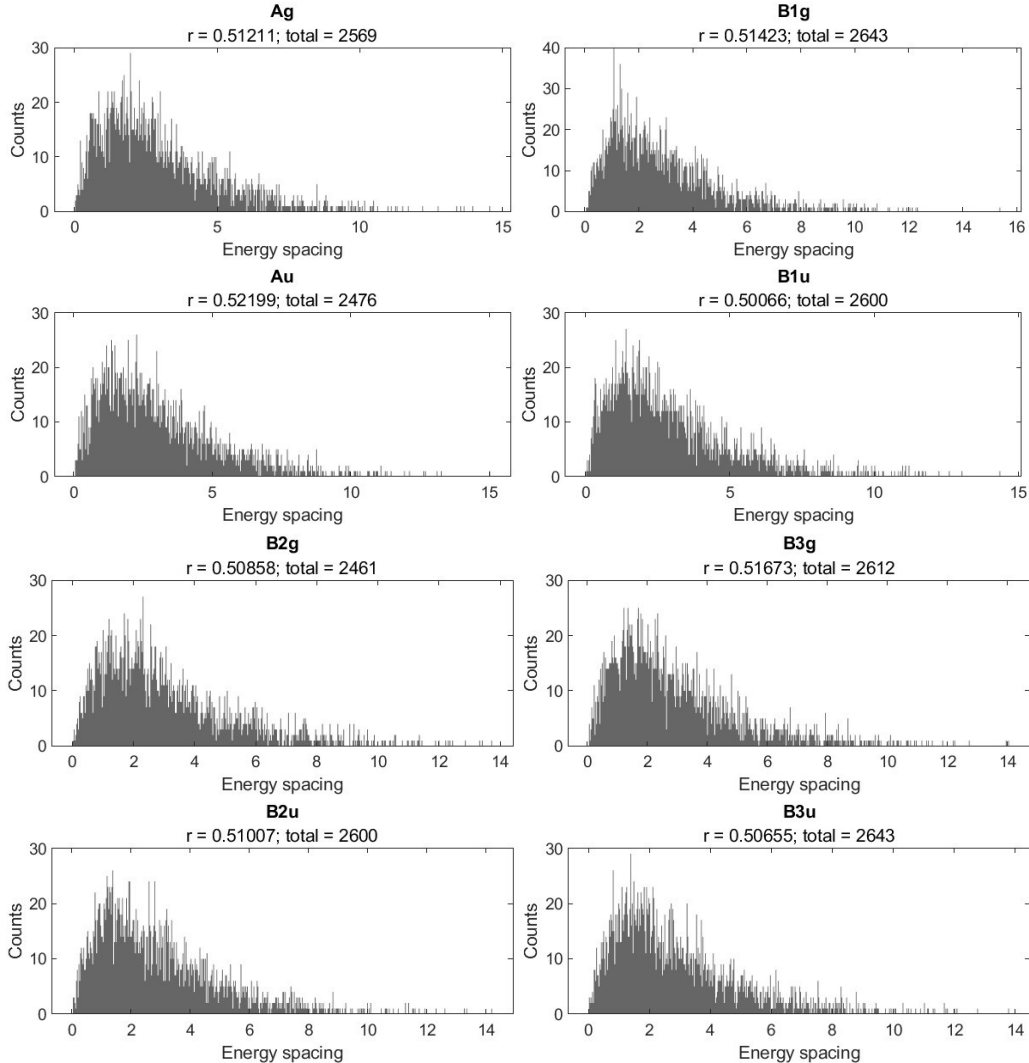


Figure 64: Energy level spacing histograms of wavefunctions of the (1, 2, 3) rectangular prism in all irreps after removal of solvable wavefunctions

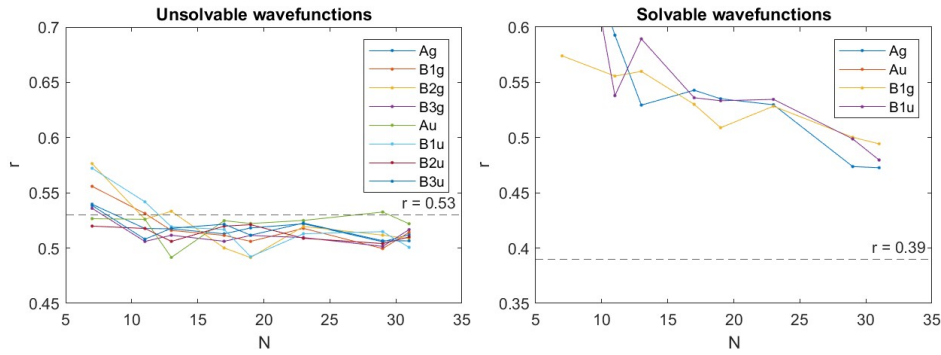


Figure 65: r values as a function of N for the $(1, 2, 3)$ rectangular prism wavefunctions after removal of solvable wavefunctions (left) and for wavefunctions identified as solvable (right)

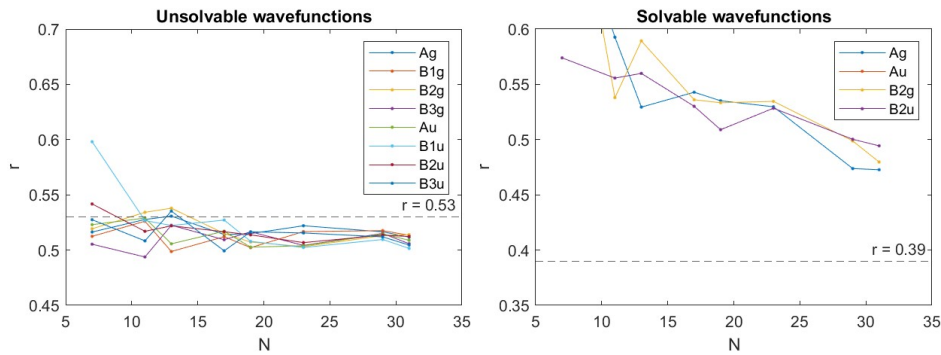


Figure 66: r values as a function of N for the $(1, 2, 4)$ rectangular prism wavefunctions after removal of solvable wavefunctions (left) and for wavefunctions identified as solvable (right)

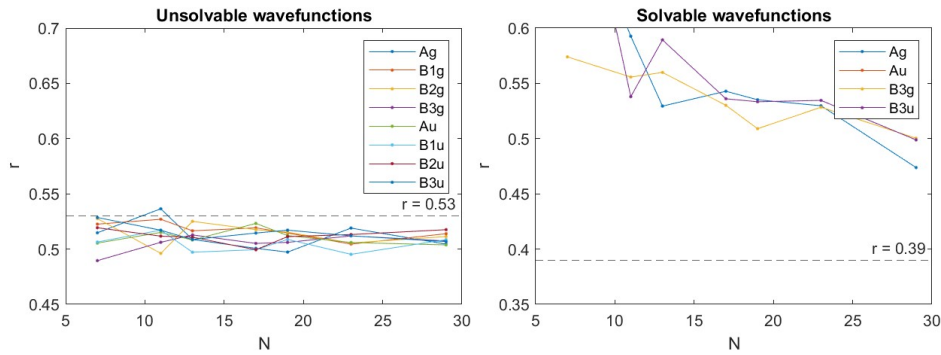


Figure 67: r values as a function of N for the $(1, 3, 4)$ rectangular prism wavefunctions after removal of solvable wavefunctions (left) and for wavefunctions identified as solvable (right)

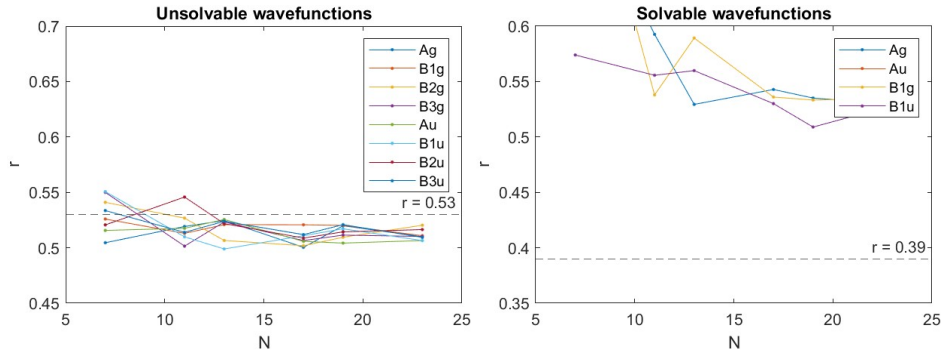


Figure 68: r values as a function of N for the $(2, 3, 4)$ rectangular prism wavefunctions after removal of solvable wavefunctions (left) and for wavefunctions identified as solvable (right)

Superposition	n_1, n_2	l_1	l_2	l_3	$\langle C_2(x) \rangle$	$\langle C_2(y) \rangle$	$\langle \sigma_h(xy) \rangle$	Irrep	Counts
sym	odd	odd	odd	odd	+1	+1	-1	A_u	$(\lfloor \frac{N}{2} \rfloor)$
anti-sym	odd	odd	odd	odd	+1	+1	+1	A_g	$(\lfloor \frac{N}{2} \rfloor)$
sym	odd	odd	odd	even	+1	-1	-1	B_{3g}	$(\lfloor \frac{N}{2} \rfloor)$
anti-sym	odd	odd	odd	even	+1	-1	+1	B_{3u}	$(\lfloor \frac{N}{2} \rfloor)$
sym	odd	odd	even	odd	-1	+1	-1	B_{2g}	$(\lfloor \frac{N}{2} \rfloor)$
anti-sym	odd	odd	even	odd	-1	+1	+1	B_{2u}	$(\lfloor \frac{N}{2} \rfloor)$
sym	odd	even	odd	odd	-1	-1	+1	B_{1g}	$(\lfloor \frac{N}{2} \rfloor)$
anti-sym	odd	even	odd	odd	-1	-1	-1	B_{1u}	$(\lfloor \frac{N}{2} \rfloor)$
sym	odd	odd	even	even	-1	-1	-1	B_{1u}	$(\lfloor \frac{N}{2} \rfloor)$
anti-sym	odd	odd	even	even	-1	-1	+1	B_{1g}	$(\lfloor \frac{N}{2} \rfloor)$
sym	odd	even	odd	even	-1	+1	+1	B_{2u}	$(\lfloor \frac{N}{2} \rfloor)$
anti-sym	odd	even	odd	even	-1	+1	-1	B_{2g}	$(\lfloor \frac{N}{2} \rfloor)$
sym	odd	odd	even	odd	+1	-1	+1	B_{3u}	$(\lfloor \frac{N}{2} \rfloor)$
anti-sym	odd	even	even	odd	+1	-1	-1	B_{3g}	$(\lfloor \frac{N}{2} \rfloor)$
sym	even	any	any	any	+1	+1	+1	A_g	$(\lfloor \frac{N}{2} \rfloor + 1)$
anti-sym	even	any	any	any	+1	+1	-1	A_u	$(\lfloor \frac{N}{2} \rfloor)$

Table 9: Irreps of solvable rectangular prism wavefunctions. We use the following abbreviations: sym = symmetric superposition $\frac{1}{\sqrt{2}}(\psi_{m,n} + \psi_{m,-n})$, and anti-sym = anti-symmetric superposition $\frac{1}{\sqrt{2}}(\psi_{m,n} - \psi_{m,-n})$

D_{2h}	E	$C_2(z)$	$C_2(y)$	$C_2(x)$	i	$\sigma(xy)$	$\sigma(xz)$	$\sigma(yz)$
$A_g + A_u$	+2	+2	+2	+2	0	0	0	0
$B_{1g} + B_{1u}$	+2	+2	-2	-2	0	0	0	0
$B_{2g} + B_{2u}$	+2	-2	+2	-2	0	0	0	0
$B_{3g} + B_{3u}$	+2	-2	-2	+2	0	0	0	0

Table 10: Character table for accidental degeneracies of the rectangular prism

wavefunctions within each charge sector and analyzing the energy level spacings separately. For brevity, we refer to a rectangular prism with relative dimensions $l_1 \times l_2 \times l_3$ as a (l_1, l_2, l_3) square prism. We note that solvable wavefunctions were identified within the predicted irreps in all cases and the proportion of solvable wavefunctions approached the predicted proportions (see Figs. (69) and (70)). The r values generally approached 0.53 as $N \rightarrow \infty$ for all irreps after removal of solvable wavefunctions, and the r values of the solvable wavefunctions approached 0.39 as $N \rightarrow \infty$ as expected (see Figs. (65) through (68)).

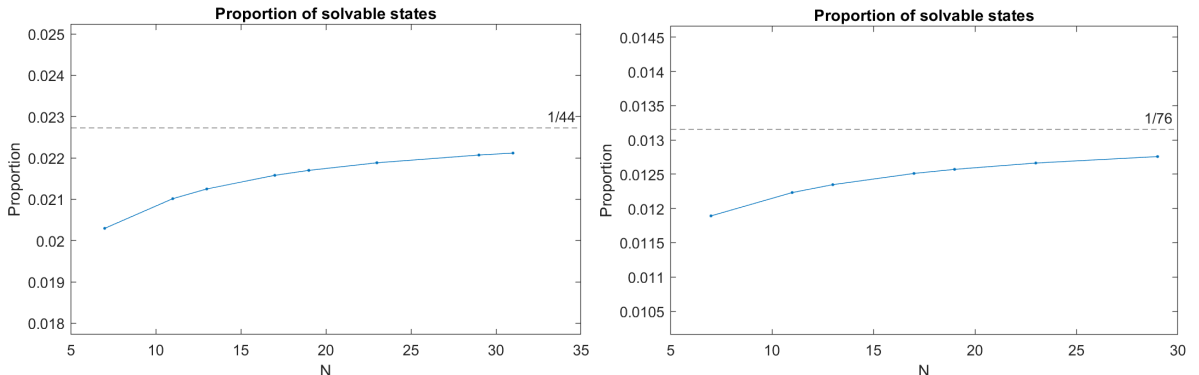


Figure 69: Proportion of wavefunctions identified as solvable for the (1, 2, 3) (left) and (1, 3, 4) (right) rectangular prisms as a function of N . Predicted proportions are indicated by the dashed line.

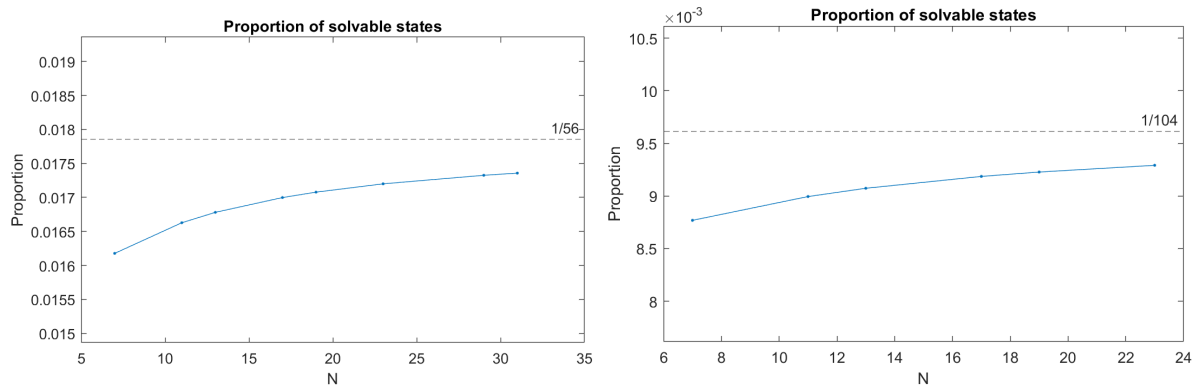


Figure 70: Proportion of wavefunctions identified as solvable for the $(1, 3, 4)$ (left) and $(2, 3, 4)$ (right) rectangular prisms as a function of N . Predicted proportions are indicated by the dashed line.

5 Solvable wavefunctions on the tetrahedron

5.1 Honeycomb lattice

When discretizing the wave functions on the triangle-faced polyhedra, it is most natural to use a lattice which respects the symmetry of the triangular faces. This suggests using either a hexagonal or a honeycomb lattice. We chose to use the honeycomb lattice rather than the hexagonal lattice since the latter cannot be arranged on a triangle-faced polyhedron net without lattice points intersecting the edges and vertices of the polyhedron net. We require lattice points to not intersect edges and vertices of the net since various edges and vertices of the net are identified. Illustrations of the honeycomb lattice on the tetrahedron, octahedron, and octahedron with nearest neighbor hoppings are illustrated in Fig. (71).

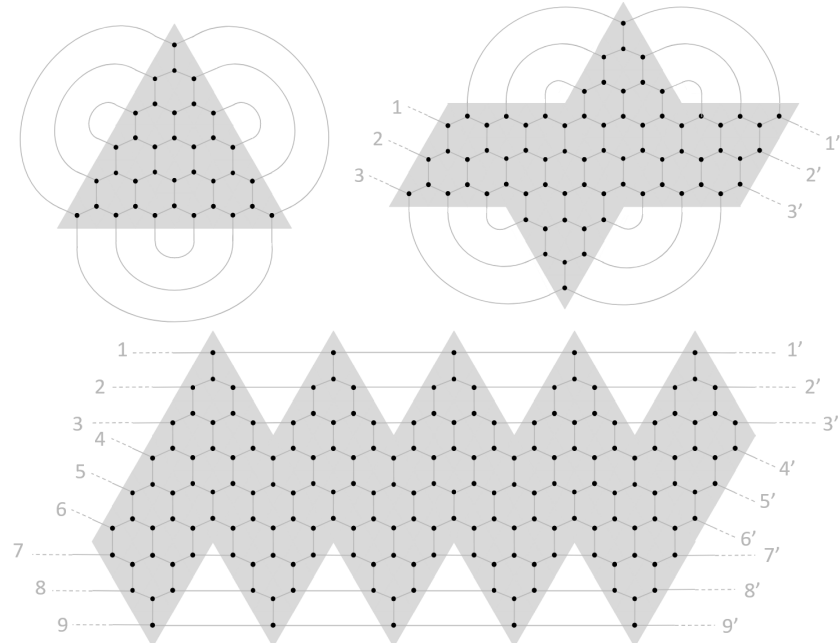


Figure 71: Honeycomb lattice on the tetrahedron, octahedron, and icosahedron nets with nearest neighbor hoppings

5.1.1 Tight-binding Hamiltonian

The honeycomb lattice consists of two sub-lattices which we will denote as A and B . The two sub-lattices can be defined as follows. Let $\vec{R} = \vec{a}_1\mathbb{Z} + \vec{a}_2\mathbb{Z}$ be the lattice of points located precisely at the centers of the honeycombs. Then $\vec{R}_\alpha = \vec{R} + \vec{d}_\alpha$ where $\alpha = A, B$ defines the α sub-lattice.

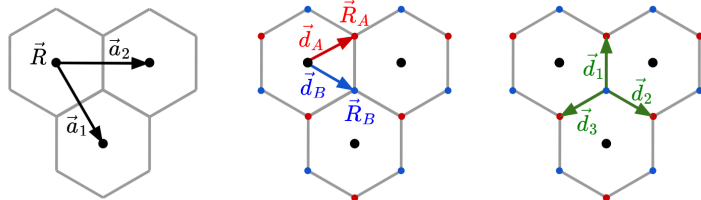


Figure 72: From left to right: illustration of the \vec{R} lattice at the centers of the honeycombs, the A and B sub-lattices, and the nearest neighbor bonds.

Next note that each lattice point in the honeycomb has three nearest neighbors all of which are located in the other sub-lattice. Then the tight-binding Hamiltonian with on-site hopping s and nearest

neighbor hopping $-t$ can be written as

$$H = s \left(\sum_{\alpha=A,B} \sum_{\vec{R}_\alpha} c_{\vec{R}_\alpha}^\dagger c_{\vec{R}_\alpha} \right) - t \left(\sum_{\langle \vec{R}_\alpha, \vec{R}'_\beta \rangle} c_{\vec{R}_\alpha}^\dagger c_{\vec{R}'_\beta} \right)$$

where $\langle \vec{R}_\alpha, \vec{R}'_\beta \rangle$ indicates that the summation is performed over nearest neighbors only. We write the operators in Fourier components as

$$c_{\vec{R}_\alpha}^\dagger = \frac{1}{\sqrt{N}} \sum_{\vec{k}} e^{-i\vec{k}\cdot\vec{R}_\alpha} c_{\vec{k},\alpha}^\dagger,$$

so that the Hamiltonian (ignoring the on-site hopping terms) becomes

$$\begin{aligned} H &= -\frac{t}{N} \sum_{\langle \vec{R}_\alpha, \vec{R}'_\beta \rangle} \sum_{\vec{k}, \vec{k}'} e^{-i(\vec{k}\cdot\vec{R}_\alpha - \vec{k}'\cdot\vec{R}_\beta)} c_{\vec{k},\alpha}^\dagger c_{\vec{k}',\beta} + (\alpha \rightleftharpoons \beta) \\ &= -\frac{t}{N} \sum_{\langle \vec{R}_\alpha, \vec{R}'_\beta \rangle} \sum_{\vec{k}, \vec{k}'} e^{-i(\vec{k}-\vec{k}')\cdot\vec{R}_\alpha} e^{-i\vec{k}'\cdot(\vec{R}_\alpha - \vec{R}_\beta)} c_{\vec{k},\alpha}^\dagger c_{\vec{k}',\beta} + (\alpha \rightleftharpoons \beta) \\ &= -t \sum_{\vec{k}, \vec{k}'} \delta(\vec{k} - \vec{k}') (e^{-i\vec{k}'\cdot\vec{d}_1} + e^{-i\vec{k}'\cdot\vec{d}_2} + e^{-i\vec{k}'\cdot\vec{d}_3}) c_{\vec{k},\alpha}^\dagger c_{\vec{k}',\beta} + (\alpha \rightleftharpoons \beta) \\ &= -t \sum_{\vec{k}} f(\vec{k}) c_{\vec{k},\alpha}^\dagger c_{\vec{k},\beta} - t \sum_{\vec{k}} f^*(\vec{k}) c_{\vec{k},\beta}^\dagger c_{\vec{k},\alpha} \\ &= -t \sum_{\vec{k}} \sum_{\alpha=A,B} \sum_{\beta=A,B} c_{\vec{k},\alpha}^\dagger \mathcal{H}_{\alpha,\beta}(\vec{k}) c_{\vec{k},\beta} \end{aligned}$$

where the bond vectors \vec{d}_i are defined as in Fig. (72), and

$$f(\vec{k}) = e^{-i\vec{k}\cdot\vec{d}_1} + e^{-i\vec{k}\cdot\vec{d}_2} + e^{-i\vec{k}\cdot\vec{d}_3},$$

and $\mathcal{H}_{\alpha,\beta}(\vec{k})$ is a matrix under the α, β indices given by

$$\mathcal{H}(\vec{k}) = \begin{bmatrix} 0 & f(\vec{k}) \\ f^*(\vec{k}) & 0 \end{bmatrix}.$$

The matrix \mathcal{H} has eigenvalues $\pm|f(\vec{k})|$. We can fix

$$\vec{d}_1 = a_0(1, 0), \quad \vec{d}_2 = a_0 \left(-\frac{1}{2}, \frac{\sqrt{3}}{2} \right), \quad \vec{d}_3 = a_0 \left(-\frac{1}{2}, -\frac{\sqrt{3}}{2} \right),$$

and compute $|f(k)|$ explicitly:

$$\begin{aligned} |f(k)| &= |e^{-ia_0k_1} + e^{i(-\frac{1}{2}a_0k_1 + \frac{\sqrt{3}}{2}a_0k_2)} + e^{i(-\frac{1}{2}a_0k_1 - \frac{\sqrt{3}}{2}a_0k_2)}| \\ &= \left| \cos(a_0k_1) - i \sin(a_0k_2) + \left(\cos\left(\frac{a_0k_1}{2}\right) + i \sin\left(\frac{a_0k_1}{2}\right) \right) 2 \cos\left(\frac{\sqrt{3}}{2}a_0k_2\right) \right| \\ &= \sqrt{1 + 4 \cos\left(\frac{3}{2}a_0k_1\right) \cos\left(\frac{\sqrt{3}}{2}a_0k_2\right) + 4 \cos^2\left(\frac{\sqrt{3}}{2}a_0k_2\right)}, \end{aligned}$$

so in the small k^2 limit

$$|f(k)| = 3 - \frac{3}{4}a_0^2 k^2 + \mathcal{O}(k^4).$$

Since we want $E = -s + t|f(k)| \approx -k^2$ in the small k^2 limit we set $t = -\frac{4}{3a_0^2}$ and the on-site hopping $s = -3t = \frac{4}{a_0^2}$. Then we obtain the energies

$$E_{n_1, n_2} = \begin{cases} -\frac{4N^2}{L^2} + \frac{4N^2}{3L^2} \sqrt{1 + 4 \cos\left(\frac{3\pi n_1}{N}\right) \cos\left(\frac{\pi n_2}{N}\right) + 4 \cos^2\left(\frac{\pi n_2}{N}\right)} & \text{tetrahedron} \\ -\frac{4N^2}{L^2} + \frac{4N^2}{3L^2} \sqrt{1 + 4 \cos\left(\frac{\pi n_1}{N}\right) \cos\left(\frac{\pi n_2}{N}\right) + 4 \cos^2\left(\frac{\pi n_2}{N}\right)} & \text{octahedron} \\ -\frac{4N^2}{L^2} + \frac{4N^2}{3L^2} \sqrt{1 + 4 \cos\left(\frac{3\pi n_1}{2N}\right) \cos\left(\frac{\pi n_2}{2N}\right) + 4 \cos^2\left(\frac{\pi n_2}{2N}\right)} & \text{icosahedron} \end{cases}$$

for the various triangle-faced regular polyhedra.

5.2 Symmetries

By labeling the four vertices of the tetrahedron, it can be shown that the symmetries of the tetrahedron have a one-to-one correspondence with the set of permutations of four indices. Thus, the tetrahedron has symmetry group T_d which is isomorphic to the symmetry group on 4 indices. Thus, there are four non-trivial conjugacy classes corresponding to the single permutations, double permutations, 3-cycles, and 4-cycles. In terms of tetrahedron symmetries, these correspond to the σ_d , C_2 , C_3 and S_4 symmetries, respectively.

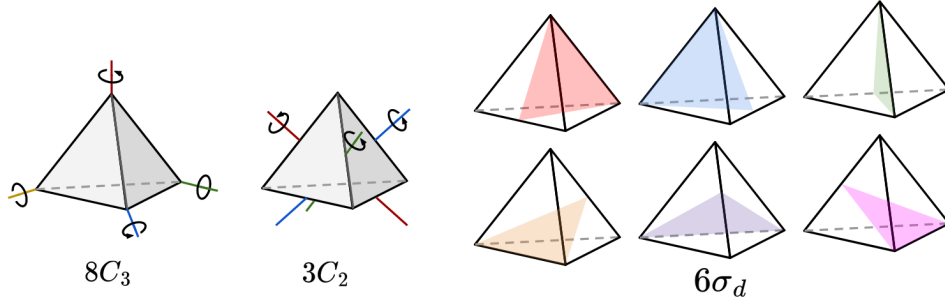


Figure 73: Rotation and reflection symmetries of the tetrahedron

T_d	E	$8C_3$	$3C_2$	$6S_4$	$6\sigma_d$
A_1	+1	+1	+1	+1	+1
A_2	+1	+1	-1	-1	-1
E	+2	-1	+2	0	0
T_1	+3	0	-1	+1	-1
T_2	+3	0	-1	-1	+1

Table 11: Character table for T_d [11]

Based on the character table for T_d , it suffices to compute traces of the symmetries σ_d , C_2 and C_3 to distinguish the irreps and possible accidental degeneracies. Placing the origin at the bottom left vertex of the tetrahedron net, these symmetries can be realized on the net as a reflection about the line $x_1 = L$, a π rotation about $(L, \frac{\sqrt{3}}{2}L)$, and a $\frac{2\pi}{3}$ rotation about $(L, \frac{\sqrt{3}}{2})$ as illustrated in Fig. (74).

5.2.1 Van Hove singularity

For the tetrahedron, there are two Van Hove singularities which occur at energies with $\frac{1}{3}$ and $\frac{2}{3}$ of the maximum energy. The Van Hove singularity occurred at every prime value of N and the degeneracy of both singularities varied exactly linearly with N via the relations $D_{VH}(N) = \frac{3}{2}N - \frac{3}{2}$ for the first

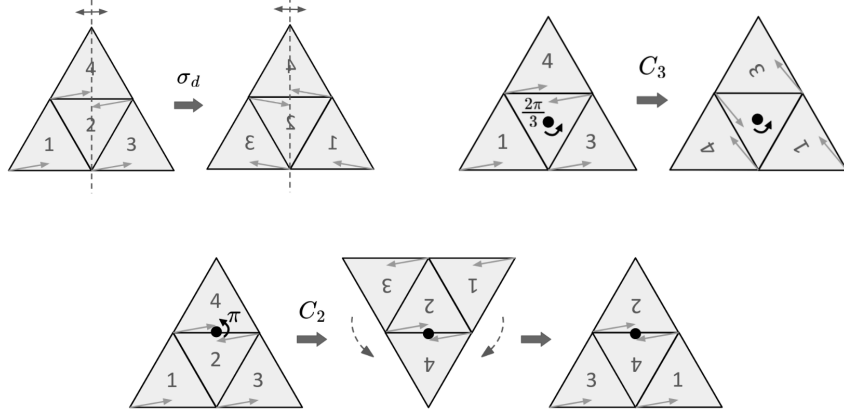


Figure 74: Realization of the σ_d , C_3 , and C_2 symmetries on the tetrahedron net

Van Hove singularity at $\frac{1}{3}$ the maximum energy and via $D_{VH}(N) = \frac{3}{2}N + \frac{3}{2}$ for the second Van Hove singularity at $\frac{2}{3}$ the maximum energy. See Fig. (75).

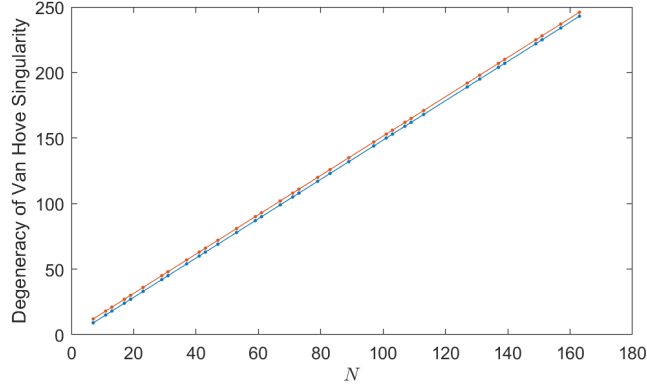


Figure 75: Degeneracy of the Van Hove singularities for the tetrahedron wavefunctions as a function of N

In general, to avoid the Van Hove singularity we only consider the energy level spacing ratios of the energy levels below $\frac{1}{3}$ of the maximum energy. Unfortunately, the Van Hove singularity and the energy cutoff complicates the counting of solvable eigenfunctions within each irrep. Thus, we will not attempt to precisely count the number of solvable wavefunctions in each irrep.

5.3 Completeness of solvable wavefunctions

It was already shown in [6] that the solvable wavefunctions on a tetrahedron are complete via direct computation of the completeness relation. Thus, in this section we provide an additional thermodynamic argument that the solvable wavefunctions are complete and we also demonstrate that the symmetry argument used in the proof of incompleteness of the cube solvable wavefunctions fails in the tetrahedron case.

5.3.1 Proof of completeness via thermodynamics

As before, thermodynamics predicts that the expected number of states with energy below E_0 for a particle confined to an area $A = \sqrt{3}L^2$ in 2 dimensions is

$$N(E) = \frac{\sqrt{3}L^2 E_0}{4\pi}.$$

Next, recall the quantization condition of the wave vector for the tetrahedron wavefunctions

$$\vec{k} = \frac{\pi}{L} \left(m_1, \frac{2m_2 - m_1}{\sqrt{3}} \right)$$

where m_1 and m_2 can be any integers. Then in wave vector space the solvable wave vectors sit in an equilateral triangular grid as illustrated in Fig. (76).

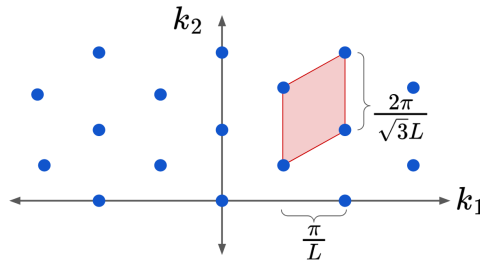


Figure 76: Calculation of the area occupied by each solvable wave vector \vec{k} in wave vector space.

From Fig. (76), it is clear that the area occupied by each \vec{k} is $\frac{2\pi^2}{\sqrt{3}a^2}$. Note that the wave vectors occupy a half circle due to the equivalence of wavefunctions with wave vectors \vec{k} and $-\vec{k}$. Thus, the solvable states with energy less than E_0 occupy a total space of $\frac{\pi E_0}{2}$, so the number of solvable states below energy E_0 can be computed as

$$N_S(E) = \frac{\pi E_0}{2} \cdot \frac{\sqrt{3}L^2}{2\pi^2} = \frac{\sqrt{3}L^2 E_0}{4\pi}$$

in agreement with the expected total number of states. Thus, the solvable wavefunctions are complete.

5.3.2 Failure of symmetry arguments to prove incompleteness

The symmetry group of the tetrahedron, T_d , contains two conjugacy classes of elements of order greater than 2 and hence can potentially have complex eigenvalues: the $8C_3$ rotations and the $6S_4$ improper rotations. We thus should examine the behavior of the solvable tetrahedron wavefunctions under these symmetries. Recall that these wavefunctions are

$$\begin{aligned} \psi_{m,n}(\vec{x}) &= A \cos \left[\frac{\pi}{L} \left((m+n)x_1 + \frac{(m-n)x_2}{\sqrt{3}} \right) \right] \\ &= A \cos \left[\frac{\pi}{L} \left(n_1 x_1 + \frac{n_2 x_2}{\sqrt{3}} \right) \right] \end{aligned}$$

where m and n can be any integers so n_1 and n_2 must be integers of same parity. The C_3 rotations can be implemented on the tetrahedron net as rotations by $\frac{2\pi}{3}$ or $\frac{4\pi}{3}$ about the center of any of the four triangular faces. Placing the origin at the bottom left vertex of the net, the face centers are located at $\vec{x} = (\frac{1}{2}L, \frac{\sqrt{3}}{6}L), (L, \frac{\sqrt{3}}{3}L), (\frac{3}{2}L, \frac{\sqrt{3}}{6}L)$ and $(L, \frac{2\sqrt{3}}{3}L)$. It is straightforward to check that the wavefunctions

$\psi_{m,n}(\vec{x})$ are invariant up to a sign change under the two translations

$$(x_1, x_2) \rightarrow (x_1 + L, x_2)$$

$$(x_1, x_2) \rightarrow (x_1 - \frac{1}{2}L, x_2 + \frac{\sqrt{3}}{2}L)$$

which send the centers of the outer three faces to each other. Thus it suffices to check C_3 rotations about the central face centered at $(L, \frac{\sqrt{3}}{3}L)$ and one outer face, for instance the one centered at $(\frac{1}{2}L, \frac{\sqrt{3}}{6}L)$. It is then straightforward to check that

$$C_3|\psi_{n_1,n_2}\rangle = (-1)^{\frac{n_1+n_2}{2}}|\psi_{\frac{n_1-n_2}{2}, \frac{3n_1+n_2}{n_2}}\rangle$$

$$C_3^2|\psi_{n_1,n_2}\rangle = (-1)^{\frac{3n_1+n_2}{2}}|\psi_{-\frac{n_1+n_2}{2}, \frac{3n_1-n_2}{n_2}}\rangle$$

for C_3 rotations about the center face and

$$C_3|\psi_{n_1,n_2}\rangle = (-1)^{n_1}|\psi_{\frac{n_1-n_2}{2}, \frac{3n_1+n_2}{n_2}}\rangle$$

$$C_3^2|\psi_{n_1,n_2}\rangle = (-1)^{\frac{3n_1-n_2}{2}}|\psi_{-\frac{n_1+n_2}{2}, \frac{3n_1-n_2}{n_2}}\rangle$$

for C_3 rotations about the outer face. Thus, for any C_3 symmetry, we can choose some (n_1, n_2) such that $|\psi_{n_1,n_2}\rangle$ is not an eigenvector of C_3 . It follows that there are no C_3 symmetries such that all of the solvable wavefunctions are eigenfunctions of the symmetry.

The improper symmetries S_4 are implemented by a $\frac{\pi}{2}$ rotation about a C_2 symmetry axis followed by a horizontal reflection through the plane perpendicular to the rotation axis (see Fig. (77)).

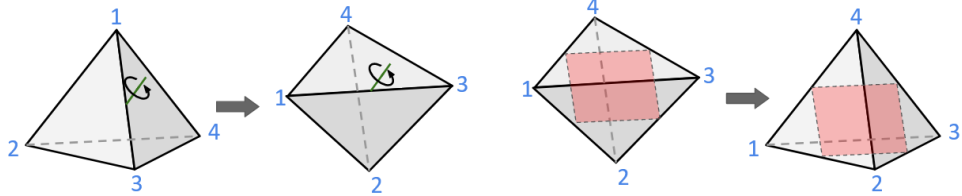


Figure 77: Illustration of a S_4 symmetry of the tetrahedron

The realization of the S_4 symmetry on the tetrahedron net can be most easily visualized by labeling the vertices and permuting them in a four cycle (see Fig. (78)). By examining the triangle with vertices 1, 2, 3 it is clear that the transformation is a reflection about the line $x_2 = \cos \frac{2\pi}{3}x_1 + \frac{L}{2}$ followed by a translation $x_1 \rightarrow x_1 + L$. Similarly as in the C_3 symmetries, one can check that there exist solvable wavefunctions which are not eigenfunctions of any of the S_4 symmetries.

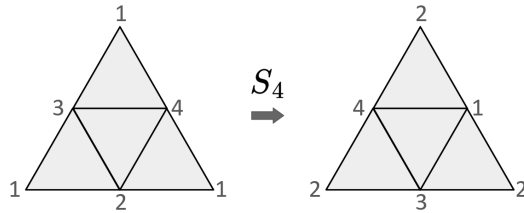


Figure 78: Realization of the S_4 symmetry of the tetrahedron net

5.4 Irreps of the solvable wavefunctions

In this section, we classify all of the solvable wavefunctions on the tetrahedron into irreps of the T_d symmetry group. First, note that when numerically computing the wavefunctions we can simultaneously diagonalize H , σ_d and $C_3 + C_3^{-1}$ since all three operators commute with each other. Thus, all computed wavefunctions are eigenfunctions of H , σ_d and $C_3 + C_3^{-1}$.

By following the same procedures as before, one can verify that

$$\begin{aligned}\sigma_d |\psi_{n_1, n_2}\rangle &= |\psi_{-n_1, n_2}\rangle \\ C_3 |\psi_{n_1, n_2}\rangle &= (-1)^{\frac{n_1+n_2}{2}} |\psi_{\frac{n_1-n_2}{2}, \frac{3n_1+n_2}{2}}\rangle \\ C_2 |\psi_{n_1, n_2}\rangle &= (-1)^{n_2} |\psi_{n_1, n_2}\rangle.\end{aligned}$$

We first consider solvable wavefunctions of the form $|\psi_{0, n_2}\rangle$ where n_2 must be even. It follows that $|\psi_{0, n_2}\rangle$ is an eigenvector of both σ_d and C_2 with eigenvalues both 1. Under the C_3 rotation, $|\psi_{0, n_2}\rangle$ is triply degenerate so we may write the wavefunctions $|\psi\rangle$ in the degenerate energy level in the form

$$\begin{aligned}|\psi\rangle &= c_1 |\psi_{0, n_2}\rangle + c_2 C_3 |\psi_{0, n_2}\rangle + c_3 C_3^2 |\psi_{0, n_2}\rangle \\ &= \begin{cases} c_1 |\psi_{0, n_2}\rangle + c_2 |\psi_{-\frac{n_2}{2}, \frac{n_2}{2}}\rangle + c_3 |\psi_{\frac{n_2}{2}, \frac{n_2}{2}}\rangle & \frac{n_2}{2} \text{ even} \\ c_1 |\psi_{0, n_2}\rangle - c_2 |\psi_{-\frac{n_2}{2}, \frac{n_2}{2}}\rangle - c_3 |\psi_{\frac{n_2}{2}, \frac{n_2}{2}}\rangle & \frac{n_2}{2} \text{ odd} \end{cases}\end{aligned}$$

for some constants $c_i \in \mathbb{C}$. We first consider the case where $\frac{n_2}{2}$ is even. Then $|\psi\rangle$ clearly is always an eigenvector of C_2 with eigenvalue 1 so the T_1 and T_2 irreps can be eliminated. Then, note that if $c_1 \neq 0$ then $|\psi\rangle$ is an eigenfunction of σ_d with eigenvalue 1 then we can set $c_2 = c_3$. Alternatively, if $c_1 = 0$ then we either must have $c_2 = c_3$ (so $|\psi\rangle$ has σ_d eigenvalue 1) or $c_2 = -c_3$ (so $|\psi\rangle$ has σ_d eigenvalue -1). Lastly, since $|\psi\rangle$ is an eigenvector of $C_3 + C_3^{-1}$ then we must have

$$\begin{cases} \frac{c_1+c_2}{c_3} = \frac{c_2+c_3}{c_1} = \frac{c_1+c_3}{c_2} & c_1 \neq 0 \\ c_2 = \pm c_3 & c_1 = 0 \end{cases}$$

These conditions together with the normalization condition have a convenient linearly independent set of solutions

$$(c_1, c_2, c_3) = \left(\frac{1}{\sqrt{3}}, \frac{1}{\sqrt{3}}, \frac{1}{\sqrt{3}} \right), \left(0, \frac{1}{\sqrt{2}}, \frac{1}{\sqrt{2}} \right), \left(0, -\frac{1}{\sqrt{2}}, \frac{1}{\sqrt{2}} \right).$$

It is then clear that the $(c_1, c_2, c_3) = (\frac{1}{\sqrt{3}}, \frac{1}{\sqrt{3}}, \frac{1}{\sqrt{3}})$ solution corresponds to an eigenvector in the A_1 irrep and the remaining two solutions correspond to eigenvectors in the E irrep (note that both eigenvectors are not eigenvectors of C_3 , eliminating A_1 and A_2).

Next consider the case where $\frac{n_2}{2}$ is odd. Then if $c_1 \neq 0$ then $|\psi\rangle$ can only be an eigenvector of σ_d if $c_2 = c_3 = 0$. However, the wavefunction $|\psi\rangle = |\psi_{0, n_2}\rangle$ is not an eigenvector of C_3 so the wavefunction cannot be in one of the one-dimensional irreps. If $c_1 = 0$ then $|\psi\rangle$ must be an eigenvector of C^2 with eigenvalue -1. This again eliminates the one-dimensional irreps A_1 and A_2 . Thus, no wave functions in the degenerate energy level can be contained in the one dimensional irreps, and as a result, no wave functions in the degenerate energy level can be contained in the two dimensional irrep E since the energy level is triply degenerate.

Thus, the wave vectors must be contained in one of the three-dimensional irreps T_1 or T_2 . We

recently argued that if $c_1 \neq 0$ then we must have $c_2 = c_3 = 0$, so $\langle \psi | \sigma_d | \psi \rangle = 1$. Moreover, if $c_1 = 0$ then $|\psi\rangle$ can only be an eigenvector of σ_d if $c_2 = c_3$ (so $\langle \psi | \sigma_d | \psi \rangle = 1$) or if $c_2 = -c_3$ (so $\langle \psi | \sigma_d | \psi \rangle = -1$). Thus we obtain the convenient set of linearly independent solutions

$$(c_1, c_2, c_3) = (1, 0, 0), \left(0, \frac{1}{\sqrt{2}}, \frac{1}{\sqrt{2}}\right), \left(0, -\frac{1}{\sqrt{2}}, \frac{1}{\sqrt{2}}\right),$$

and it is clear that the energy level is contained in the T_2 irrep.

Next consider wavefunctions of the form $|\psi_{n_1,0}\rangle$ where n_1 must be even. Using a highly analogous argument as in the previous case, one can similarly show that the triple degenerate energy level containing $|\psi_{n_1,0}\rangle$ consists of a E and A_1 irrep if $\frac{n_1}{2}$ is even and comprises a T_2 irrep if $\frac{n_1}{2}$ is odd.

The remaining wavefunctions to consider are the wavefunctions of the form $|\psi_{n_1,n_2}\rangle$ such that none of the wavefunctions $|\psi_{n_1,n_2}\rangle$, $C_3|\psi_{n_1,n_2}\rangle$ and $C_3^2|\psi_{n_1,n_2}\rangle$ have vectors parallel to the x_1 or x_2 axes. Equivalently, $n_1, n_2, n_1 - n_2, n_1 + n_2$ are all non-zero. In this case, the symmetries of the tetrahedron predict a six-fold degenerate state which can be written in the form

$$\begin{aligned} |\psi\rangle &= c_1|\psi_{n_1,n_2}\rangle + c_2C_3|\psi_{n_1,n_2}\rangle + c_3C_3^2|\psi_{n_1,n_2}\rangle + c_4\sigma_d|\psi_{n_1,n_2}\rangle + c_5\sigma_dC_3|\psi_{n_1,n_2}\rangle + c_6\sigma_dC_3^2|\psi_{n_1,n_2}\rangle \\ &= c_1|\psi_{n_1,n_2}\rangle + c_2(-1)^{\frac{n_1+n_2}{2}}|\psi_{\frac{n_1-n_2}{2}, \frac{3n_1+n_2}{2}}\rangle + c_3(-1)^{n_1}|\psi_{-\frac{n_1+n_2}{2}, \frac{3n_1-n_2}{2}}\rangle \\ &\quad + c_4|\psi_{-n_1,n_2}\rangle + c_2(-1)^{\frac{n_1+n_2}{2}}|\psi_{\frac{n_2-n_1}{2}, \frac{3n_1+n_2}{2}}\rangle + c_3(-1)^{n_1}|\psi_{\frac{n_1+n_2}{2}, \frac{3n_1-n_2}{2}}\rangle \end{aligned}$$

Since $|\psi\rangle$ must be an eigenvector of σ_d then we can require that $(c_1, c_2, c_3) = \pm(c_4, c_5, c_6)$. Then the wavefunction becomes

$$\begin{aligned} |\psi\rangle &= c_1(|\psi_{n_1,n_2}\rangle \pm |\psi_{-n_1,n_2}\rangle) + c_2(-1)^{\frac{n_1+n_2}{2}}(|\psi_{\frac{n_1-n_2}{2}, \frac{3n_1+n_2}{2}}\rangle \pm |\psi_{\frac{n_2-n_1}{2}, \frac{3n_1+n_2}{2}}\rangle) \\ &\quad + c_3(-1)^{n_1}(|\psi_{-\frac{n_1+n_2}{2}, \frac{3n_1-n_2}{2}}\rangle \pm |\psi_{\frac{n_1+n_2}{2}, \frac{3n_1-n_2}{2}}\rangle) \end{aligned}$$

We next consider the possible parities of n_1 and n_2 . If n_1 and n_2 are both odd then $\frac{n_1-n_2}{2}$ and $\frac{n_1+n_2}{2}$ must have differing parity since their difference is odd. If n_1 and n_2 are even then $\frac{n_1-n_2}{2}$ and $\frac{n_1+n_2}{2}$ must have same parity since their difference is even. Thus we effectively have two cases: $(n_1, n_2), (\frac{n_1-n_2}{2}, \frac{3n_1+n_2}{2}), (-\frac{n_1+n_2}{2}, \frac{3n_1-n_2}{2})$ must be three pairs of even numbers and if not, they are two pairs of odd numbers and one pair of even numbers.

First consider the case where all three pairs consist of even numbers. The wavefunction then becomes

$$\begin{aligned} |\psi\rangle &= c_1(|\psi_{n_1,n_2}\rangle \pm |\psi_{-n_1,n_2}\rangle) + c_2(|\psi_{\frac{n_1-n_2}{2}, \frac{3n_1+n_2}{2}}\rangle \pm |\psi_{\frac{n_2-n_1}{2}, \frac{3n_1+n_2}{2}}\rangle) \\ &\quad + c_3(|\psi_{-\frac{n_1+n_2}{2}, \frac{3n_1-n_2}{2}}\rangle \pm |\psi_{\frac{n_1+n_2}{2}, \frac{3n_1-n_2}{2}}\rangle) \end{aligned}$$

We first note that $|\psi\rangle$ is an eigenvector of C_3 if and only if $c_1 = c_2 = c_3$. In particular, by setting $c_1 = c_2 = c_3 = \frac{1}{\sqrt{3}}$ it is apparent that the resulting state is an eigenvector of C_3 and C_2 with eigenvalues 1 and an eigenvector of σ_d with eigenvalue ± 1 . Thus the six-fold degenerate energy level must contain a wavefunction in the A_1 irrep and a wavefunction in the A_2 irrep and the wavefunctions spanning the remaining dimensions of the degenerate space must consist of irreps with dimension higher than one. Since the remaining space is four dimensional, it must be spanned by the two degenerate spaces contained in the E irrep.

Lastly, we consider the case where one pair of $(n_1, n_2), (\frac{n_1-n_2}{2}, \frac{3n_1+n_2}{2})$ and $(-\frac{n_1+n_2}{2}, \frac{3n_1-n_2}{2})$ is even and the other two pairs are odd. Without loss of generality, we can assume that (n_1, n_2) is the even

pair while the remaining pairs are odd. Then the wavefunction becomes

$$|\psi\rangle = c_1(|\psi_{n_1, n_2}\rangle \pm |\psi_{-n_1, n_2}\rangle) - c_2(|\psi_{\frac{n_1-n_2}{2}, \frac{3n_1+n_2}{2}}\rangle \pm |\psi_{\frac{n_2-n_1}{2}, \frac{3n_1+n_2}{2}}\rangle) + c_3(|\psi_{-\frac{n_1+n_2}{2}, \frac{3n_1-n_2}{2}}\rangle \pm |\psi_{\frac{n_1+n_2}{2}, \frac{3n_1-n_2}{2}}\rangle)$$

First note that if $|\psi\rangle$ is an eigenvector of C_2 then we must have either $c_1 = 0$ or $c_2 = c_3 = 0$. In either case, it follows that $|\psi\rangle$ can no longer be an eigenvector of C_3 . Thus the degenerate energy level does not contain wavefunctions in any one-dimensional irreps. Since the space is six dimensional then it must contain either three sets of the two-dimensional irrep E or no wavefunctions in the irrep E .

If the energy level consisted entirely of E irreps then all wavefunctions would have to be eigenfunctions of C_2 with eigenvalue 1. However, it is clear that any wavefunction with $c_1 = 0$ and $c_2 = c_3$ is an eigenfunction of C_2 with eigenvalue -1 . Thus, the degenerate energy level must consist entirely of three-dimensional irreps.

Lastly, we note that for any choice of (c_1, c_2, c_3) the choice of having only $+$ signs gives an eigenfunction of σ_d with eigenvalue 1 and the choice of having only $-$ signs gives a linearly independent eigenfunction of σ_d with eigenvalue -1 . It follows that the energy level must consist of one three-dimensional subspace in the irrep T_1 and one three-dimensional subspace in the irrep T_2 .

The last remaining case is $\psi_{0,0}$ which the constant ground state which must be in irrep A_1 since it is an eigenvector of all the symmetry operations with eigenvalue 1. The results from this section are summarized in the table below.

n_1	n_2	$\frac{n_2}{2}$	$\frac{n_1-n_2}{2}$	$\frac{3n_1+n_2}{2}$	$\frac{n_1+n_2}{2}$	$\frac{3n_1-n_2}{2}$	Irrep
0	0	-	-	-	-	-	A_1
0	even	even	-	-	-	-	$A_1 + E$
0	even	odd	-	-	-	-	T_2
even	0	even	-	-	-	-	$A_1 + E$
even	0	odd	-	-	-	-	T_2
even	even	-	even	even	even	even	$2E + A_1 + A_2$
even	even	-	odd	odd	odd	odd	$T_1 + T_2$
odd	odd	-	even	even	odd	odd	$T_1 + T_2$
odd	odd	-	odd	odd	even	even	$T_1 + T_2$

Table 12: Irreps of the solvable tetrahedron wavefunctions. For brevity, the indication “even” in the table is short for even and non-zero.

T_d	E	$8C_3$	$3C_2$	$6S_4$	$6\sigma_d$
$E + A_1$	+3	0	+3	+1	+1
$T_1 + T_2$	+6	0	-2	0	0
$2E + A_1 + A_2$	+4	0	+4	0	0

Table 13: Character table for accidental degeneracies of the tetrahedron

5.5 Energy level statistics

The energy level spacings and level spacing ratios of the tetrahedron wavefunctions within each charge sector are shown in Figs. below. Note that the energy spacing distributions are largely Poisson as expected. The LSR values also approach 0.39 as $N \rightarrow \infty$, indicating that deviations are likely due to finite system size.

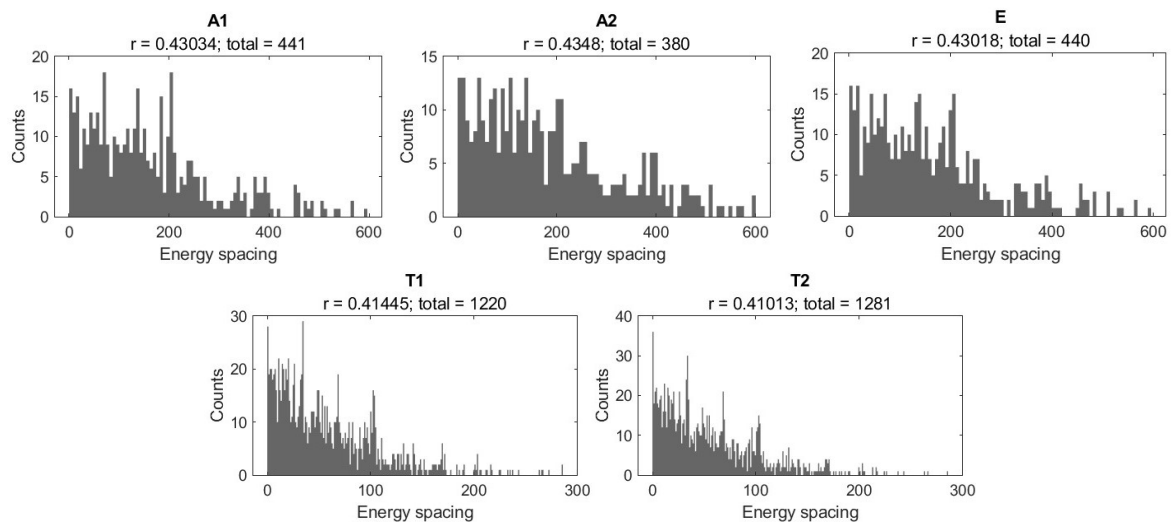


Figure 79: Energy-level spacing histograms of the tetrahedron wavefunctions for $N = 163$.

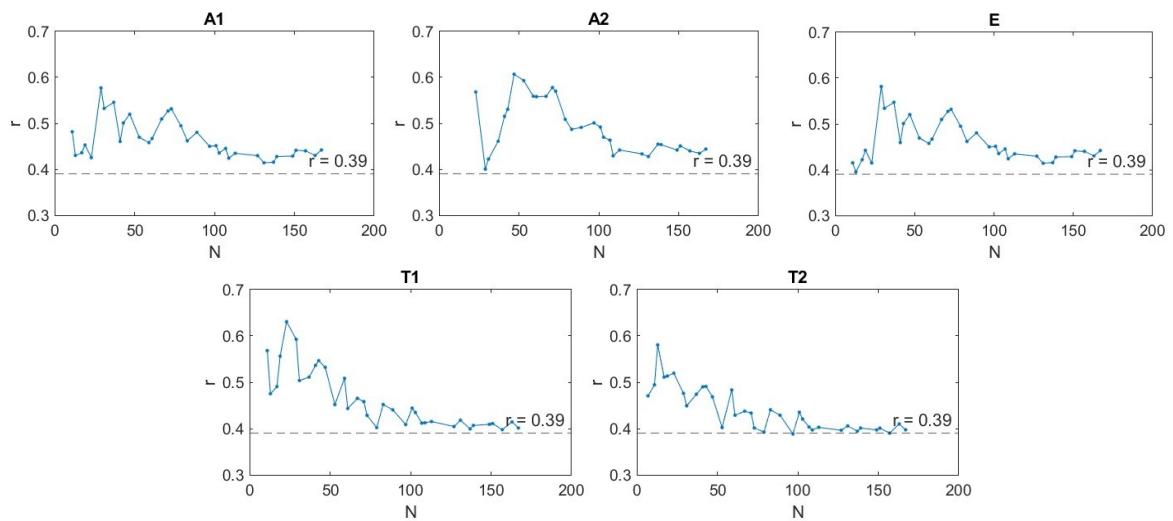


Figure 80: LSR plots for each charge sector of the tetrahedron as a function of N

6 Unsolvable wavefunctions on the octahedron

6.1 Incompleteness of the solvable wavefunctions

6.1.1 Proof via thermodynamics

The expected number of states with energy below E_0 for a particle confined to an area composed of 8 triangular faces spanned by the lattice vectors $\vec{a}_1 = (L, 0)$ and $\vec{a}_2 = (\frac{L}{2}, \frac{\sqrt{3}L}{2})$ is

$$N(E) = \frac{\pi E}{(2\pi)^2} \cdot 8 \cdot \frac{|\vec{a}_1 \times \vec{a}_2|}{2} = \frac{E|\vec{a}_1 \times \vec{a}_2|}{\pi}.$$

Next, recall the quantization condition of the wave vector for the tetrahedron wavefunctions

$$\vec{k} = \frac{2\pi}{L} \left(\frac{n_1}{3}, \frac{n_2}{\sqrt{3}} \right) = m_1 \vec{b}_1 + m_2 \vec{b}_2$$

where $\vec{b}_1 = \frac{2\pi}{L}(1, -\frac{1}{\sqrt{3}})$ and $\vec{b}_2 = \frac{2\pi}{L}(0, \frac{2}{\sqrt{3}})$ are the reciprocal vectors of the lattice vectors and m_1 and m_2 are any integers so that n_1 and n_2 are integers of same parity. Thus each wave vector \vec{k} in momentum space occupies an area

$$A_k = \frac{1}{2} \cdot \frac{1}{3} |\vec{b}_1 \times \vec{b}_2| = \frac{(2\pi)^2}{6|\vec{a}_1 \times \vec{a}_2|} = \frac{2\pi^2}{3|\vec{a}_1 \times \vec{a}_2|}$$

where the factor of $\frac{1}{2}$ accounts for both the sine and cosine wavefunctions for each \vec{k} and the observation that three wave vectors are contained in each lattice unit cell. Then since the wave functions are invariant under rotations of the wave vector by $\frac{\pi}{3}$ then the expected number of solvable wavefunctions is

$$N_s(E) = \frac{\pi E}{6A_k} = \frac{E|\vec{a}_1 \times \vec{a}_2|}{4\pi}.$$

Thus, it is clear that

$$\frac{N_s(E)}{N(E)} = \frac{1}{4},$$

so the solvable wavefunctions are incomplete and comprise only $\frac{1}{4}$ the complete set of solvable wavefunctions.

6.1.2 Proof of incompleteness via symmetry

The octahedron has a C_3 rotation symmetry. Which corresponds to a $\frac{2\pi}{3}$ rotation about the origin of the wavefunctions. The solvable wavefunctions are all invariant under $\frac{\pi}{3}$ rotations about the origin, so the solvable wavefunctions are all eigenfunctions of C_3 with eigenvalue 1. Thus, it is impossible to eigenfunctions of C_3 with eigenvalues at the complex cube roots of unity using only solvable wavefunctions, indicating that they are incomplete.

6.2 Symmetries of the octahedron

The symmetries of the octahedron are in one-to-one correspondence with the symmetries of the cube by inscribing the octahedron within the cube as illustrated in Fig (82). As such, the octahedron is known as the dual polyhedron of the cube. It follows that the symmetry group of the octahedron is O_h , the same as for the cube. The rotation and reflection symmetries of the octahedron are illustrated in Figs. (81) and (82), respectively.

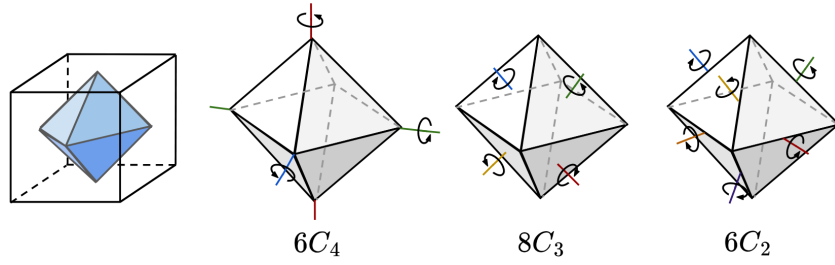


Figure 81: Left: illustration of the octahedron as the dual polyhedron of the cube. Right: rotation symmetries of the octahedron.

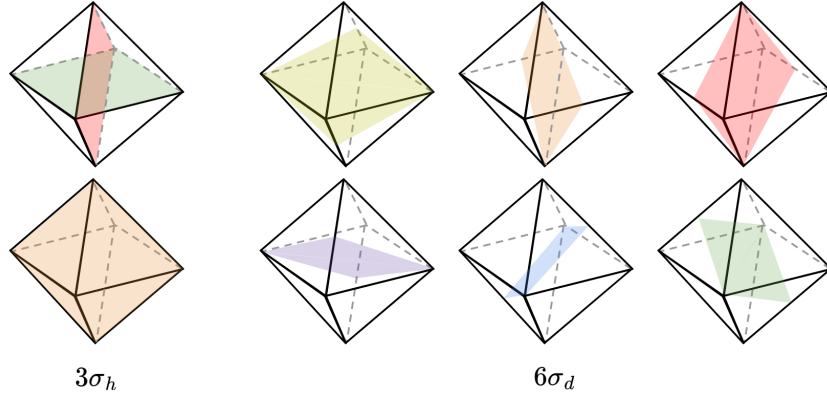


Figure 82: Reflection symmetries of the octahedron

6.2.1 Irreps of the solvable wavefunctions

To distinguish the irreps of the octahedron solvable wavefunctions it will suffice to consider the symmetries C_2 , C_3 , σ_d and i which can be implemented on the octahedron net by a π rotation about $(\frac{L}{4}, \frac{\sqrt{3}L}{4})$, a $\frac{2\pi}{3}$ rotation about $(0, \frac{\sqrt{3}L}{4})$, a reflection about $x_1 = 0$, and successive reflections about the lines $x_1 = 0$, $x_1 = L$ and $x_2 = \frac{\sqrt{3}L}{2}$, respectively.

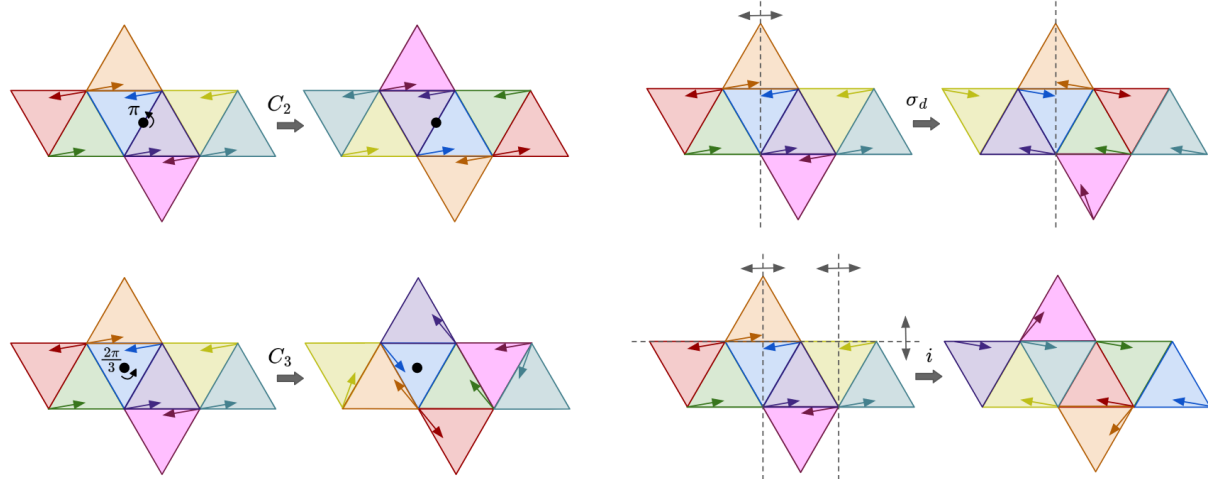


Figure 83: Implementation of the C_2 , C_3 , σ_d and i symmetries of the octahedron on the octahedron net

Using the usual method, it is straightforward to verify that

$$\begin{aligned} C_2|\psi_{n_1,n_2}^{(\square)}\rangle &= \begin{cases} |\psi_{n_1,n_2}^{(c)}\rangle & \square = c \\ -|\psi_{n_1,n_2}^{(s)}\rangle & \square = s \end{cases} \\ C_3|\psi_{n_1,n_2}^{(\square)}\rangle &= |\psi_{n_1,n_2}^{(\square)}\rangle \quad \text{if } 3|n_1 \\ (C_4)^2|\psi_{n_1,n_2}^{(\square)}\rangle &= |\psi_{n_1,n_2}^{(\square)}\rangle \\ \sigma_d|\psi_{n_1,n_2}^{(\square)}\rangle &= |\psi_{-n_1,n_2}^{(\square)}\rangle \\ \sigma_h|\psi_{n_1,n_2}^{(\square)}\rangle &= |\psi_{n_1,-n_2}^{(\square)}\rangle. \end{aligned}$$

where $\square = c$ or s . We first consider the case where $n_1 = 0$ and n_2 is even and non-zero. It then follows that the degenerate wavefunctions $|\psi_{n_1,n_2}^{(c)}\rangle$ and $|\psi_{n_1,n_2}^{(s)}\rangle$ are eigenfunctions of C_3 , each with eigenvalue +1 indicating that the wavefunctions must be contained in one-dimensional irreps. Further, they are eigenfunctions of σ_d with eigenvalue +1 leaving only A_{1g} and A_{2u} as possible candidates. Noting that $|\psi_{n_1,n_2}^{(c)}\rangle$ and $|\psi_{n_1,n_2}^{(s)}\rangle$ are eigenfunctions of C_2 with eigenvalue +1 and -1, respectively, it follows that $|\psi_{n_1,n_2}^{(c)}\rangle$ is contained in the A_{1g} irrep and $|\psi_{n_1,n_2}^{(s)}\rangle$ is contained in the A_{2u} irrep. Thus, there is an accidental degeneracy between A_{1g} and A_{2u} wavefunctions.

Similarly, in the case where $n_2 = 0$ and n_1 is even, non-zero, and divisible by 3, then the degenerate wavefunctions $|\psi_{n_1,n_2}^{(c)}\rangle$ and $|\psi_{n_1,n_2}^{(s)}\rangle$ must be contained in one-dimensional irreps since they are eigenfunctions of C_3 with eigenvalue +1. Next, we note that $\sigma_d|\psi_{n_1,0}^{(c)}\rangle = |\psi_{-n_1,0}^{(c)}\rangle = |\psi_{n_1,0}^{(c)}\rangle$ and $C_2|\psi_{n_1,0}^{(c)}\rangle = |\psi_{n_1,0}^{(c)}\rangle$ indicating that $|\psi_{n_1,0}^{(c)}\rangle$ must be contained in A_{1g} . Meanwhile, $\sigma_d|\psi_{n_1,0}^{(s)}\rangle = |\psi_{-n_1,0}^{(s)}\rangle = -|\psi_{n_1,0}^{(s)}\rangle$ and $C_2|\psi_{n_1,0}^{(s)}\rangle = -|\psi_{n_1,0}^{(s)}\rangle$ indicating that $|\psi_{n_1,0}^{(s)}\rangle$ is contained in A_{2g} . This results in another accidental degeneracy $A_{1g} + A_{2g}$.

Next we consider the case where n_1 and n_2 are non-zero and $3|n_1$. We then have a four-fold degenerate energy level spanned by $|\psi_{\pm n_1,n_2}^{(c)}\rangle$ and $|\psi_{\pm n_1,n_2}^{(s)}\rangle$. Since all of the wavefunctions are eigenfunctions of C_3 with eigenvalue +1 then they must be contained in one-dimensional irreps. In particular, we note that

$$\frac{1}{\sqrt{2}}(|\psi_{n_1,n_2}^{(c)}\rangle \pm |\psi_{-n_1,n_2}^{(c)}\rangle)$$

is an eigenvector of C_2 and σ_d with eigenvalues +1 and ± 1 , respectively, indicating that the symmetric superposition of cosine wavefunctions is contained in A_{1g} while the anti-symmetric superposition of cosine wavefunctions is contained in A_{1u} . Similarly,

$$\frac{1}{\sqrt{2}}(|\psi_{n_1,n_2}^{(s)}\rangle \pm |\psi_{-n_1,n_2}^{(s)}\rangle)$$

is an eigenvector of C_2 and σ_d with eigenvalues -1 and ± 1 , respectively, indicating that the symmetric superposition of sine wavefunctions is contained in A_{2u} while the anti-symmetric superposition of cosine wavefunctions is contained in A_{2g} . Thus, there is a four-fold accidental degeneracy $A_{1g} + A_{1u} + A_{2g} + A_{2u}$ for n_1 and n_2 non-zero and $3|n_1$.

We next consider the cases when $n_1 \nmid 3$. Suppose first that $n_2 = 0$. Then there is a two-fold degeneracy between $|\psi_{n_1,0}^{(c)}\rangle$ and $|\psi_{n_1,0}^{(s)}\rangle$. We first note that both are eigenfunctions of σ_d with eigenvalues +1 and -1, respectively, yet they also are not eigenfunctions of C_3 . Thus, the wavefunctions cannot belong to one-dimensional irreps. Furthermore, we note that both wavefunctions are eigenfunctions of $(C_4)^2$ with eigenvalue +1 so they cannot belong to three-dimensional irreps. Lastly, since both wavefunctions are eigenfunctions of σ_h with eigenvalue +1 they must belong to the E_g irrep.

The next case to consider is when $n_1 \nmid 3$ and $n_2 \neq 0$. Then we have a four-fold degeneracy spanned by $\frac{1}{\sqrt{2}}(|\psi_{n_1,n_2}^{(c)}\rangle \pm |\psi_{n_1,-n_2}^{(c)}\rangle)$ and $\frac{1}{\sqrt{2}}(|\psi_{n_1,n_2}^{(s)}\rangle \pm |\psi_{n_1,-n_2}^{(s)}\rangle)$ are eigenfunctions of C_2 and σ_h with distinct eigenvalues but are not eigenvectors of C_3 . Thus the wavefunctions cannot be contained in one-dimensional irreps. Again since all four wavefunctions are eigenfunctions of $(C_4)^2$ with eigenvalue +1 then they cannot be contained in a three-dimensional irrep. Lastly note that the symmetric superpositions are eigenfunctions of σ_h with eigenvalue +1 while the anti-symmetric superpositions have eigenvalue -1. Thus the eigenfunctions must be contained in the E_u and E_g irreps.

The last case to consider is the trivial case where $n_1 = n_2 = 0$. Then the wavefunction is a constant and is thus an eigenfunction of all symmetries with eigenvalue +1 so the wavefunction belongs in A_{1g} . The results in this section are summarized in Table (14).

n_1	n_2	Irrep
0	0	A_1
0	even	$A_{1g} + A_{2u}$
even, $3 n_1$	0	$A_{1g} + A_{2g}$
even, $3 n_1$	even	$A_{1g} + A_{2g} + A_{1u} + A_{2u}$
odd, $3 n_1$	odd	$A_{1g} + A_{2g} + A_{1u} + A_{2u}$
even, $3 \nmid n_1$	0	E_g
even, $3 \nmid n_1$	even	$E_g + E_u$
odd, $3 \nmid n_1$	odd	$E_g + E_u$

Table 14: Irreps of the solvable octahedron wavefunctions. For brevity, the indication “even” in the table is short for even and non-zero.

T_d	E	$8C_3$	$6C_2$	$6C_4$	$3(C_4)^2$	i	$6S_4$	$8S_6$	$3\sigma_h$	$6\sigma_d$
$A_{1g} + A_{2u}$	+2	+2	0	0	+2	0	+2	0	0	+2
$A_{1g} + A_{2g}$	+2	+2	+2	+2	+2	0	0	0	0	0
$A_{1g} + A_{2g} + A_{1u} + A_{2u}$	+4	+4	0	0	+4	0	0	0	0	0
$E_{2g} + E_{2u}$	+4	-2	0	0	+4	0	0	0	0	0

Table 15: Character table for accidental degeneracies of the octahedron

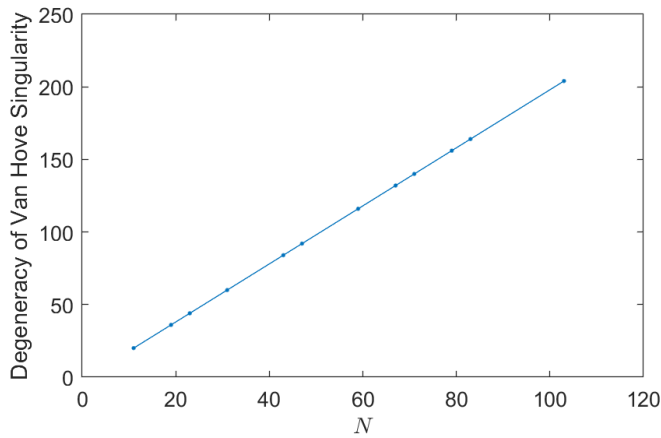


Figure 84: Degeneracy of the Van Hove singularity for the octahedron wavefunctions as a function of N

6.2.2 Van Hove singularity

The octahedron contained energy levels in the Van Hove singularity for some values of N at energies located at approximately $\frac{1}{3}$ and $\frac{2}{3}$ of the maximum possible energy. Interestingly, at values of N when the

Van Hove singularity did occur, the degeneracies of the both Van Hove singularities were identical and varied strictly linearly with N via the relation $D_{VH}(N) = 2N - 2$, as illustrated in Fig. (84). In further contrast with the tetrahedron case, the Van Hove singularity did not occur for every prime number N but did occur at exactly the Gaussian prime numbers, that is prime numbers of the form $N = 4n + 3$ for some $n \in \mathbb{Z}$.

6.3 Energy level statistics

The energy level spacing histograms within each irrep for the octahedron are shown in Figs. (86) and (87) while the LSR values for each irrep are shown in Figs. (88) and (89). We note that the one- and two-dimensional irreps have Poisson-like energy spacing distributions while the three-dimensional irreps have a Wigner-Dyson-like distribution. Correspondingly, the r values for the one- and two-dimensional irreps approach 0.39 as $N \rightarrow \infty$ while the r values for the three-dimensional irreps approach 0.53 as $N \rightarrow \infty$. Furthermore, as shown in Fig. (90), the proportion of states occupying the one-dimensional and two-dimensional irreps approaches $\frac{1}{12}$ and $\frac{1}{6}$ as predicted for the solvable states. Thus, there is no mixing of solvable and unsolvable wavefunctions within the same irreps.

6.4 Quantum scarring

As in the square-faced prism cases, the unsolvable wavefunctions on the octahedron similarly demonstrated quantum scarring. An example is illustrated in Fig. (85).

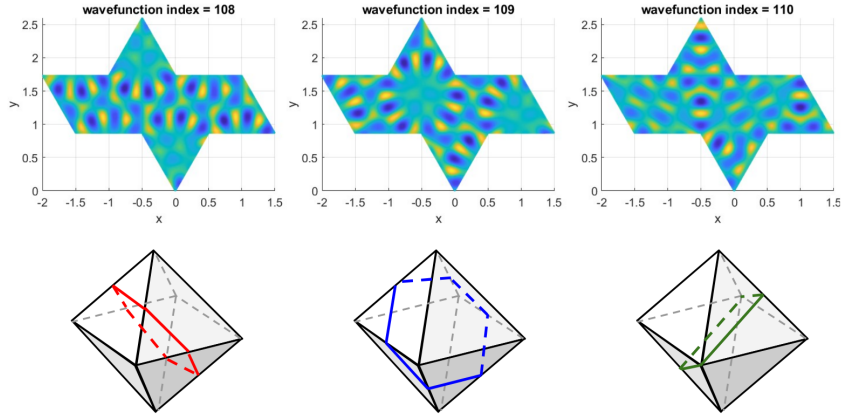


Figure 85: A three-fold degenerate energy level in the $N = 113$ octahedron case demonstrating enhanced probability density along classically unstable orbits

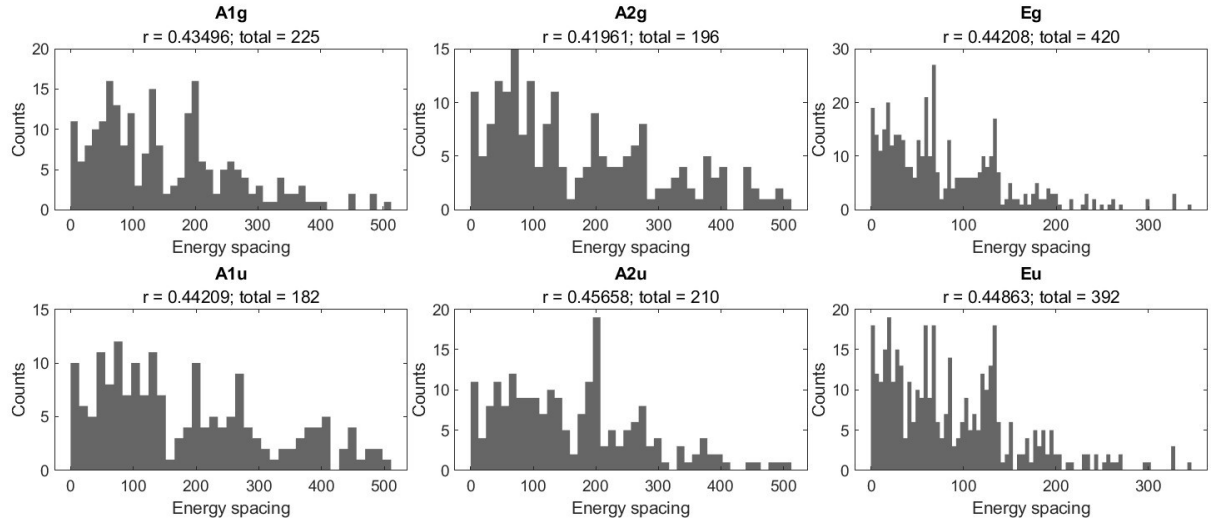


Figure 86: Energy-level spacing histograms for the one- and two-dimensional irreps. The total number of eigenfunctions in each irrep and the mean level spacing ratio r are indicated in the subtitle of each plot.

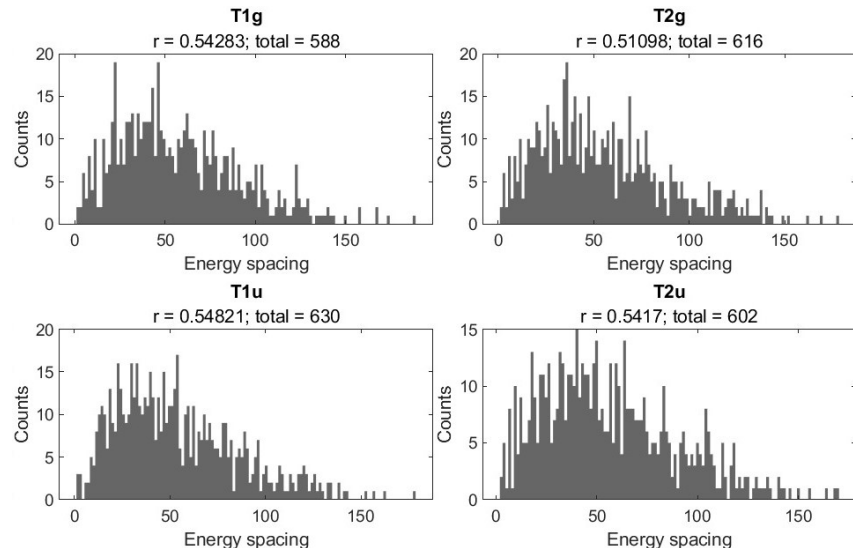


Figure 87: Energy-level spacing histogram for the three-dimensional irreps. The total number of eigenfunctions in each irrep and the mean level spacing ratio r are indicated in the subtitle of each plot.

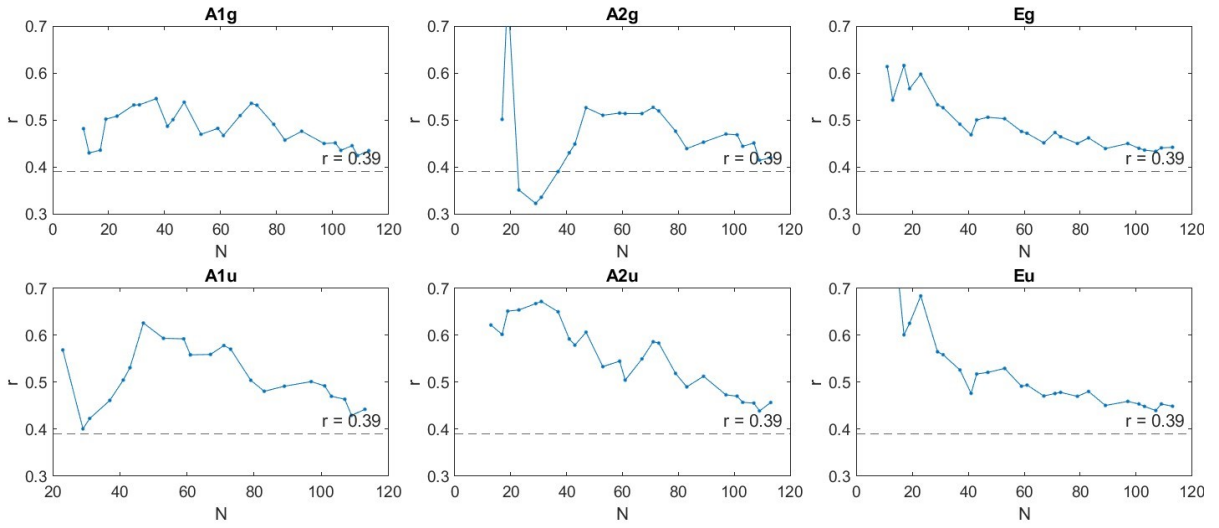


Figure 88: Plot of r values for each irrep as a function of N for the one- and two-dimensional irreps.

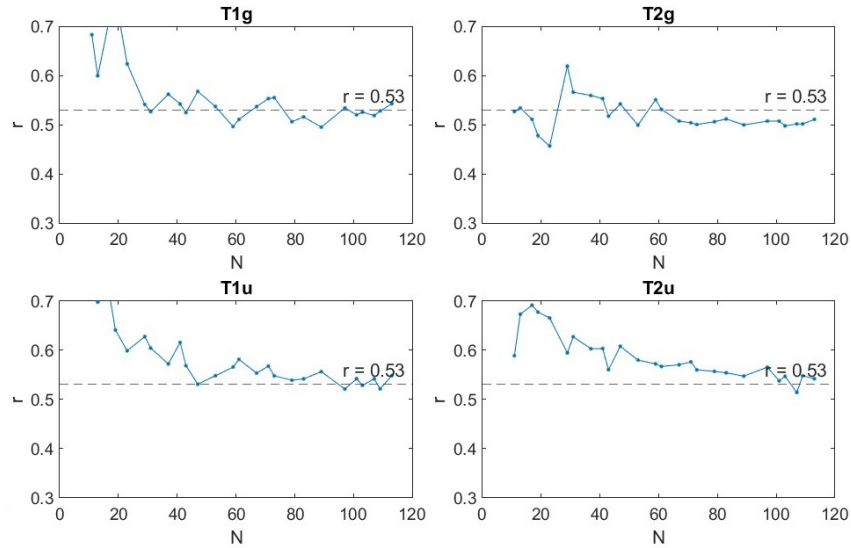


Figure 89: Plot of r values for each irrep as a function of N for the three-dimensional irreps.

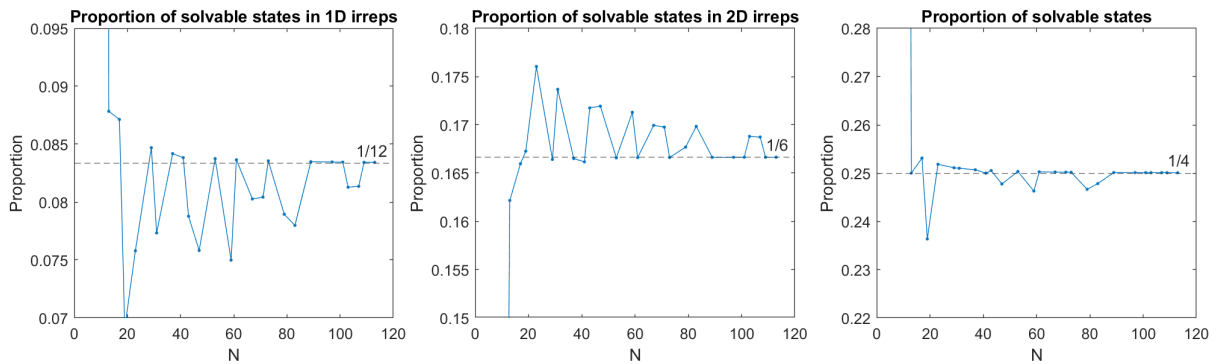


Figure 90: Plot of the proportion of eigenfunctions of \tilde{H} in the one- and two-dimensional irreps.

7 Unsolvable wavefunctions on the icosahedron

7.1 Incompleteness of the solvable wavefunctions

7.1.1 Proof via thermodynamics

The expected number of states with energy below E_0 for a particle confined to an area composed of 20 triangular faces spanned by the lattice vectors $\vec{a}_1 = (L, 0)$ and $\vec{a}_2 = (\frac{L}{2}, \frac{\sqrt{3}L}{2})$ is

$$N(E) = \frac{\pi E}{(2\pi)^2} \cdot 20 \cdot \frac{|\vec{a}_1 \times \vec{a}_2|}{2} = \frac{5E|\vec{a}_1 \times \vec{a}_2|}{2\pi}.$$

Next, recall the quantization condition of the wave vector for the icosahedron wavefunctions

$$\vec{k} = m\vec{b}_1 + n\vec{b}_2$$

where \vec{b}_i are the reciprocal vectors of the lattice vectors, and m and n can be any integers. Thus the area occupied by each wave vector \vec{k} in momentum space occupies an area

$$A_k = |\vec{b}_1 \times \vec{b}_2| = \frac{(2\pi)^2}{|\vec{a}_1 \times \vec{a}_2|} = \frac{4\pi^2}{|\vec{a}_1 \times \vec{a}_2|}.$$

Then since the wave functions are invariant under rotations of the wave vector by $\frac{\pi}{3}$ then the expected number of solvable wavefunctions is

$$N_s(E) = \frac{\pi E}{6A_k} = \frac{E|\vec{a}_1 \times \vec{a}_2|}{24\pi}.$$

Thus, it is clear that

$$\frac{N_s(E)}{N(E)} = \frac{1}{60},$$

so the solvable wavefunctions are incomplete and comprise only $\frac{1}{60}$ the complete set of solvable wavefunctions.

7.1.2 Proof of incompleteness via symmetry

The icosahedron has a C_5 rotation symmetry (see Fig. (91)), one of which corresponds to a $(x_1, x_2) \mapsto (x_1 + L, x_2)$ translation of the solvable wavefunctions. Since all the solvable wavefunctions are invariant under such translations then the solvable wavefunctions are all eigenfunctions of C_5 with eigenvalue +1. Thus, it is impossible to eigenfunctions of C_5 with eigenvalues at the complex fifth roots of unity using only solvable wavefunctions, indicating that they are incomplete.

7.2 Symmetries of the icosahedron

The symmetry group of the icosahedron is I_h which is isomorphic to $A_5 \times \mathbb{Z}/2\mathbb{Z}$ where A_5 indicates the alternating group on five indices. The A_5 subgroup corresponds to rotational symmetries while the generator of the $\mathbb{Z}/2\mathbb{Z}$ subgroup corresponds to the inversion symmetry.

An intuitive way to understand this symmetry group is to note that the icosahedron is the dual polyhedron of the dodecahedron which can be viewed as the convex hull of five distinct but overlapping tetrahedra whose vertices are coincident with the vertices of the dodecahedron. Labeling the five tetrahedra with numbers then allows us to identify each face of the dodecahedron by listing the clockwise

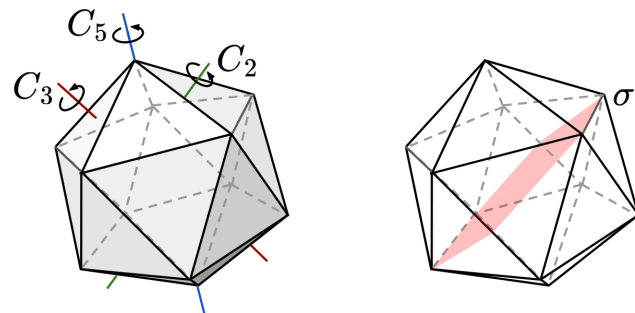


Figure 91: Representative example of each type of rotational symmetry of the icosahedron (left) as well as the σ symmetry (right)

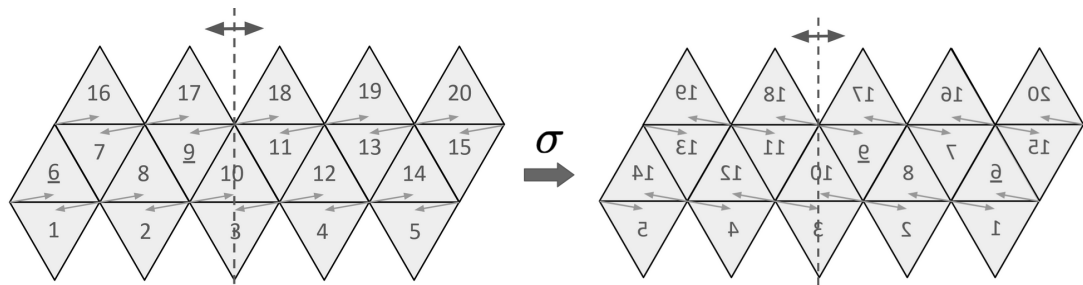


Figure 92: Implementation of the σ symmetry on the icosahedron net.

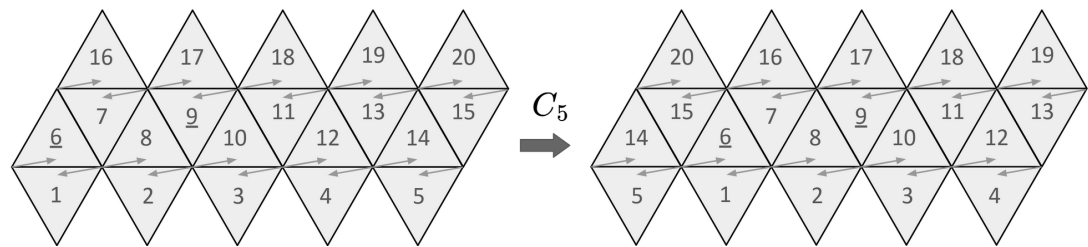


Figure 93: Implementation of the C_5 symmetry on the icosahedron net.

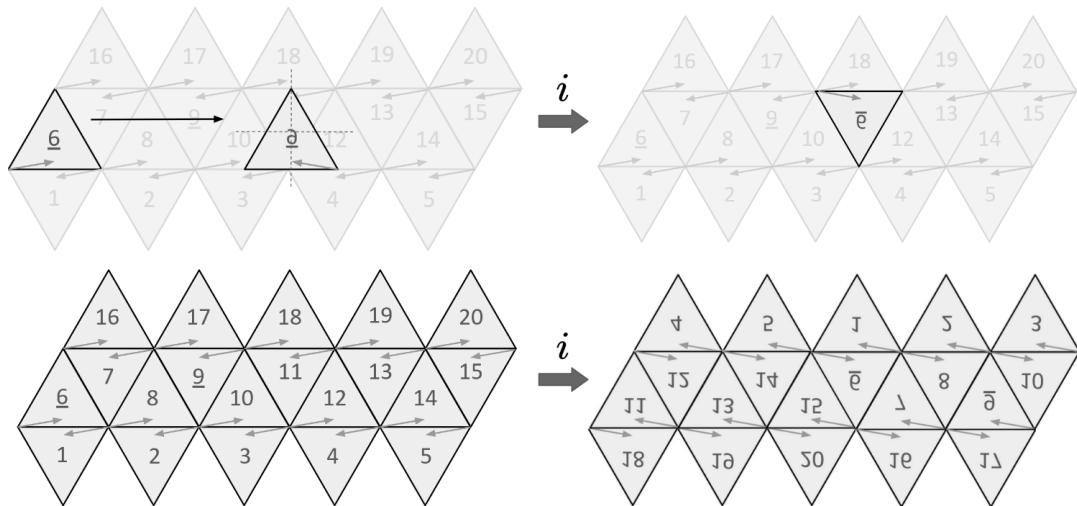


Figure 94: Implementation of the i symmetry on the icosahedron net.

vertex numbers. As the dodecahedron only has 12 faces but there are 24 possible orderings of five indices (up to five cycle permutations), only half of the possible orderings can be present. It can be checked that the possible face labels all correspond to the even permutations of five indices. Thus rotational symmetries will send an even permutation of the indices to another even permutation [25].

The character table for I_h is given in Tab. (16). A representative example of each of the rotation symmetries as well as the σ symmetry is illustrated in Fig. (91).

I_h	E	$12C_5$	$12(C_5)^2$	$20C_3$	$15C_2$	i	$12S_{10}$	$12(S_{10})^3$	$20S_6$	15σ
A_g	+1	+1	+1	+1	+1	+1	+1	+1	+1	+1
T_{1g}	+3	$-2 \cos(\frac{4\pi}{5})$	$-2 \cos(\frac{2\pi}{5})$	0	-1	+3	$-2 \cos(\frac{2\pi}{5})$	$-2 \cos(\frac{4\pi}{5})$	0	-1
T_{2g}	+3	$-2 \cos(\frac{2\pi}{5})$	$-2 \cos(\frac{4\pi}{5})$	0	-1	+3	$-2 \cos(\frac{4\pi}{5})$	$-2 \cos(\frac{2\pi}{5})$	0	-1
G_g	+4	-1	-1	+1	0	+4	-1	-1	+1	0
H_g	+5	0	0	-1	+1	+5	0	0	-1	+1
A_u	+1	+1	+1	+1	+1	-1	-1	-1	-1	-1
T_{1u}	+3	$-2 \cos(\frac{4\pi}{5})$	$-2 \cos(\frac{2\pi}{5})$	0	-1	-3	$+2 \cos(\frac{2\pi}{5})$	$+2 \cos(\frac{4\pi}{5})$	0	+1
T_{2u}	+3	$-2 \cos(\frac{2\pi}{5})$	$-2 \cos(\frac{4\pi}{5})$	0	-1	-3	$+2 \cos(\frac{4\pi}{5})$	$+2 \cos(\frac{2\pi}{5})$	0	+1
G_u	+4	-1	-1	+1	0	-4	+1	+1	-1	0
H_u	+5	0	0	-1	+1	-5	0	0	+1	-1

Table 16: Character table for I_h [11]

7.2.1 Irreps of the solvable wavefunctions

The classification of icosahedron solvable wavefunctions into irreps is relatively simple. Since the C_5 symmetry and σ symmetry can be implemented on the icosahedron net by a translation $(x_1, x_2) \mapsto (x_1 + L, x_2)$ and a reflection $(x_1, x_2) \mapsto (-x_1, x_2)$, respectively, it follows that

$$C_5 |\psi_{n_1, n_2}\rangle = |\psi_{n_1, n_2}\rangle$$

$$\sigma |\psi_{n_1, n_2}\rangle = |\psi_{-n_1, n_2}\rangle.$$

First, since all the solvable wavefunctions are eigenvectors of C_5 they must belong to the one-dimensional irreps. In the case where $n_2 = 0$ then $|\psi_{n_1, n_2}\rangle$ is an eigenfunction of σ as well with eigenvalue +1 and thus must belong in A_g . In the case where $n_2 \neq 0$ then the energy level is two-fold degenerate and spanned by $|\psi_{n_1, n_2}\rangle$ and $|\psi_{-n_1, n_2}\rangle$. It follows that

$$\left(\frac{\langle \psi_{n_1, n_2} | \pm \langle \psi_{n_1, -n_2} |}{\sqrt{2}} \right) \sigma_d \left(\frac{|\psi_{n_1, n_2}\rangle \pm |\psi_{n_1, -n_2}\rangle}{\sqrt{2}} \right) = \pm 1,$$

so the symmetric superposition belongs in A_g while the anti-symmetric superposition belongs in A_u . Thus, we can expect exactly one accidental degeneracy between A_g and A_u which has the symmetry traces indicated in Tab. (17).

I_h	E	$12C_5$	$12(C_5)^2$	$20C_3$	$15C_2$	i	$12S_{10}$	$12(S_{10})^3$	$20S_6$	15σ
$A_g + A_u$	+2	+2	+2	+2	+2	0	0	0	0	0

Table 17: Character table for accidental degeneracy of the octahedron

From Tables (16) and (17) it is clear that it suffices to consider the C_5 , i , and σ symmetries to distinguish all of the irreps. The C_5 symmetry can be implemented on the icosahedron net by a translation $(x_1, x_2) \mapsto (x_1 + L, x_2)$, and the σ symmetry can be implemented by a reflection about the line $x_1 = 0$. The i symmetry can be visualized that the reflection through the plane of the paper sends

the triangle 6 to the position occupied by triangle 11 after a horizontal reflection. Subsequent reflections of the triangle 6 about the horizontal and vertical lines the page then align triangle 6 as shown in the upper right of Fig. (94). The positions and orientations of the remaining triangles can be found by continuously extending from triangle 6.

7.2.2 Van Hove singularity

Similarly to the octahedron, the icosahedron contained energy levels in the Van Hove singularity for some values of N at energies located at approximately $\frac{1}{3}$ and $\frac{2}{3}$ of the maximum possible energy. At values of N when the Van Hove singularity did occur, the degeneracies of the both Van Hove singularities were identical and varied strictly linearly with N via the relation $D_{VH}(N) = 3N - 3$, as illustrated in Fig. (95). Similarly to the octahedron, the Van Hove singularity occurred exactly at the Gaussian prime numbers.

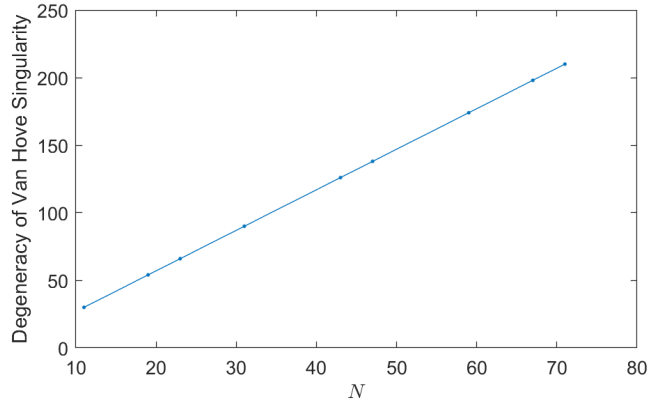


Figure 95: Degeneracy of the Van Hove singularity for the icosahedron wavefunctions as a function of N

7.3 Energy level statistics

The energy level spacing histograms within each irrep for the icosahedron are shown in Fig. (96) while the LSR values for each irrep are shown in Fig. (98). We expect that the one-dimensional irreps should have Poisson-like energy spacing distributions while the remaining irreps have a Wigner-Dyson-like distribution. We note that it is somewhat unclear whether or not the A_g and A_u irreps show a Poisson-like distribution but this could be due to the low number of states in these irreps. The low number of states in the one-dimensional irreps is entirely expected though since we predict that they comprise only $\frac{1}{60}$ of the total number of states, and due to the Van Hove singularity, we had to apply an energy cutoff. Correspondingly, the r values for the one-dimensional irreps do not clearly approach 0.39 as $N \rightarrow \infty$ as expected.

In the remaining irreps, the energy level spacing histograms do demonstrate a Wigner-Dyson-like peak but do not always clearly tend to zero as the energy spacing vanishing. Again this could be an issue of an insufficiently high number of states. Nonetheless, the r values for the remaining irreps roughly approach 0.53 as $N \rightarrow \infty$, as expected. Lastly, as shown in Fig. (97), the proportion of states occupying the one-dimensional irreps approaches $\frac{1}{60}$ as $N \rightarrow \infty$, as predicted for the solvable states. Thus, the one-dimensional irreps are comprised solely of solvable wavefunctions.

One method to verify that the solvable states follow a Poisson-like energy spacing distribution is

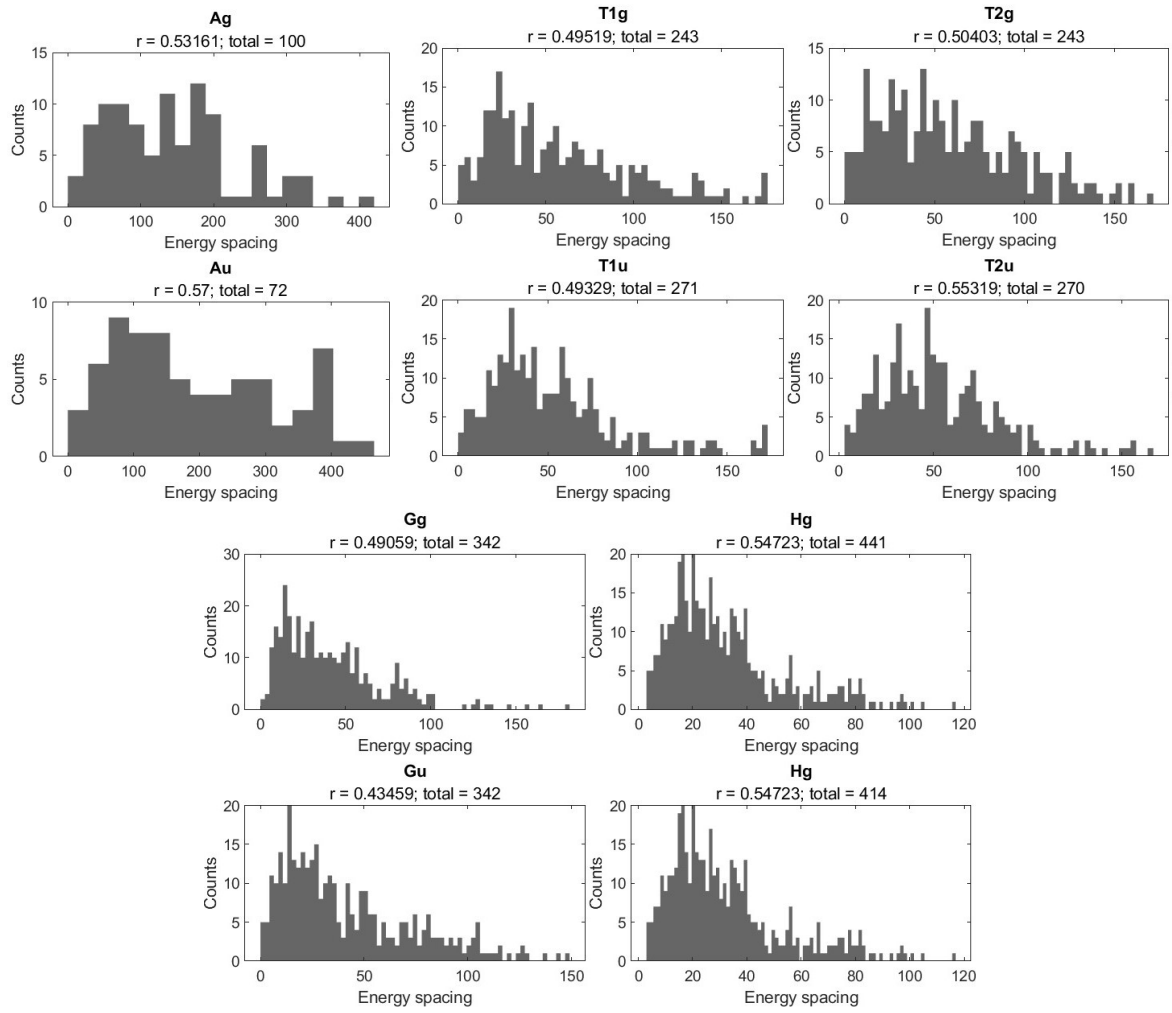


Figure 96: Energy level spacing histograms of the icosahedron wavefunctions

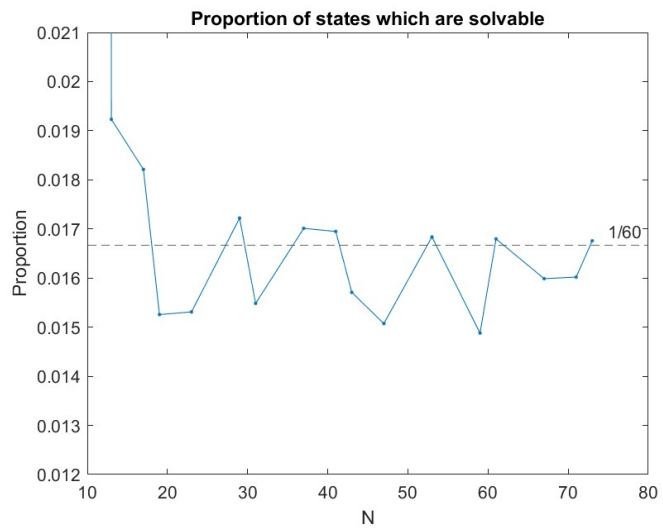


Figure 97: Proportion of icosahedron wavefunctions in the irreps predicted to contain solvable wavefunctions as a function of N .

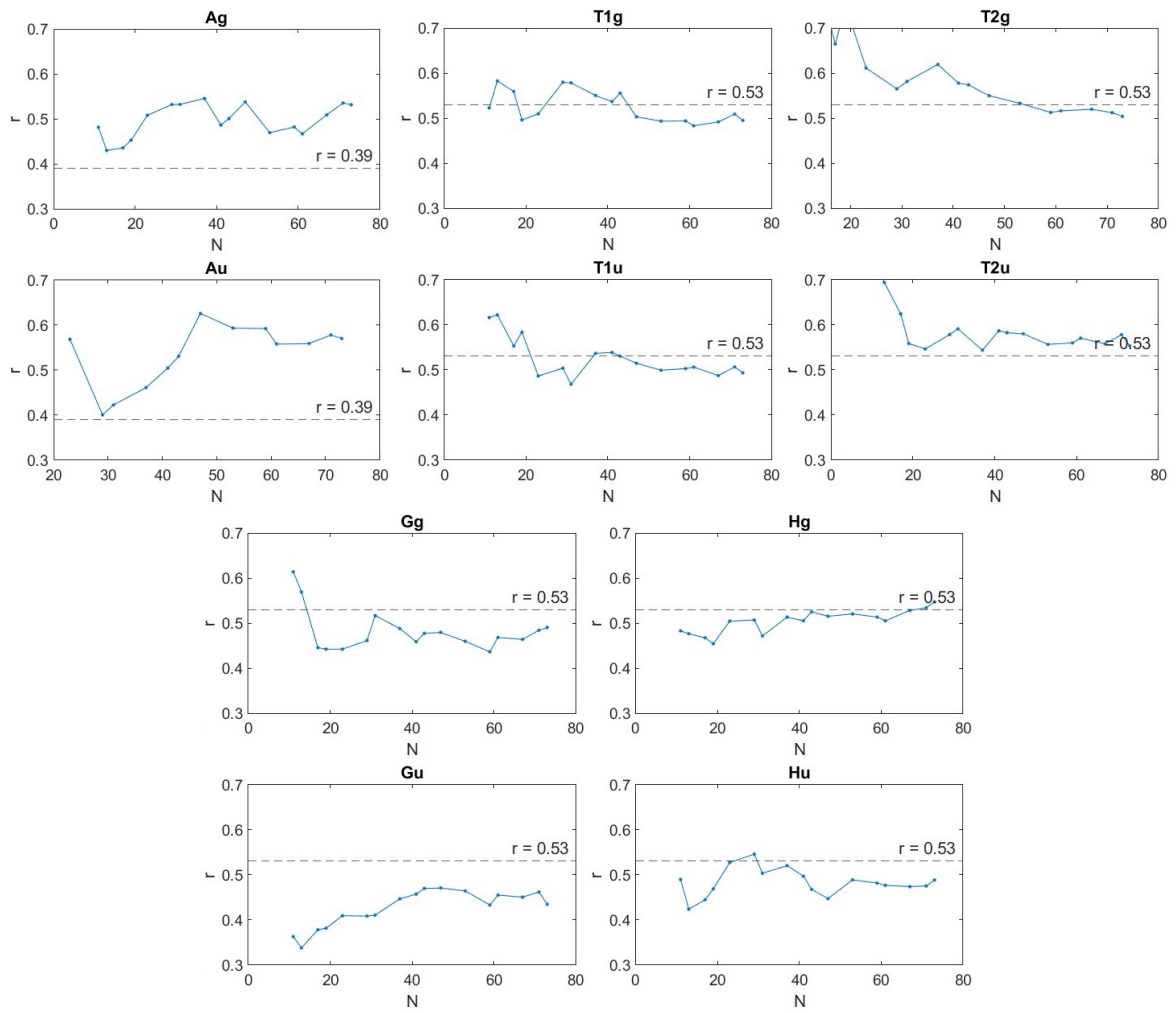


Figure 98: r values within each irrep of the icosahedron wavefunctions as a function of N .

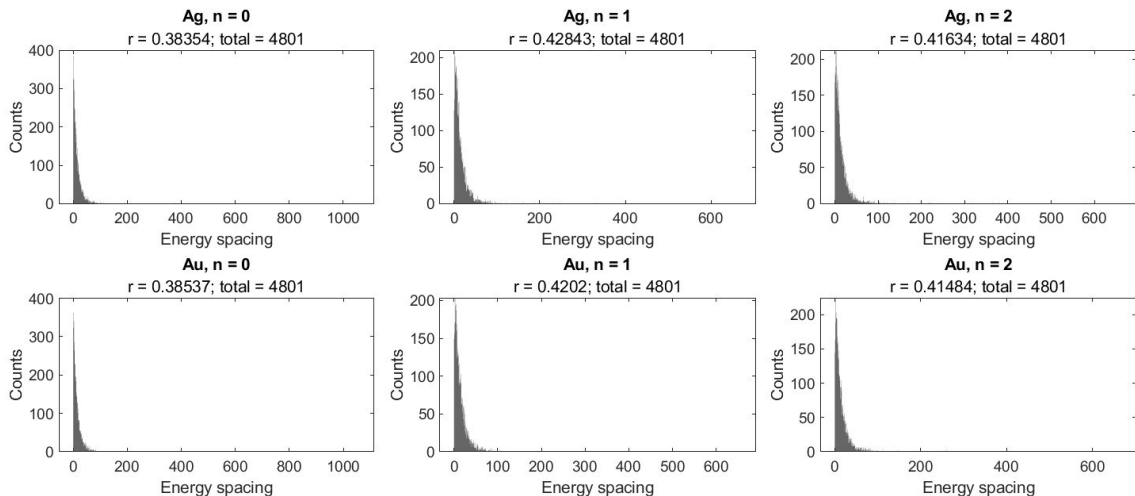


Figure 99: Energy spacing histograms when working in the $|w^n R_i\rangle$ basis for $n = 0, 1, 2$ for $N = 97$

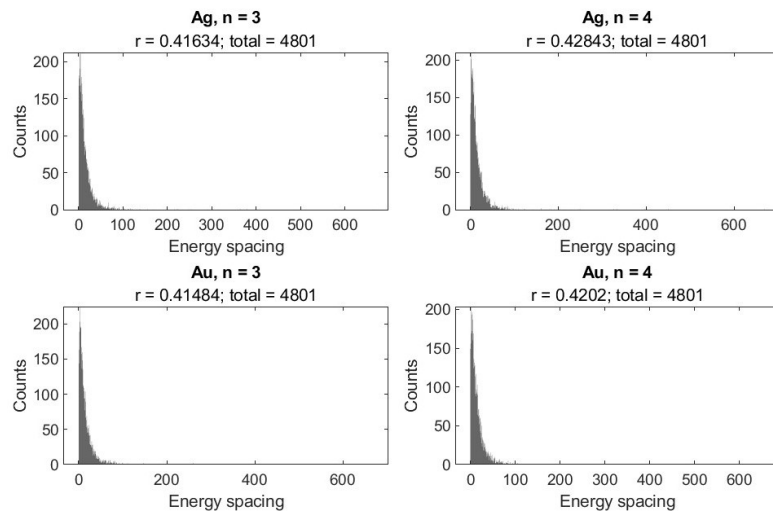


Figure 100: Energy spacing histograms when working in the $|w^n R_i\rangle$ basis for $n = 3, 4$ for $N = 97$

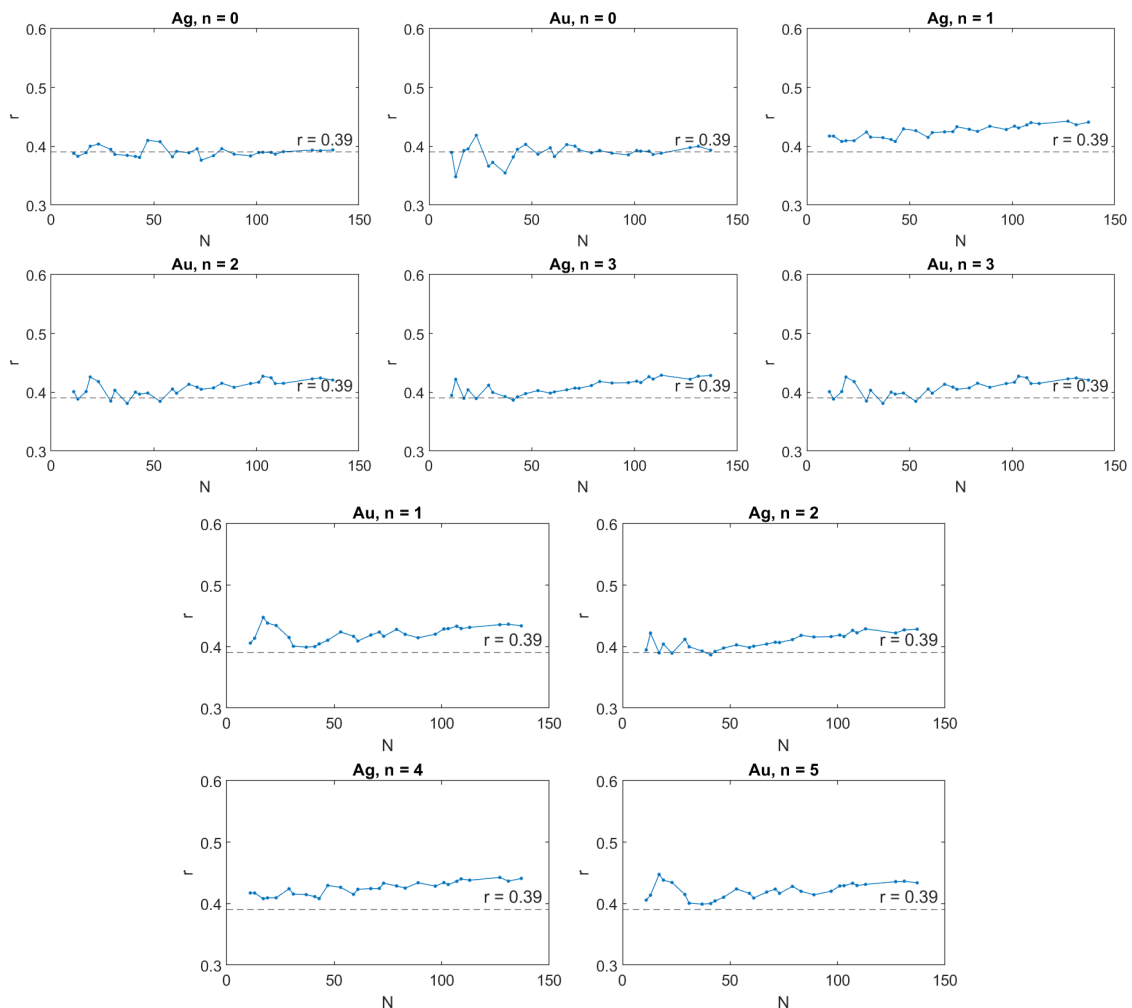


Figure 101: Plots of r as a function of N when working in the $|w^n R_i\rangle$ basis.

to instead work in the basis of states given by

$$|\omega^n R_i\rangle = \sum_{j=0}^4 \omega^{nj} |C_5^j R_i\rangle$$

where $\omega = e^{i\frac{2\pi}{5}}$, R_i is a lattice site on icosahedron net, and $n \in \{0, 1, 2, 3, 4\}$. We note that such wavefunctions are always eigenfunctions of C_5 with eigenvalue ω^n . Since $[H, C_5] = 0$ then we can block diagonalize H into five blocks corresponding to the five possible eigenvalues of C_5 . Moreover, we expect the wavefunctions to also be eigenfunctions of i , so we can classify all wavefunctions into either A_g or A_u simply from their i eigenvalue. Results for $N = 137$ are shown in Fig. (99). Note that as expected, for all n the energy spacing distribution is Poisson-like. Moreover, as shown in Fig. (101), the r values approach 0.39 as $N \rightarrow \infty$.

7.3.1 Quantum scarring

We conclude the analysis of the icosahedron wavefunctions by noting the presence of quantum scarring in some of the non-solvable wavefunctions. An example is illustrated in Fig. (102).

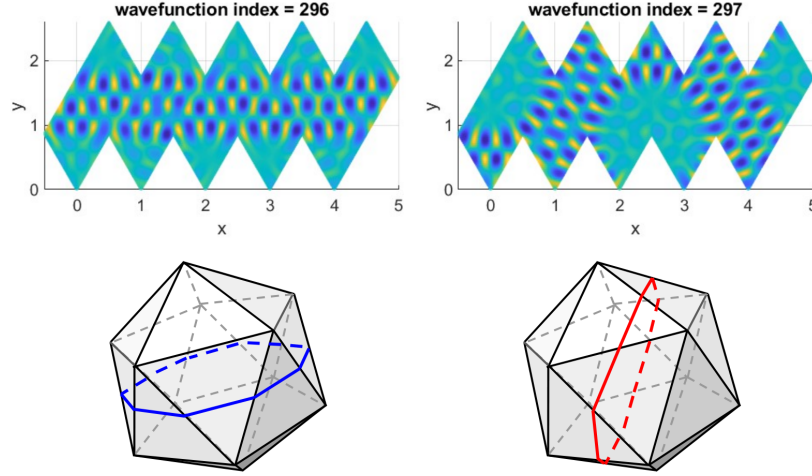


Figure 102: Two wavefunctions within a five-fold degenerate energy level belonging to the H_u irrep which demonstrate quantum scarring.

8 Billiards: an analogous classical problem

In classical mechanics, we are no longer constrained by the Heisenberg uncertainty principle and can specify a particle's position and momentum with arbitrary precision. Thus, the analogous classical problem of computing quantum wavefunctions is computing particle trajectories. There are previous studies on such trajectories in two-dimensional polygonal enclosures, referred to as billiards [26–29]. We first review some results from billiards in polygonal enclosures and then extend the results to billiards on polyhedral surfaces to study the classical counterpart of our polyhedral wavefunctions.

8.1 Billiards on 2D polygons

A theorem by Arnold states that an integrable Hamiltonian system explores a phase space with the topology of a torus while non-integrable Hamiltonian systems explore phase spaces with non-toroidal topologies [30]. Later, Berry and Richens introduced the concept of pseudo-integrable systems in their study of billiards in polygonal enclosures [12]. A pseudo-integrable system is a Hamiltonian system with an equal number of degrees of freedom and constants of motion but whose phase space is not topologically equivalent to a torus, suggesting non-integrability [12, 31]. Berry and Richens conjecture that these systems are chaotic with chaos emerging from splitting of trajectories near vertices of the polygonal enclosure.

8.1.1 Topology of phase space

Since the particle trajectories are independent of speed, the relevant phase space to consider is (\vec{q}, θ) where $\vec{q} = (x, y)$ is the position of the particle in the polygonal enclosure and θ is the angle of the trajectory. Berry and Richens examine polygonal enclosures with rational angles of π so that θ can only take on a finite number of values. Thus, the phase space can be visualized as a finite number of sheets in (\vec{q}, θ) space, each containing a replica of the polygonal enclosure such that the particle can jump between sheets after reflection about an edge. Then, identifying the edges of the sheets between which reflection occurs gives the surface in phase space in which the particle moves.

For example, consider the equilateral triangle. Then θ has six possible values. We can identify all edges by gluing the six sheets into a hexagon and identifying the boundary edges as shown in Fig. (103). A trajectory then can be represented by a straight line on the hexagon. Berry and Richens show that after identifying the boundary edges, the surface becomes a torus, indicating that the system is integrable. More generally, it will be shown later that polygons that tessellate the plane under reflections are integrable.

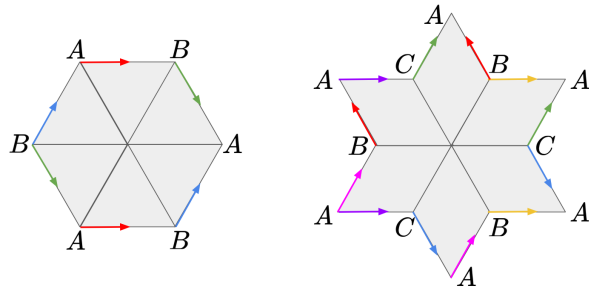


Figure 103: Illustration of the phase spaces for trajectories in the equilateral triangle (left) and a rhombus with angles $\frac{2\pi}{3}$ and $\frac{\pi}{3}$ (right). Edges on the boundary are identified by the colored arrows with same-color arrows glued together in the direction of the arrow.

In contrast, consider the rhombus with angles $\frac{2\pi}{3}$ and $\frac{\pi}{3}$ which does not tessellate the plane under

reflections. Again θ takes six possible values and the phase space can be illustrated by gluing together six copies of the rhombus under reflections about each boundary edge and then identifying the boundary edges as shown in Fig. (103). Berry and Richens demonstrate that this surface is topologically equivalent to the 5-fold torus, so the rhombus with interior angles $\frac{\pi}{3}$ and $\frac{2\pi}{3}$ is pseudo-integrable. More generally, they conjecture that any polygons with angles that are rational multiples of π and do not tessellate the plane under reflection are pseudo-integrable.

8.1.2 General method to calculate genus

Berry and Richens introduced a general method for calculating the genus of any rational polygonal enclosure. Using the identity

$$g = 1 - \frac{1}{2}\mathcal{I}$$

where \mathcal{I} is the index of a vector field \vec{V} on the surface. Only circuits about singularities in the vector field at vertices contribute to the index. For simplicity the constant vector field $\vec{V}(\vec{r}) = \hat{x}$ can be used. Then, the angle enclosed at each vertex of the polygonal region can be written in the form $\frac{2\pi p}{q}$ where q is even and p and q are positive integers which are otherwise co-prime. Then q copies of the sector around the vertex joined via reflections about the sector edges are required to complete a helicoid as illustrated, and the helicoid consists of p turns. The helicoid can then be compressed into a disc and the vector field becomes singular at the vertex.

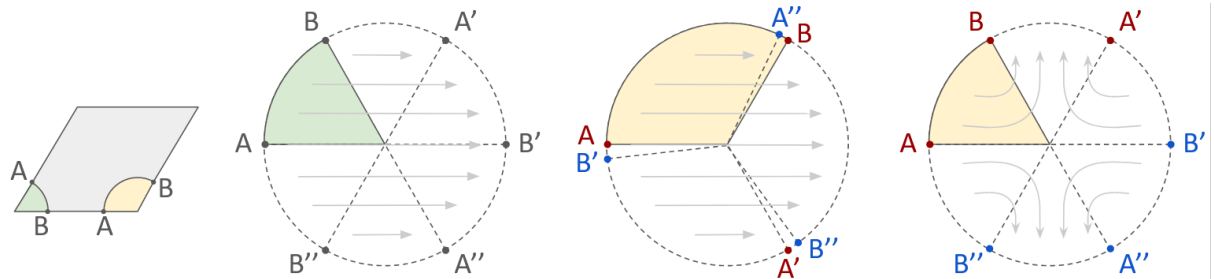


Figure 104: Construction of the phase space of the rhombus enclosure with angles $\frac{\pi}{3}$ (green sector) and $\frac{2\pi}{3}$ (yellow sector). The $\frac{\pi}{3}$ sector forms a helicoid with one turn under the reflection rule. The $\frac{2\pi}{3}$ sector forms a helicoid with two turns under the reflection rule. After continuously compressing the $\frac{2\pi}{3}$ sectors into $\frac{\pi}{3}$ sectors, the vector field becomes singular at the vertex.

To determine the index of the singularity, notice that a vector travelling around the outer edge of sector rotates relative to the vector field by $p - 1$ times. To see this, note that the helicoid contains p complete 2π rotations which are counteracted by one rotation of the vector in the opposite direction as it traverses the outer edge of the helicoid. As a result, the vertex has index $1 - p$.

Next, since q sectors of each vertex are required to assemble a complete helicoid while \mathcal{N} sheets are available in phase space to contribute sectors, then each vertex of the polygon can be treated as $\frac{\mathcal{N}}{q}$ independent vertices in phase space. Thus the genus of the phase space for a polygonal closure is

$$g = 1 - \frac{\mathcal{N}}{2} \sum_{v \in V} \frac{1 - p_v}{q_v} \quad (20)$$

where the sum goes over all vertices of the polygonal enclosure. From Eqn. (20), it is apparent that only vertices for which $p_v > 1$ contribute the non-toroidal topology of the phase space and consequently, result in a pseudo-integrable billiard system. In particular, we note that the angle $\frac{2\pi}{3}$ in the rhombus has

$p = 2$. More generally, the only enclosure angles that don't result in chaotic motion can be determined by setting $p = 1$ and $q = 2q'$ to be any even number i.e. $\theta = \frac{\pi}{q'}$ for any positive integer q' .

8.1.3 Demonstration of chaos

The integrability of trajectories on the equilateral triangles in comparison to the pseudo-integrability of trajectories on the rhombus can be demonstrated by a MATLAB simulation. Compare Figs. (105) and (106). Polygonal enclosures of side length 1 were simulated with a particle traveling with initial conditions (x_0, y_0, θ_0) with unit velocity. Within the interior of the polygonal enclosures, the particles follow constant velocity while at the boundaries they undergo specular reflection.

The MATLAB simulation is also useful for illustrating the behavior of closed periodic orbits (see Fig. (107) in comparison with ergodic orbits which explore all or almost all of the available phase space is explored (see Fig. (108)) [32]. The study of geodesics on polygonal enclosures remain an active area of research in mathematics [4].

8.2 Billiards on 3D polyhedra

When generalizing Berry and Richens's method to polyhedra phase spaces it is more natural to work with the conical singularity θ of each vertex instead of the enclosure angle since the conical singularity is independent of the particular unfolding used for the polyhedron.

We first write $\theta = \frac{2\pi\tilde{p}}{\tilde{q}}$ where \tilde{q} is even and \tilde{p} and \tilde{q} are otherwise co-prime integers. Then, similarly to before, \tilde{q} is the number of sectors required to construct a complete helicoid. Moreover, the number of sheets in phase space is given by the smallest number of multiples of θ required to reach a multiple of 2π . Thus,

$$\mathcal{N} = \begin{cases} \tilde{q} & \tilde{p} \text{ is odd} \\ \frac{\tilde{q}}{2} & \tilde{p} \text{ is even} \end{cases}$$

For the regular polyhedra considered so far we have $\theta = \pi, \frac{\pi}{3}, \frac{\pi}{2}, \frac{2\pi}{3}$ and $\frac{\pi}{5}$ which translate to $(\tilde{p}, \tilde{q}) = (1, 2), (1, 6), (1, 4), (1, 3)$, and $(1, 10)$, respectively. We note that \tilde{p} is odd in all cases so $\mathcal{N} = \tilde{q}$. Moreover, the number of rotations in each helicoid is given by $\frac{\tilde{q}}{2\pi}(2\pi - \theta) = \tilde{q} - \tilde{p}$, giving an index of $1 + \tilde{p} - \tilde{q}$ to the vector field at each vertex. Thus, Eqn. (20) simplifies to

$$g = 1 - \frac{1}{2} \sum_{v \in V} (1 + \tilde{p}_v - \tilde{q}_v) \quad (21)$$

where V is set of vertices of the polyhedron. In the case of a regular polyhedron we further gave that $\tilde{p}_v = 1$ and constant \tilde{q}_v across all vertices since every vertex has the same conical singularity and Eqn. (21) further simplifies to

$$g = 1 + \frac{V}{2}(2 - \tilde{q}) \quad (22)$$

Note that non-toroidal geometries can only occur if $\tilde{q} > 2$. Indeed the tetrahedron satisfies $\tilde{q} = 2$ while the remaining polyhedra have $\tilde{q} > 2$.

8.2.1 Topology of the cube phase space

A straightforward application of Eqn. (22) gives the genus of the cube phase space: $g = 9$. For an entertaining sanity check, the phase space topology of the cube can also be determined using techniques

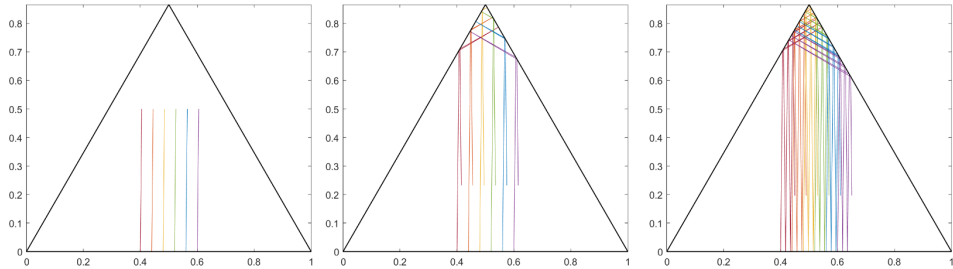


Figure 105: Classical billiards on an equilateral triangle. An ensemble of particles starting near $(\frac{1}{2}, 0)$ all with trajectory angle $\frac{2\pi}{3} - \varepsilon$ relative to the x axis remain close together even after arbitrarily long travel times: from left to right $t = 0.5, 1.5, 5$. A small perturbation $\varepsilon = 0.01$ was applied to the trajectory angle so that the trajectories would be non-closed.

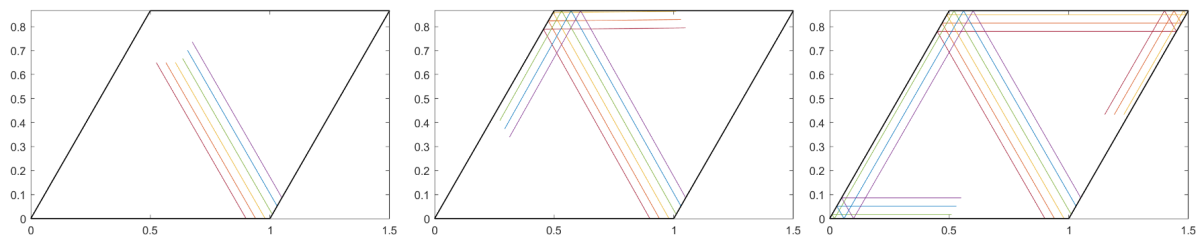


Figure 106: Classical billiards on a rhombus with angles $\frac{\pi}{3}$ and $\frac{2\pi}{3}$. An ensemble of particles starting near $(1, 0)$ all with trajectory angle $\frac{2\pi}{3}$ relative to the x axis demonstrate splitting after reflection off different sides of the $\frac{2\pi}{3}$ vertex. Plots are given after travel time $t = 0.5, 1, 5, 2.5$

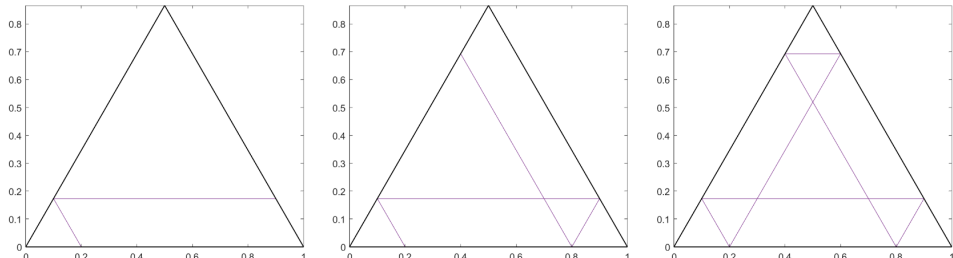


Figure 107: Example of a closed orbit in the triangle. Initial condition is $(0.2, 0, \frac{2\pi}{3})$ and the trajectories after travel times $t = 1, 2, 3$ are shown left to right.

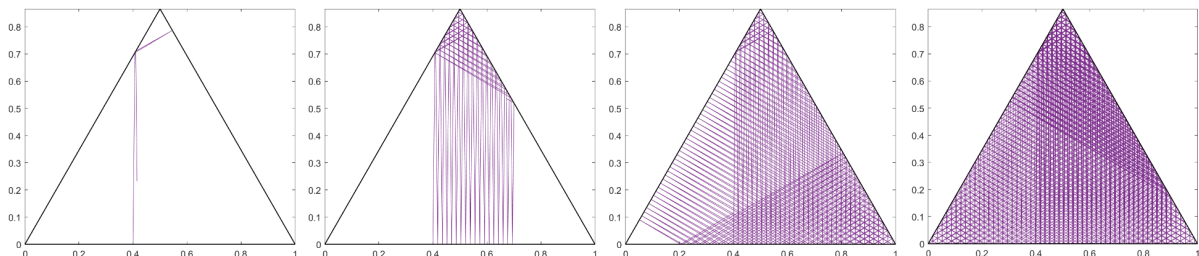


Figure 108: Example of an ergodic orbit in the triangle. Initial condition is $(0.4, 0, \frac{2\pi}{3} - 0.01)$ and the trajectories after travel times $t = 1.5, 50, 100, 250$ are shown left to right.

from algebraic topology. Since a trajectory on a cube can have four possible values of θ then the cube phase space can be represented by four copies of the cube net. The edges of the net are identified and correspond to changes in trajectory direction resulting from the conical singularities at the vertices as shown in Fig. (109). Denote this topological space X_{cube} .

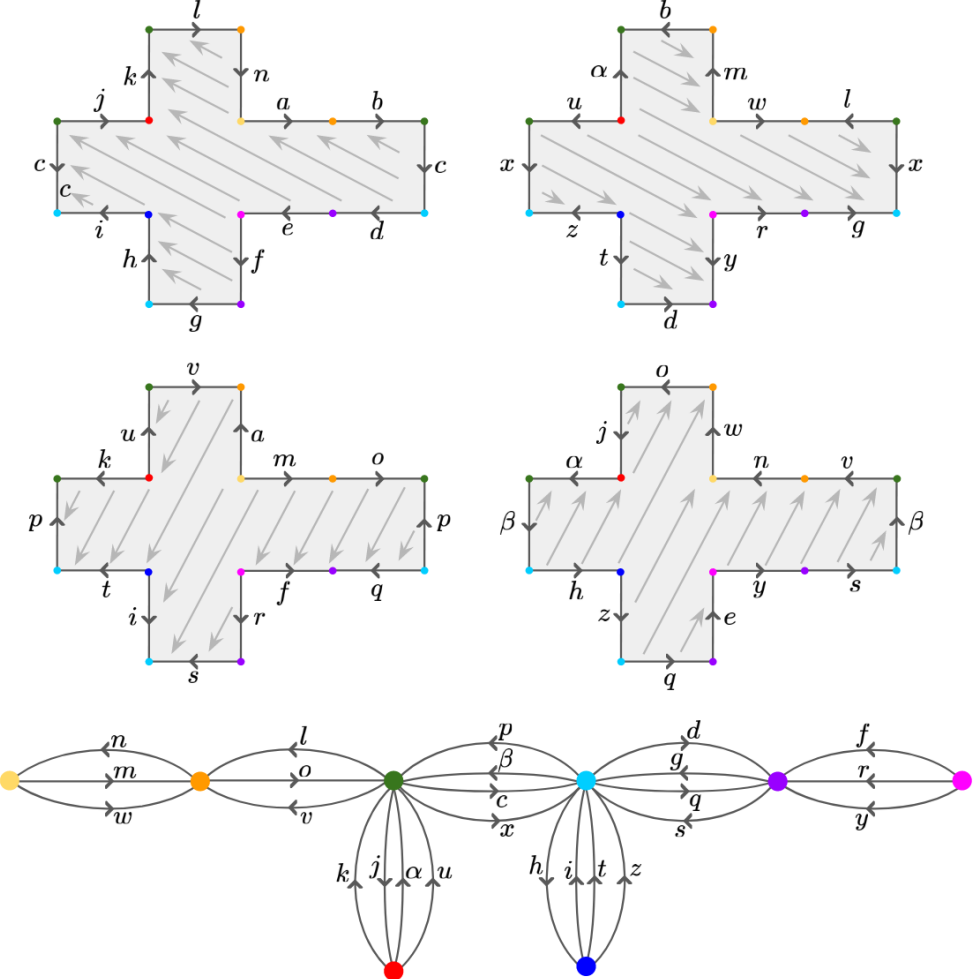


Figure 109: Illustration of the phase space of the cube X_{cube} (top, middle) and the graph obtained after joining the cube nets along edges a , b , and e and identifying all other boundary edges (bottom). The vertices in the cube nets correspond to the vertex in the graph with the same color.

The four copies of the cube net can be joined together to form a single edge-labeled polygon by identifying the three edges a , b , and e . Then, after identifying all edges on the boundary of the polygon we obtain the graph shown in Fig. (109). We can contract the graph along the minimum spanning tree consisting of edges n , l , k , p , h , d , and f to obtain a wedge of 18 circles indicating that the fundamental group of X_{cube} has 18 generators given by the letters

$$\pi_1(X_{cube}) = \langle m, w, o, v, j, \alpha, u, \beta, c, x, i, t, z, g, q, s, r, y | R \rangle. \quad (23)$$

Then an application of the Seifert van Kampen Theorem indicates that $\pi_1(X_{cube})$ is a free group on the 18 generators given in Eqn. (23) and satisfying the relation R determined by reading off the edges on the boundary of the polygon after contracting the edges contained in the minimum spanning tree:

$$moqrssi^{-1}tuvwm^{-1}wxg^{-1}r^{-1}yt^{-1}zx^{-1}u^{-1}\alpha cq^{-1}z^{-1}\beta^{-1}\alpha^{-1}j^{-1}o^{-1}w^{-1}v^{-1}\beta^{-1}s^{-1}y^{-1}gic^{-1}j = 1. \quad (24)$$

Next, we verify that X_{cube} is a compact 2D manifold. First, since each cube net is closed and bounded then X_{cube} is compact. Further, since the edge-labeled polygon can be embedded in \mathbb{R}^2 then X_{cube} is Hausdorff and has a countable basis. Lastly, one can check that a sufficiently small open disc about any point in X_{cube} is homeomorphic to an open subset of \mathbb{R}^2 . Thus, X_{cube} is a compact 2D manifold.

By the known classification of compact 2D manifolds, it suffices to consider the abelianization of $\pi_1(X_{cube})$ to classify the surface X_{cube} [33]. Since the relation R contains each generator of $\pi_1(X_{cube})$ and its inverse exactly once, then the relation R becomes trivial, so $\pi_1(X_{cube})/[\pi_1(X_{cube}), \pi_1(X_{cube})]$ is the free group on 18 letters. Therefore, X_{cube} must be a 9-fold torus, indicating that the system is pseudo-integrable.

Another more straightforward way to compute the genus of the surface is to use the algebraic relation for the Euler characteristic of a compact, oriented two-dimensional manifold

$$2 - 2g = F - E + V$$

where F , E and V are the number of faces, edges, and vertices, respectively, of any polygonalization of the surface [5, 34]. We can use the polygonalization given in Fig. (109). This polygonalization gives $F = 24$ since the four copies of the unfolded cube each contain six faces, $E = 28$ since each of the four copies contains 14 edges which are subsequently identified in pairs, and $V = 8$ which is apparent from the graph in Fig. (109), which gives $g = 9$, as desired.

8.2.2 Topology of other polyhedral phase spaces

A straightforward application of Eqn. (22) allows us to easily compute the genus of all the regular polyhedra as shown in Table (18). As expected, the tetrahedron phase space has toroidal geometry while the remaining polyhedra all have non-toroidal phase spaces.

Tetrahedron	Cube	Square & rectangular prisms	Octahedron	Dodecahedron	Icosahedron
1	9	9	4	25	61

Table 18: Genus of the phase spaces of the regular polyhedra.

References

- [1] A. Gonzalez, C. Noguez, G. Ortiz, and G. Rodriguez-Gattorno, *Optical absorbance of colloidal suspensions of silver polyhedral nanoparticles*, The Journal of Physical Chemistry B **109**, 17512 (2005).
- [2] X. Xu, Z. Saghi, R. Gay, and G. Möbus, *Reconstruction of 3D morphology of polyhedral nanoparticles*, Nanotechnology **18**, 225501 (2007).
- [3] Z. L. Wang and X. Feng, *Polyhedral shapes of CeO₂ nanoparticles*, The Journal of Physical Chemistry B **107**, 13563 (2003).
- [4] A. Zorich, *Flat surfaces*, arXiv preprint math/0609392 (2006).
- [5] M. P. Do Carmo, *Differential geometry of curves and surfaces: revised and updated second edition* (Courier Dover Publications, 2016).
- [6] J. Bělín, S. A. R. Horsley, and T. Tyc, *Quantum mechanics and Talbot revivals on a tetrahedron*, Phys. Rev. A **100**, 033806 (2019).
- [7] R. V. Jensen, *Quantum chaos*, Nature **355**, 311 (1992).
- [8] S. Wimberger, *Nonlinear dynamics and quantum chaos* Vol. 10 (Springer, 2014).
- [9] F. Haake, *Quantum signatures of chaos* (Springer, 1991).
- [10] D. V. Schroeder, *An introduction to thermal physics*, 1999.
- [11] M. S. Dresselhaus, G. Dresselhaus, and A. Jorio, *Group theory: application to the physics of condensed matter* (Springer Science & Business Media, 2007).
- [12] M. V. Berry and M. Tabor, *Level clustering in the regular spectrum*, Proceedings of the Royal Society of London. A. Mathematical and Physical Sciences **356**, 375 (1977).
- [13] O. Bohigas, M.-J. Giannoni, and C. Schmit, *Characterization of chaotic quantum spectra and universality of level fluctuation laws*, Physical review letters **52**, 1 (1984).
- [14] S. Müller, S. Heusler, P. Braun, F. Haake, and A. Altland, *Semiclassical foundation of universality in quantum chaos*, Physical review letters **93**, 014103 (2004).
- [15] Y. Atas, E. Bogomolny, O. Giraud, and G. Roux, *Distribution of the ratio of consecutive level spacings in random matrix ensembles*, Physical review letters **110**, 084101 (2013).
- [16] B. Lian, *Quantum breakdown model: From many-body localization to chaos with scars*, Physical Review B **107**, 115171 (2023).
- [17] V. Oganesyan and D. A. Huse, *Localization of interacting fermions at high temperature*, Physical review b **75**, 155111 (2007).
- [18] E. Brézin and S. Hikami, *Spectral form factor in a random matrix theory*, Physical Review E **55**, 4067 (1997).
- [19] S. Heusler, S. Müller, P. Braun, and F. Haake, *Universal spectral form factor for chaotic dynamics*, Journal of Physics A: Mathematical and General **37**, L31 (2004).
- [20] J. Liu, *Spectral form factors and late time quantum chaos*, Physical Review D **98**, 086026 (2018).
- [21] E. J. Heller, *Bound-state eigenfunctions of classically chaotic Hamiltonian systems: scars of periodic orbits*, Physical Review Letters **53**, 1515 (1984).

- [22] L. Kaplan, *Scars in quantum chaotic wavefunctions*, Nonlinearity **12**, R1 (1999).
- [23] S. W. McDonald and A. N. Kaufman, *Spectrum and eigenfunctions for a Hamiltonian with stochastic trajectories*, Physical Review Letters **42**, 1189 (1979).
- [24] B. Lian, Phy525: Introduction to condensed matter physics.
- [25] S. Kotak, Symmetry groups of platonic solids, 2009.
- [26] J. Cassaigne, P. Hubert, and S. Troubetzkoy, Complexity and growth for polygonal billiards, in *Annales de l'institut Fourier* Vol. 52, pp. 835–847, 2002.
- [27] G. Harris, *Polygonal Billiards*, Southern Illinois university Edwardsville **87**, 88 (2007).
- [28] M. D. Boshernitzan, *Billiards and rational periodic directions in polygons*, The American mathematical monthly **99**, 522 (1992).
- [29] C. Boldrighini, M. Keane, and F. Marchetti, *Billiards in polygons*, Publications des séminaires de mathématiques et informatique de Rennes , 1 (1976).
- [30] V. I. Arnol'd *Mathematical methods of classical mechanics* Vol. 60 (Springer Science & Business Media, 2013).
- [31] J. Hannay and R. McCraw, *Barrier billiards-a simple pseudo-integrable system*, Journal of Physics A: Mathematical and General **23**, 887 (1990).
- [32] S. Pilatowsky-Cameo *et al.*, *Ubiquitous quantum scarring does not prevent ergodicity*, Nature communications **12**, 852 (2021).
- [33] J. R. Munkres, *Elements of algebraic topology* (CRC press, 2018).
- [34] B. Pollard, *An Introduction to Algebraic Topology* (PRE-21503, 1977).